CRITICAL BEHAVIOR AND DYNAMICS OF THE SUPERFLUID-MOTT GLASS TRANSITION

by

JACK RUSSELL CREWSE III

A DISSERTATION

Presented to the Graduate Faculty of the

MISSOURI UNIVERSITY OF SCIENCE AND TECHNOLOGY

In Partial Fulfillment of the Requirements for the Degree

DOCTOR OF PHILOSOPHY

in

PHYSICS

2024

Approved by:

Dr. Thomas Vojta, Advisor
Dr. Ulrich Jentschura
Dr. Yew San Hor
Dr. Alexey Yamilov
Dr. Ferdinand Evers

PUBLICATION DISSERTATION OPTION

This dissertation consists of the following four articles, formatted in the style used by the Missouri University of Science and Technology.

Paper I: Pages 23-53 has been published as *Quantum critical behavior of the superfluid-Mott glass transition* in Physical Review B **94**, 134501 (2016) with Thomas Vojta, Martin Puschmann, Daniel Arovas and Yuri Kiselev.

Paper II: Pages 54-84 has been published as *Quantum critical behavior of a three-dimensional superfluid-Mott glass transition* in Physical Review B **98**, 054515 (2018) with Cameron Lerch and Thomas Vojta.

Paper III: Pages 85-117 has been published as *Collective modes at a disordered quantum phase transition* in Physical Review Letters **125**, 027002 (2020) with Martin Puschmann, José Hoyos, and Thomas Vojta.

Paper IV: Pages 118-147 has been published as *Localization of the Higgs mode at the superfluid-Mott glass transition* in Physical Review B **104**, 014511 (2021) with Thomas Vojta.

In addition to the papers presented in this dissertation, Jack has also contributed to two publications on material unrelated to the topic of this dissertation as part of his work as a visiting researcher in the group of Ferdinand Evers at the University of Regensburg.

Paper V: *Tunable non-integer high-harmonic generation in a topological insulator* in Nature **593**, 385-390 (2021) with C.P. Schmid, L. Weigl, P. Grössing, V. Junk, C. Gorini, S. Schlauderer, M. Meierhofer, N. Hofmann, D. Afanasiev, KA Kokh, OE Tereshchenko, J. Güdde, F. Evers, J. Wilhelm, K. Richter, U Höfer, and R. Huber.

Paper VI: *Semiconductor Bloch-equations formalism: Derivation and application to high-harmonic generation from Dirac fermions* Physical Review B **103**, 125419 (2021) with J. Wilhelm, P. Grössing, A. Seith, M. Nitsch, L. Weigl, C. Schmid, and F. Evers.

ABSTRACT

This work studies the effects of disorder on the thermodynamic critical behavior and dynamical properties of the superfluid-Mott glass quantum phase transition. After a brief introduction covering relevant fundamentals, we present the dissertation in the form of four separate but related publications.

In the first two publications, we calculate the thermodynamic critical exponents of the superfluid-Mott glass quantum phase transition in both two and three spatial dimensions. The undiluted transition exhibits critical exponents that violate the Harris criterion, and thus the critical behavior is expected to change upon introducing disorder. We confirm this behavior via Monte Carlo simulation of a diluted quantum rotor model of the transition, calculating new phase diagrams and critical behavior for the diluted systems.

In publications three and four, we investigate the dynamical properties of the collective modes near the transition boundary based on scaling arguments. These collective modes are expected to have energies that follow a power-law relationship governed by the critical exponents. In these publications, we find that in two spatial dimensions, the introduction of disorder localizes the Higgs mode, defying this expectation.

In conclusion, the introduction of disorder to the superfluid-Mott insulator system has a significant effect on the thermodynamic critical behavior. In our calculations, we see that the disordered case has a new set of critical exponents that govern the power-law critical behavior of the superfluid-Mott glass transition. Despite the critical behavior of the transition being of conventional power-law type, when we consider the dynamics of the collective excitation modes, we see localization behavior that is unaccounted for in current theoretical descriptions. This shows that in disordered systems one may observe unconventional dynamical behavior in a system whose underlying thermodynamics is that of conventional power-law type.

ACKNOWLEDGMENTS

Completing this dissertation was only possible thanks to the supportive network of educators, mentors, family and friends whose guidance and encouragement have been instrumental in my journey through graduate education.

First and foremost, I am profoundly grateful to my thesis adviser, Thomas Vojta, whose mentorship has been a cornerstone in my professional development. Working with him has been a terrific privilege in my career.

I would also like to acknowledge the influence and mentoring provided by many of the faculty in the Department of Physics: Dr. Greg Story for his passionate teaching, Dr. Ulrich Jentschura for his willingness to discuss the most abstract of topics, and Dr. Yew San Hor for providing my first look inside the world of research. A special thanks must also be extended to Dr. Ferdinand Evers from the University of Regensburg, for a memorable and enriching experience as a visiting researcher in Germany.

Beyond my professional colleagues and mentors, I must also acknowledge the many family and friends who provided support through my studies. My parents, Rusty and Stella Crewse, who have been unflinchingly supportive in every endeavor I have taken on in my life. My friends, especially the people of KMNR, who provided so many good times and good people to contrast the challenges of graduate studies. A special mention must go out to my friend Mat Pollard, with whom I've had some of the most valuable intellectual discussions of my life and without whom I may have never passed the qualifying exam.

Last but certainly not least, my wonderful wife Shay, who has put up with many long nights, frustrations and struggles throughout nearly every moment of both my undergraduate and graduate studies. She held me up during the worst times and made me stand taller during the best. I love you to no end.

TABLE OF CONTENTS

Page

LIST OF ILLUSTRATIONS

Figure Page

PAPER I

PAPER II

LIST OF TABLES

1. INTRODUCTION

1.1. CLASSICAL PHASE TRANSITIONS

1.1.1. Phase Transition Classification. Phase transitions are characterized by abrupt changes in the macroscopic thermodynamic properties (the 'phase') of a system in response to a smooth change in some parameter of the system such as temperature, pressure, magnetic field, or chemical composition. The solid-liquid-gas transitions of water are abrupt changes in density in response to changes in either temperature or pressure. The creation of a permanent iron magnet is an abrupt change of the ferromagnetic materials magnetism in response to an external magnetic field. Formally, phase transitions (or more precisely phase boundaries) can be defined as non-analyticities (discontinuities, singularities) in the thermodynamic free energy as a function of the parameters of the system (e.g. temperature, pressure, magnetic field) [1]. These non-analyticities of the free energy can come in two types which serve to classify phase transitions into two broad categories: first-order and continuous.

In *first-order* (or discontinuous) transitions, the free energy is continuous across the phase boundary, but features discontinuities in it's first derivatives. This implies a *latent heat* – a certain amount of heat that is required to be absorbed or emitted by the system to completely cross the phase boundary. Additionally, first-order phase transitions exhibit *phase coexistence*, where both phases exist in equilibrium with each other at the phase boundary. The solid-liquid-gas transitions of water used in everyday life are simple examples of first-order transitions.

In *continuous* transitions (or *critical points*), the free energy as well as it's first-derivatives are continuous across the phase boundary. This means no latent heat is required and the transition occurs continuously as the phase boundary is approached. However, the free energy exhibits discontinuities in it's higher-order derivatives, which leads to diverging

susceptibilities and correlation lengths of fluctuations. A prominent example of a continuous transition is the ferromagnetic transition of iron, wherein the magnetization continuously decreases to zero as the critical temperature is approached.

In addition to classification via the non-analyticities of the free energy of the system, we will see in the following Sections that continuous phase transitions may be further classified by their *critical exponents*. These exponents define the way in which the various observables of a system behave upon approaching a phase boundary and are powerful analytic tools in understanding phase transition behavior. Further, we will see that these critical exponents fall into so-called *universality classes*, within which the relevant systems all exhibit the same critical behavior and exponents, with the nature of their phase transitions being dependent only upon the dimensionality and symmetries of the degrees-of-freedom of the underlying Hamiltonian [2, 3].

1.1.2. Critical Exponents and Universality. Both first-order and continuous phase transitions are often best described in terms of an *order parameter* Ψ – a thermodynamic observable that is zero in the 'disordered' phase ($\Psi = 0$) and finite in the 'ordered' phase ($\Psi \neq 0$) [4, 5]. For example, the magnetization in ferromagnetic transitions, density-differences in solid-liquid-gas transitions, or the density of superconducting electrons in superconductor-insulator transitions. A key component to understanding the critical behavior of phase transitions is the role of fluctuations (in space and time) of this order parameter. While an order parameter may exhibit a zero *average* value in the disordered phase, the fluctuations of the order parameter about this mean value are non-zero. In fact, for continuous transitions it can be observed that the correlation length ξ of these order parameter fluctuations becomes long-ranged as the critical point is approached, diverging at the critical point according to a power-law relationship dependent on the external tuning parameter. This allows us to write an expression for the correlation length divergence in

Table 1.1. Definitions of commonly used critical exponents and the conditions under which they are valid. h represents a field conjugate to the order parameter.

Observable	Exponent	Definition	Conditions
Specific heat	α	$C \sim \lvert r\rvert^{-\alpha}$	$r \to 0$, $h = 0$
Order parameter	β	$\Psi \sim (-r)^{\beta}$	$r \to 0$, $h = 0$
Susceptibility	γ	$\chi \sim \lvert r\rvert^{\gamma}$	$r \to 0$, $h = 0$
Critical isotherm	δ	$\Psi \sim h^{1/\delta}$	$r = 0$, $h \to 0$
Correlation length	ν	$\xi \sim \lvert r\rvert^{-\nu}$	$r \to 0$, $h = 0$
Correlation function	η	$G(\mathbf{x}) \sim \lvert\mathbf{x}\rvert^{-d+2-\eta}$	$r = 0$, $h = 0$
Dynamic correlation	z	$\tau_c \sim \xi^z$	$r \to 0$, $h = 0$

terms of the dimensionless distance from criticality $r \equiv (T - T_c)/T_c$

$$\xi \sim |r|^{-\nu} \tag{1.1}$$

which serves to define the correlation length critical exponent ν that determines the nature of the divergence as the critical point $r = 0$ is approached. Not only are spatial correlations divergent near the critical point, but also the correlation times of these fluctuations. Another critical exponent may be defined, the dynamical exponent z, that describes this divergence of the correlation time τ_c as well,

$$\tau_c \sim \xi^z \sim |r|^{-z\nu}. \tag{1.2}$$

At the critical point, fluctuations exist on all length and time scales, thus rendering the system *scale-invariant*. This scale-invariance results in the observables of the system obeying power-law relationships dependent on the external parameters of the system. We may therefore define critical exponents for each relevant observable such as heat capacity, susceptibility, and order parameter as shown in Table 1.1. These critical exponents uniquely characterize the critical behavior near a continuous phase transition.

The scale-invariant nature of critical points leads to the concept of *universality* wherein the divergence of the correlation length-scales renders the microscopic details of the system irrelevant, with the nature of the phase transition depending only upon the dimensionality and the symmetries of the degrees-of-freedom of the underlying microscopic Hamiltonian. The symmetries and dimensionality of the system thus serve to classify continuous phase transitions even further, into so-called *universality classes*. Within a particular universality class, the critical behavior is universal among the relevant systems which share the same critical exponent values (e.g. easy-plane magnets and liquid Helium-4, two very different physical systems, exhibit the same critical exponents and therefore belong to the same universality class) [7]!

1.2. THEORETICAL DESCRIPTION OF PHASE TRANSITIONS

1.2.1. Mean-field and Landau Theories. The earliest successful theories describing phase transitions were *mean-field theories*, where the mathematical difficulties of interacting many-body systems are eliminated by approximating the many-body interactions as an external field consisting of the 'mean' interactions of the many-body system, reducing the issue to a much simpler, single-particle problem [5]. These theories have found success in describing ferromagnetic transitions and even in describing some metal-superconductor transitions. However, the predictions of mean-field theory are typically limited, providing only a single set of critical exponents and therefore, cannot account for a large number of universality classes that are observed in nature.

Perhaps the greatest paradigm shift in the understanding of phase transitions came from the mind of Landau in the late 1930's [4]. Landau set out to generalize mean-field like approaches and his proposal was two-fold. First, was the concept of the order parameter Ψ – an observable of the system whose value is zero $\Psi = 0$ on one side of a phase boundary (in the 'disordered' phase) and takes on a finite value $\Psi \neq 0$ on the other side (in the 'ordered' phase). Some examples include: magnetization in magnetic transitions, density

difference in solid-liquid-gas transitions of water, density of superconducting electrons for superconductor-insulator transitions. Second, Landau proposed that the Helmholtz free energy F of the system is an analytic function of the order parameter. Accordingly, near the critical point (where the order parameter is finite, but small) the free energy can be expanded in powers of the order parameter

$$F_L = F_L(0) - h\Psi + r\Psi^2 + v\Psi^3 + u\Psi^4 + \ldots \tag{1.3}$$

where $F_L(0)$ is the free energy in the disordered phase ($\Psi = 0$), h represents an external field conjugate to the order parameter, and r, v, and u are system-dependent constants that are independent of the order parameter.

To see that this form of the free-energy captures the expected behavior of a phase transition, let us consider a system with no external field ($h = 0$), close to the phase boundary ($|\Psi| \ll 1$). In this case, the higher order terms of F_L may be safely ignored. Additionally, if the free energy is invariant under a sign change of Ψ, then only *even* powers should contribute to the free-energy ($v = 0$) since it should not depend on the sign of the order parameter (e.g. the free-energy of a magnet does not depend on the orientation of the north and south poles without some external field). In this case, the Landau free energy takes the form

$$F_L = F_L(0) + r\Psi^2 + u\Psi^4. \tag{1.4}$$

The equilibrium value of the order parameter is then determined by minimizing F_L with respect to Ψ. Setting the first derivative to zero leads to the equation

$$r\Psi + 2u\Psi^3 = 0 \tag{1.5}$$

for which we can see has two solutions $\Psi = 0$ (for $r > 0$) and $\Psi = \pm\sqrt{-r/2u}$ (for $r < 0$). The first solution represents the system in the disordered phase $\Psi = 0$ and the second represents the system in the ordered phase $\Psi \neq 0$. This allows us to attribute some physical meaning to the parameter r as the distance from criticality $r = (T - T_c)/T_c$, where T is some system parameter that is used to tune through the phase transition (i.e. temperature, pressure, coupling constant). This result also allows us to determine the critical exponents of the system. We now have the order parameter in a form dependent on the distance from criticality r

$$\Psi \sim (-r)^{\beta} \tag{1.6}$$

which allows us to conclude $\beta = 1/2$. We may also find the critical exponents of the specific heat (via the second derivative of F_L), susceptibility and external field (by considering $h \neq 0$) through more involved calculations that provide $\alpha = 0$, $\gamma = 1$, and $\delta = 3$.

Interestingly, these are the exact critical exponents that one would find via mean-field theory techniques. This is striking, as the system-dependent parameters in the theory capture the unique structure of each system we may consider, but yet the critical exponents remain the same. One may think this is a sign of the universality phenomenon we have already briefly discussed. However, Landau's theory would suggest that *every* phase transition should belong to the same universality class!

1.2.2. Ginzburg-Landau-Wilson Theory. The key component missing from Landau's original theory is the role of *fluctuations* and *long-range correlations*. The inclusion of these features in the free energy is relatively straight forward. We must now consider a spatially dependent order parameter $\Psi(\mathbf{x})$, to capture spatial fluctuations, as well as it's gradient $\nabla\Psi(\mathbf{x})$, to capture long-range correlations. Calculation of the free energy now takes the form of an integration across the volume V of the system in question

$$F_L\big[\Psi(\mathbf{x})\big] = \int_V d^d x \Big[- h\Psi(\mathbf{x}) + r\Psi^2(\mathbf{x}) + u\Psi^4(\mathbf{x}) + [\nabla\Psi(\mathbf{x})]^2 \Big]. \tag{1.7}$$

where d is the spatial dimensionality of the system being considered. This theory, often called the Landau-Ginzburg-Wilson theory of phase transitions, is quite useful in the context of calculating the critical behavior of many systems and serves as a basis for a broad category of phase transition analysis [8].

1.3. THE SCALING HYPOTHESIS

We have seen already that the critical exponents serve to define the behavior of various observables as the critical point is approached and their calculation are a central focus of the study of phase transitions. In this Section, we will see that the long list of critical exponents are in fact closely related to each other and that only two of the exponents are required to entirely describe the systems critical behavior.

In Section 1.1.2 we noted that the correlation lengths of fluctuations diverge at the critical point. This makes the correlation length the only relevant length scale of the system and the system becomes *scale invariant*. That is to say, the physical properties of a system will be invariant if we were to rescale all lengths in the system by a common factor while at the same time adjusting external parameters such that the correlation length remained the same. Formally, this takes the form of the homogeneity relation for the singular portion of the free energy density (the portion of the free energy that exhibits the defining singularity of a thermodynamics phase transition)

$$f(r,h) = b^{-d} f(rb^{y_r}, hb^{y_h}) \tag{1.8}$$

and the correlation lengths

$$\xi = b\xi(rb^{y_r}, hb^{y_h}) \tag{1.9}$$

where b is an arbitrary (positive) rescaling factor, d is the spatial dimensionality of the system, and y_r & y_h are new critical exponents. This scaling form was first derived by Widom [9] on phenomenological grounds, but may be also derived from first principles using

renormalization group techniques [10]. From the homogeneity relationship (1.8) we may derive the thermodynamic observables of the system via differentiation of F. Accordingly, we arrive at scaling relations for the order parameter, susceptibility, and specific heat

$$\Psi \sim \frac{\partial f}{\partial h} = b^{y_h - d} X_\Psi(r b^{1/\nu}, h b^{y_h}) \tag{1.10}$$

$$\chi \sim \frac{\partial^2 f}{\partial h^2} = b^{2y_h - d} X_\chi(r b^{1/\nu}, h b^{y_h}) \tag{1.11}$$

$$C \sim \frac{\partial^2 f}{\partial r^2} = b^{2/\nu - d} X_C(r b^{1/\nu}, h b^{y_h}) \tag{1.12}$$

where X_Ψ, X_χ, and X_C are scaling functions of the order parameter, susceptibility and specific heat, respectively, defined via the appropriate derivatives of the free energy F. Since the rescaling factor b is arbitrary, we may choose it's value in a convenient way. In order to fix the first argument in the scaling functions, we choose $b = r^{-\nu}$ (this also has some physical meaning since, in effect, we are choosing the correlation lengths near the critical point $\xi \sim r^{-\nu}$). Then, for $h = 0$, we arrive at relationships for the order parameter, susceptibility, and specific heat critical exponents

$$\Psi \sim r^{(d - y_h)\nu} \equiv r^\beta \tag{1.13}$$

$$\chi \sim r^{(d - 2y_h)\nu} \equiv r^{-\gamma} \tag{1.14}$$

$$C \sim r^{d\nu - 2} \equiv r^{-\alpha}. \tag{1.15}$$

To make a connection to the critical isotherm exponent, we consider equation (1.10) for a scaling factor $b = h^{-1/y_h}$ chosen to fix the second argument. This gives another relationship for the critical isotherm exponent at the critical point $r = 0$

$$\Psi \sim h^{d/y_h - 1} \equiv h^{1/\delta} \tag{1.16}$$

and therefore a set of equations relating the thermodynamic critical exponents to one another:

$$(d - y_h)\nu = \beta \tag{1.17}$$

$$(d - 2y_h)\nu = -\gamma \tag{1.18}$$

$$d\nu - 2 = -\alpha \tag{1.19}$$

$$d/y_h - 2 = 1/\delta \tag{1.20}$$

Algebraic manipulation of these equations then provides the scaling relationships that connect the various critical exponents

$$\alpha = 2 - d\nu \tag{1.21}$$

$$2\beta + \gamma + \alpha = 2 \tag{1.22}$$

$$\beta(\delta - 1) = \gamma. \tag{1.23}$$

Based on the generality of the derivation of these scaling relationships, we expect that all critical systems must have exponents that satisfy these conditions. Given this fact, the above relationships may be used as checks on the final results of a critical exponent calculation, as we will see demonstrated in the calculations we perform in the following chapters.

1.4. QUENCHED DISORDER AND THE HARRIS CRITERION

The main focus of this dissertation is on the effects of disorder (e.g. impurities, doping, lattice vacancies) on the critical behavior of systems. In particular, we are interested in quenched, or time-independent disorder in these systems. While it may be intuitively clear that disorder may affect the critical behavior of a system, Harris derived a quantitative

criterion for the stability of the critical behavior of a clean system against the introduction of disorder [11]. Here, we will give a sketch of Harris' original 1974 derivation of his eponymous criterion.

Introduction of disorder to a system has the effect of modifying the critical temperature so that now we have a critical temperature $T_c(p)$, where p represents the fraction of missing interactions in the disordered system (i.e. $p = 1$ is the clean, undiluted case). Close to the critical point, we then have a relationship for the diverging correlation lengths

$$\xi \sim |T - T_c(p)|^{-\nu} \tag{1.24}$$

and our goal is to determine the width (or variance) of the spatial distribution of $T_c(p)$ in our system (since the disorder is randomly distributed throughout). The first step in determining this is to divide the system up into blocks of volume ξ^d, where d is the spatial dimensionality. Blocks of linear size ξ are chosen so we may treat them as statistically independent entities. Then, the number of missing interactions in a given block may be written as $\langle n \rangle = p\xi^d$. We may then write for the variance of the number of missing interactions in a block as

$$\sigma_n^2 \equiv \langle n^2 \rangle - \langle n \rangle^2 = \xi^d p(1-p) \tag{1.25}$$

Thus, the width of the distribution of the concentration of missing interactions in a given block is of order $\sigma_p^2 \sim [\xi^d p(1-p)]^{1/2}/\xi^d$. Then, using the linearity of the relationship between p and $T_c(p)$, we may conclude that the variance $\sigma_{T_c}^2$ of the distribution of $T_c(p)$ throughout the system is of order

$$\frac{\sigma_{T_c}^2}{T_c} \sim \frac{\sqrt{\xi^d p(1-p)}}{\xi^d}. \tag{1.26}$$

From here, we must ask ourselves if the originally chosen correlation lengths $\xi \sim |T - T_c(p)|^{-\nu}$ are self-consistent. That is, we must have a correlation length that is not larger than that which corresponds to a temperature $|T - T_c|/T_c = \sigma_{T_c}^2/T_c$. This gives as the requirement for self-consistency

$$\xi \leq |\sigma_{T_c}^2/T_c|^{-\nu} = \xi^{d\nu/2}[p(1-p)]^{-\nu/2} \tag{1.27}$$

which can only be satisfied if we have $d\nu/2 \geq 1$, or as it is typically written

$$d\nu > 2 \tag{1.28}$$

The 'equal to' portion of the expression has been dropped, as Harris' derivation which we have sketched here is too imprecise to account for $d\nu = 2$.

Harris' criterion indicates that the stability of a sharp, well-defined phase transition at the clean critical point is dependent on system dimensionality and it's correlation length critical exponent. If the Harris' criterion is not satisfied, then any introduction of disorder to the system will result in the destruction of the clean critical point and the general expectation that new critical behavior will emerge, with new critical exponents.

In the calculations to follow in this dissertation, we will see that the systems we investigate break the Harris criterion (i.e. have critical exponents such that $d\nu < 2$) and therefore we expect the system to exhibit new critical phenomenon upon the introduction of disorder. Additionally, once the new critical exponents have been calculated, the Harris criterion can also be used as a check for the validity of the new critical exponents (e.g. we require new exponents to satisfy $d\nu > 2$) [6].

1.5. QUANTUM PHASE TRANSITIONS

The discussion so far has been relevant to *classical* phase transitions which take place at finite temperatures. Classical phase transitions are the result of the competition between order parameter and thermal fluctuations of the system and for this reason, are also often called *thermal* phase transitions. In recent years, researchers have developed interest in another class of phase transitions, namely transitions that take place at the absolute zero of temperature. These zero-temperature phase transitions are transitions in the ground state of a many-body quantum systems that are a result of quantum fluctuations and therefore designated as *quantum phase transitions* [12].

The study of phase transitions that occur at the experimentally inaccessible absolute zero of temperature may sound like a purely academic issue. However, recent experimental and theoretical developments have shown that the existence of such zero temperature quantum critical points is key to understanding the behavior of many real-world condensed matter systems at low temperatures.

1.5.1. Quantum-to-Classical Mapping. As with most quantum phenomenon, the study of quantum phase transitions (QPTs) comes with many more theoretical complications than their classical counterparts. Fortunately, there is a fundamental correspondence between the thermodynamics of a d dimensional quantum system and a $d+1$ dimensional classical system that we may take advantage of. Therefore, to study the thermodynamics of QPTs, we may perform a *quantum-to-classical mapping* which allows us to study the thermodynamics of the quantum theory by analyzing a corresponding classical system, at the cost of an extra dimension in imaginary-time.

To see how the quantum-to-classical mapping works, we start from the central focus of statistical mechanics: the partition function

$$Z = \mathrm{tr}\left(e^{-\beta H}\right) \tag{1.29}$$

where $\beta = 1/k_B T$. In a classical system with a Hamiltonian of the form $H = H_{kin} + H_{pot}$, the exponential can be factorized and the partition function takes the form $Z = Z_{kin} Z_{pot}$, effectively decoupling the static and dynamic behavior of the system. The kinetic portion of the partition function is typically in the form of a product of Gaussian integrals and therefore does not exhibit the singularities of phase transitions. This allows the study of classical phase transitions via time-independent theories in d dimensions.

In the quantum case, the luxury of a decoupled partition function is not present. In general, the kinetic and potential parts of the Hamiltonian do not commute, and therefore the partition function cannot be factorized. This means that the static and dynamic portions of the quantum system are always coupled and a time-dependent theory is required to describe QPTs accurately.

The key to developing a time-dependent theory which may describe QPTs, is recognizing that the density operator $e^{-\beta \hat{H}}$ may be rewritten as a time-evolution operator by introducing an imaginary-time τ

$$\beta = \tau = -it/\hbar \tag{1.30}$$

where t represents the real time. This maps the inverse temperature onto the imaginary-time axis, where a zero temperature $\beta \to \infty$ system corresponds to infinity on the imaginary-time axis. Utilizing the imaginary-time mapping in combination with the Suzuki-Trotter decomposition of the exponential, the partition function may be factored and evaluated by allowing the decomposed time-evolution operators to act on the basis states of the quantum system in question. The end result (after performing the emerging sums and products) is a partition function whose Hamiltonian takes the form of a classical model in imaginary-time, with the classical temperature mapped to the ratio of quantum coupling parameters.

In our calculations to follow, this fundamental connection between the quantum and classical world allows us to investigate the quantum Hamiltonian of our system by means of a classical spin model for which we may use well-established algorithms to simulate. Of

course, we are still left with the task of interpreting these results in the extra imaginary-time dimension. The details of this portion of the calculation will be presented in the following chapters.

1.5.2. Scaling Revisited. The introduction of the imaginary-time axis in the description of QPTs has an effect on the homogeneity relationship for the classical free energy and thus the scaling forms for the observables of the system. We know that times near the critical point are related to the zth power of the correlation length $\tau \sim \xi^z$. Therefore, introducing the imaginary-time axis is equivalent to introducing another dimension which scales according to the zth power and generalizing (1.8) to the quantum case is simple. The quantum homogeneity relationship is then written as

$$F(r, h) = b^{(d+z)} F(rb^{1/\nu}, hb^{y_h}). \tag{1.31}$$

Here, r now represents the distance to a quantum critical point as a function of some non-thermal tuning parameter $r = (g - g_c)/g_c$. For many critical points (e.g. clean, undiluted systems), we have $z = 1$, thus providing a connection to the quantum-to-classical mapping discussed in the previous Section (i.e. the only difference in the scaling relationship reflects the correspondence $d \rightarrow (d+1)$). We will soon see that in general (e.g. the diluted systems we focus on) we may have any $z > 0$.

1.6. FINITE-SIZE SCALING

We have seen in Section 1.1.2 that phase boundaries are characterized by singularities in certain observables of a thermodynamic system. However, these singularities only truly exist in the thermodynamic limit. That is, in a system whose volume $V \rightarrow \infty$ or number of particles $N \rightarrow \infty$ approach infinity, while keeping the density N/V constant. In the remainder of this dissertation, we will be studying the properties of these phase boundaries via computer simulation, for which the system size is constrained by the limi-

tations of computational power. In the finite-sized systems used in simulations, *finite-size effects* become a significant factor in the critical behavior, with the singularities becoming rounded and the critical points being shifted from their true thermodynamic limit values [1]. Therefore, we must ask ourselves: how do we precisely determine the critical points and critical exponents in the presence of these finite-size effects?

To answer this question, we return to the classical homogeneity relationship for the free energy density (1.8). In the case of a finite-size system of linear size L, at the critical point $r = 0$ the correlation lengths can no longer diverge to infinity, but rather are restricted by the linear size of the system $\xi \sim r^{-\nu} \to L$. The classical homogeneity relationship may be generalized to account for finite-size effects as

$$f(r, h, L) = b^{-d} f(rb^{1/\nu}, hb^{y_h}, Lb^{-1}). \tag{1.32}$$

Choosing the arbitrary scale factor in a convenient way $b = L$ to fix the third argument in the scaling function, we then arrive at the finite-size scaling form for the free energy

$$f(r, h, L) = L^{-d} f(rL^{1/\nu}, hL^{y_h}) \tag{1.33}$$

from which we may derive the scaling forms for the remaining observables. Taking the appropriate derivatives for the order parameter, susceptibility and specific heat and using the relationships (1.17) - (1.19), we arrive at the finite-size scaling forms for $h = 0$

$$\Psi \sim L^{-\beta/\nu} X_\Psi(rL^{1/\nu}) \tag{1.34}$$

$$\chi \sim L^{\gamma/\nu} X_\chi(rL^{1/\nu}) \tag{1.35}$$

$$C \sim L^{\alpha/\nu} X_C(rL^{1/\nu}). \tag{1.36}$$

With these relationships, it is relatively clear to see that if we perform calculations right at the critical point $r = 0$, then the values of these observables scales with system size according a power-law relationship governed by their respective critical exponents. Therefore, determining the critical exponents of a system is simply a matter of power-law fits to the observables as a function of system size with $r = 0$. Of course, to utilize this technique, we need a way to reliably find the critical points $r = 0$ to suitable accuracy.

1.6.1. Critical Points. The key to determining the true thermodynamic limit critical point in the context of finite-size scaling is particular observables that are of scale dimension zero, or *dimensionless*. These are observables which, unlike (1.34) - (1.36), only depend on a homogeneous scaling function. A core example of such dimensionless observables – used extensively in the remainder of this work – is the *Binder cumulant* of the order parameter [13]

$$g = 1 - \frac{\langle \Psi^4 \rangle}{3\langle \Psi^2 \rangle^2} \tag{1.37}$$

and the reduced correlation length ξ/L. The finite-size scaling form for the Binder cumulant is easy to derive by simply plugging in (1.34) to (1.37)

$$g(r, L) = 1 - \frac{\langle \Psi \rangle^4}{3\langle \Psi^2 \rangle^2} = 1 - \frac{L^{-4\beta/\nu} X_{\Psi^4}(rL^{1/\nu})}{(L^{-2\beta/\nu} X_{\Psi^2}(rL^{1/\nu}))^2} = X_g(rL^{1/\nu}). \tag{1.38}$$

The factors of L cancel out in the Binder cumulant, leaving just the homogeneous scaling function X_g, making the observable scale dimension zero. Similarly, for the correlation length, the finite-size scaling form is

$$\xi = L X_\xi(rL^{1/\nu}) \tag{1.39}$$

for which it is easy to see that the reduced correlation length is only dependent on the scaling function X_ξ

$$\xi/L = X_\xi(rL^{1/\nu}) \tag{1.40}$$

and thus also scale dimension zero.

Crucially, since dimensionless variables are only dependent on their scaling functions, they have the convenient properties that at the critical point $r = 0$

$$g(0, L) = X_g(0) \qquad \xi/L(0, L) = X_\xi(0) \tag{1.41}$$

Therefore, to find the critical point in a numerical simulation of a finite-size system, we may scan across a range of the tuning parameter r for a set of system sizes L. Since the dimensionless observables will take on the exact same value at the critical point for different system sizes, the curves of g or ξ/L as a function of r for different system sizes will cross at exactly $r = 0$, allowing us to determine the critical point to essentially arbitrary accuracy (within computational limits).

1.6.2. Critical Exponents. Once the critical points have been determined to suitable accuracy, we are then tasked with finding the critical exponents. To accomplish this, we note that the finite-size scaling forms of the observables for which the critcal exponents are defined, take the form of power laws as a function of system size at the critical point $r = 0$

$$\Psi(0, L) = L^{-\beta/\nu} X_\Psi(0) \sim L^{-\beta/\nu} \tag{1.42}$$

$$\chi(0, L) = L^{\gamma/\nu} X_\chi(0) \sim L^{\gamma/\nu} \tag{1.43}$$

$$C(0, L) = L^{\alpha/\nu} X_C(0) \sim L^{\alpha/\nu}. \tag{1.44}$$

Additionally, we may calculate the correlation length critical exponent ν directly (more precisely $1/\nu$), by considering the derivative of the Binder cumulant and reduced correlation length with respect to r

$$\frac{d}{dr}\xi/L = L^{1/\nu} X_\xi(0) \sim L^{1/\nu} \tag{1.45}$$

$$\frac{d}{dr}g = L^{1/\nu} X_g(0) \sim L^{1/\nu}. \tag{1.46}$$

Therefore, we may simulate the system at $r = 0$ for a range of system sizes and perform power law fits of the observables to extract the critical exponents ν, β/ν, γ/ν and α/ν.

To summarize, calculating the critical behavior of a (clean, undiluted) system consists of two general steps. First, utilize the crossings of scale dimension zero variables as a function of the relevant external parameter to find $r = 0$ to a suitable accuracy. Once the critical point is determined, we may then simulate the system at $r = 0$ for a range of system sizes L. Power-law fits to the observables as a function of system size then provides an estimate for the relevant critical exponent. The precision of the resulting critical points and exponents is only limited by the system sizes one may reach with the available computational resources.

1.7. COLLECTIVE EXCITATIONS: HIGGS AND GOLDSTONE MODES

1.7.1. Continuous Symmetry Breaking. Symmetries and the breaking of symmetries play a vital role in modern physics from condensed matter to cosmological and high-energy systems. Phase transitions are great examples of symmetry breaking phenomena. The freezing of water from it's liquid state into the solid state breaks the translational symmetry of the liquid. Reducing ferromagnetic materials below their Curie temperature results in the magnetization spontaneously acquiring a magnitude and direction, breaking the rotational symmetry of the system above the Curie point. In the case of superfluids, the transition to the superfluid state breaks the U(1) continuous symmetry of the complex superfluid order parameter that characterizes the superfluid density.

A fundamental consequence of the breaking of a continuous symmetry of an N-component order parameter is the emergence of a massive (or gapped) *Higgs mode* – corresponding to fluctuations of the order parameter magnitude – and $N - 1$ massless (or gapless) *Goldstone modes* – corresponding to fluctuations in the order parameter phase [14, 15]. The emergence of these collective excitation modes is easily understood in the context of the Ginzburg-Landau-Wilson theory, which was discussed in Section 1.2.2.

We are concerned with the complex superfluid order parameter

$$\Psi = |\Psi| e^{i\phi}. \tag{1.47}$$

The action defining Ginzburg-Landau-Wilson theory (1.7) implies that the order parameter $\Psi(\mathbf{x})$ experiences a potential V that is symmetric in the disordered phase. This permits an equilibrium order parameter $\Psi = 0$ with a continuous rotational symmetry (i.e. a change in the phase ϕ leaves the system unchanged). As the critical point is approached, the symmetric potential begins to evolve into the so-called 'Mexican hat' potential. Once the critical point is crossed, the order parameter spontaneously obtains a magnitude and phase in accordance with the minimums of this new potential $\Psi = |\Psi| e^{i\phi} \neq 0$, therefore breaking the continuous symmetry of the disordered phase. The fluctuations of the order parameter about the minimums of the 'Mexican hat' potential define the Higgs and Goldstone modes.

The energy of the Higgs mode is expected to follow the divergence of the correlation times $\tau_c \sim r^{-z\nu}$ as the critical point is approached. This implies a Higgs energy ω_H

$$\omega_H \sim r^{z\nu} \tag{1.48}$$

which softens to zero as the critical point is approached. In the disordered phase the Higgs and 'Goldstone' mode energies are degenerate so that we have $\omega_G = \omega_H$ and the Goldstone mode becomes gapless $\omega_G = 0$ in the ordered phase.

1.7.2. Linear Response Theory. Studies of a systems dynamical properties are most conveniently done in the context of *linear response theory* [16]. The basis of this approach assumes that sufficiently weak perturbations to a system at a driving frequency ω (e.g. by means of AC currents) will invoke a response in the system of equal frequency ω. In others words, observing a response in the system at a frequency different from the driving frequency $\neq \omega$ indicates a strong *non-linear* response. Perturbations of these kind may be described in terms of a generalized susceptibility χ which describes a response X

as a result of a driving force F as

$$X_i(\mathbf{x},\omega) \approx \int d^d r' \chi_{ij}(\mathbf{x},\mathbf{x}',\omega) F_j(r',\omega) \tag{1.49}$$

where the indices i and j denote the various components of the driving force and the systems response. The expression is only considered an approximation as we are neglecting any non-linear responses higher-order in the driving force (e.g. $O(F^2)$ and higher). For translationally invariant systems, the response function depends only on the difference between the spatial coordinates $\chi_{ij}(\mathbf{x},\mathbf{x}',\omega) = \chi_{ij}(\mathbf{x}-\mathbf{x}',\omega)$ and the spatial Fourier transform of (1.49) is simplified

$$X_i(\mathbf{q},\omega) = \chi_{ij}(\mathbf{q},\omega) F(\mathbf{q},\omega). \tag{1.50}$$

In this form it is easy to conceptualize the fact that a peak in the response $X_i(\mathbf{q},\omega)$ corresponds to an excitation in the system with frequency ω and momentum $\mathbf{q}$.

1.7.3. Kubo Formula. While linear response theory provides a significant simplification in the conceptual understanding of dynamical responses in condensed matter systems, it provides very little in terms of methods of calculation. Luckily, a mathematical connection may be made between the thermal equilibrium properties of a system and it's associated response function. This mathematical connection is most well-known as the *fluctuation-dissipation theorem*. As the name suggests, this theorem establishes a formal relationship between the thermal fluctuations of a system and it's dissipation properties (e.g. the response function corresponding to the relevant fluctuation). The derivation in terms of the functional field integral of the system results in defining relationship

$$\chi(\mathbf{q},\omega) = \langle X(\tau)X(0)\rangle - \langle X(\tau)\rangle\langle X(0)\rangle. \tag{1.51}$$

With this formula, we may calculate the susceptibility χ by calculating thermal expectation values of the relevant observable and it's product. This makes calculation of χ a rather straight-forward process in the context of Monte Carlo simulations whose central outputs are typically these thermal expectation values.

PAPER

I. QUANTUM CRITICAL BEHAVIOR OF THE SUPERFLUID-MOTT GLASS TRANSITION

Thomas Vojta[1], Jack Crewse[1], Martin Puschmann[1,2], Daniel Arovas[3], Yuri Kiselev[3]
[1] Department of Physics, Missouri University of Sci. and Tech., Rolla, MO 65409, USA
[2] Institute of Physics, Techinsche Universität Chemnitz, 09107 Chemnitz, Germany
[3] Department of Physics, University of California, La Jolla, California 92093, USA

ABSTRACT

We investigate the zero-temperature superfluid to insulator transitions in a diluted two-dimensional quantum rotor model with particle-hole symmetry. We map the Hamiltonian onto a classical $(2 + 1)$-dimensional XY model with columnar disorder which we analyze by means of large-scale Monte Carlo simulations. For dilutions below the lattice percolation threshold, the system undergoes a generic superfluid-Mott glass transition. In contrast to other quantum phase transitions in disordered systems, its critical behavior is of conventional power-law type with universal (dilution-independent) critical exponents $z = 1.52(3)$, $\nu = 1.16(5)$, $\beta/\nu = 0.48(2)$, $\gamma/\nu = 2.52(4)$, and $\eta = -0.52(4)$. These values agree with and improve upon earlier Monte-Carlo results [Phys. Rev. Lett. 92, 015703 (2004)] while (partially) excluding other findings in the literature. As a further test of universality, we also consider a soft-spin version of the classical Hamiltonian. In addition, we study the percolation quantum phase transition across the lattice percolation threshold; its critical behavior is governed by the lattice percolation exponents in agreement with recent theoretical predictions. We relate our results to a general classification of phase transitions in disordered systems, and we briefly discuss experiments.

1. INTRODUCTION

Zero-temperature phase transitions between superfluid and insulating ground states in systems of disordered interacting bosons are prototypical quantum phase transitions with experimental applications ranging from helium absorbed in vycor [1, 2] to Josephson junction arrays [3, 4], superconducting films [5, 6], doped quantum magnets in high fields [7, 8, 9], and to ultracold atoms in disordered optical lattices [10, 11, 12].

For generic disorder, the two bulk phases, viz. superfluid and Mott insulator, are separated by another phase, the Bose glass which is a compressible gapless insulator [13, 14, 15]. It can be understood as the Griffiths phase [16, 17, 18] of the superfluid-insulator transition in which rare large regions of local superfluid order coexist with the insulating bulk. The quantum phase transition between superfluid and Bose glass has been studied in great detail using various analytical and computational techniques. It has recently reattracted considerable attention because new analytical [19] and numerical [20, 21, 22, 23] findings have challenged the scaling relation[13, 14] $z = d$ between the dynamical exponent z and the space dimensionality d (References [19, 20, 21, 22, 23] also contain long lists of references to earlier work.)

In the presence of particle-hole symmetry, the glassy Griffiths phase between superfluid and Mott insulator has a different character: it is the incompressible gapless Mott glass (also called the random-rod glass) [24, 25]. The quantum phase transition between superfluid and Mott glass has attracted less attention than the Bose glass transition. Moreover, the available quantitative results for two space dimensions do not agree with each other. Monte Carlo simulations of a link-current model [26] yielded a dynamical critical exponent $z = 1.5(2)$ and a correlation function exponent $\eta = -0.3(1)$. [1] A numerical strong-disorder renormalization group study of a particle-hole symmetric quantum rotor model gave $z = 1.31(7)$, a correlation length exponent $\nu = 1.09(4)$, and $\gamma/\nu = 1.1(2)$ where γ is the order parameter susceptibility exponent [27]. The Fisher relation $2 - \eta = \gamma/\nu$

[1] Here, the numbers in parentheses are the errors of the last digits.

then implies $\eta = 0.9(2)$. Furthermore, a recent Monte Carlo study of a quantum rotor model[28] reported good scaling by setting z to its clean value $z = 1$ which resulted in $\nu = 0.96(6)$. All these models are expected to be in the same universality class. The critical behavior of the superfluid-Mott glass quantum phase transition in two dimensions must thus be considered an open question.

To address this question, we consider a site-diluted two-dimensional quantum rotor model with particle-hole symmetry. After mapping this Hamiltonian onto a classical $(2+1)$-dimensional XY model with columnar defects, we perform large-scale Monte Carlo simulations for lattices with up to 11 million sites, averaging over 10 000 to 50 000 disorder configurations. The data are analyzed by a finite-size scaling technique[29, 30, 31, 32] that does not require prior knowledge of the dynamical exponent z. We also include the leading corrections to scaling. Our results can be summarized as follows: The system features two distinct quantum phase transitions. For dilutions p below the percolation threshold p_c of the lattice, we find a superfluid-Mott glass transition characterized by universal (dilution-independent) critical behavior with exponent values $z = 1.52(3)$, $\nu = 1.16(5)$, $\beta/\nu = 0.48(2)$, $\gamma/\nu = 2.52(4)$, and $\eta = -0.52(4)$. The transition across the lattice percolation threshold p_c falls into a different universality class. Its simulation data can be fitted well with the theory developed in Reference [33] which yields critical exponents that can be expressed in terms of the classical percolation exponents and take the rational values $z = 91/48$, $\beta/\nu = 5/48$, $\gamma/\nu = 59/16$, and $\eta = -27/16$.

The rest of the paper is organized as follows. Section 2 introduces the quantum rotor Hamiltonian, the mapping to the classical XY model, and the finite-size scaling technique. Monte Carlo simulations for both the generic ($p < p_c$) transition and the percolation transition are discussed in Section 3. We conclude in Section 4.

2. THEORY

2.1. DILUTED ROTOR MODEL

The starting point is a site-diluted quantum rotor model on a square lattice given by the Hamiltonian

$$H = \frac{U}{2} \sum_i \epsilon_i (\hat{n}_i - \bar{n}_i)^2 - J \sum_{\langle ij \rangle} \epsilon_i \epsilon_j \cos(\hat{\phi}_i - \hat{\phi}_j) \ . \tag{1}$$

Here, $\hat{n}_i$ is the number operator at site i, $\hat{\phi}_i$ is the phase operator, and U and J represent the charging energy and the Josephson coupling, respectively. $\bar{n}_i$ is the offset charge at site i. In the Josephson term, $\langle ij \rangle$ refers to pairs of nearest neighbors. The quenched random variables ϵ_i implement the site dilution. They are independent of each other and take the values 0 (vacancy) with probability p and 1 (occupied site) with probability $1 - p$.

As we are interested in the superfluid-Mott glass transition, we set all offset charges $\bar{n}_i$ to zero and consider commensurate (integer) filling $\langle \hat{n} \rangle$. In this case, the disorder is purely off-diagonal, and the model is particle-hole symmetric. The qualitative features of its phase diagram are well understood [14, 25]. If the charging energy dominates, $U \gg J$, the ground state is a Mott insulator. In the opposite limit, $J \gg U$, the ground state is a superfluid as long as the dilution p is below the lattice percolation threshold p_c. For $p > p_c$, the lattice consists of disconnected clusters and a long-range ordered superfluid state is impossible.

In the case of particle-hole symmetry, the quantum rotor model (1) can be mapped [34] onto a classical (2+1)-dimensional XY model on a cubic lattice having the Hamiltonian

$$H_{\rm cl} = -J_s \sum_{\langle i,j \rangle, t} \epsilon_i \epsilon_j \mathbf{S}_{i,t} \cdot \mathbf{S}_{j,t} - J_\tau \sum_{i,t} \epsilon_i \mathbf{S}_{i,t} \cdot \mathbf{S}_{i,t+1} \tag{2}$$

where $\mathbf{S}_{i,t}$ is an O(2) unit vector at the lattice site with spatial coordinate i and "imaginary time" coordinate t. The coupling constants J_s/T and J_τ/T are determined by the original quantum rotor Hamiltonian (1) with T being an effective "classical" temperature, not equal

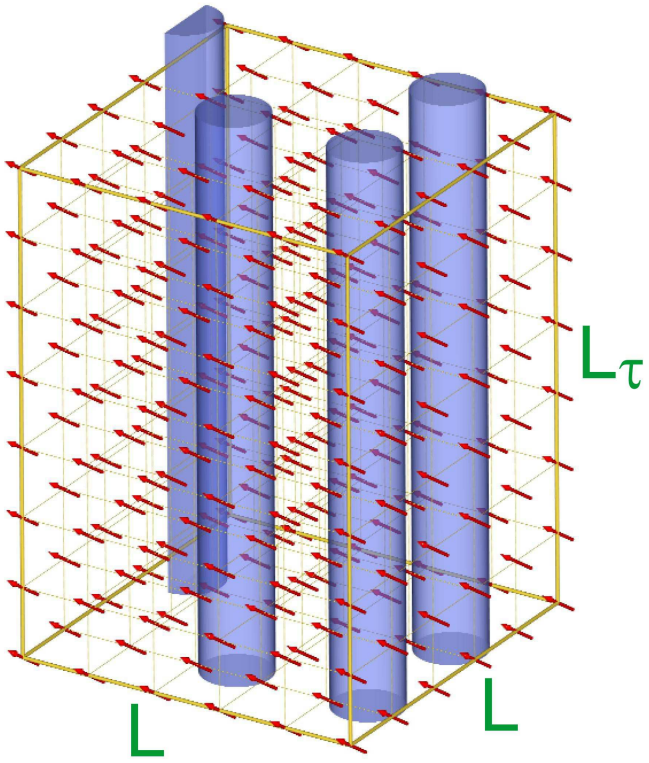

Figure 1. Sketch of the classical XY model (2).The arrows represent the classical unit vectors **S**, and the tubes show the locations of the vacancy columns.

to the real physical temperature. (The physical temperature of the quantum system (1) maps onto the inverse system size in imaginary time direction of the classical model.) Due to universality, the exact values of J_s and J_τ are not important for the critical behavior. We therefore set $J_s = J_\tau = 1$ and drive the XY model (2) through the transition by varying the classical temperature T. Because the vacancy positions do not depend on the imaginary time coordinate t, the defects in the classical model (2) are columnar, i.e., the disorder is perfectly correlated in the imaginary time direction (see Figure 1).

In the clean undiluted limit $p = 0$, the Hamiltonian (2) simplifies to the usual three-dimensional XY model. The correlation length critical exponent of the three-dimensional XY universality class takes the value $\nu \approx 0.6717$ (see, e.g., Reference [35]). This value violates the Harris criterion [36] $d\nu > 2$ where $d = 2$ is the number of dimensions in

which there is randomness. Consequently, the three-dimensional clean XY critical point is unstable against columnar defects, and we expect the diluted system to feature a different critical behavior.

2.2. ANISOTROPIC FINITE-SIZE SCALING

Finite-size scaling [37, 38] is a powerful tool for analyzing Monte Carlo data. Particularly useful are quantities of scale dimension zero such as the (average) Binder cumulant

$$g_{\mathrm{av}} = \left[1 - \frac{\langle |\mathbf{m}|^4 \rangle}{3 \langle |\mathbf{m}|^2 \rangle^2} \right]_{\mathrm{dis}}, \tag{3}$$

where $\mathbf{m} = (1/N) \sum_{i,\tau} \mathbf{S}_{i,\tau}$ is the order parameter (N denotes the number of lattice sites). $[\ldots]_{\mathrm{dis}}$ refers to the disorder average and $\langle \ldots \rangle$ denotes the Monte Carlo average for each sample. In an isotropic system with a single relevant length scale, it takes the scaling form $g_{\mathrm{av}}(r, L) = X(rL^{1/\nu})$. Here L is the linear system size, $r = (T - T_c)/T_c$ is the distance from criticality, and X is a scaling function. This scaling form implies that g_{av} vs. r curves for systems of different sizes L all cross at criticality, $r = 0$, having the value $g_{\mathrm{av}}(0, L) = X(0)$. This can be used to find the critical point with high accuracy. Moreover, the slopes of the g_{av} vs. r curves at $r = 0$ vary as $L^{1/\nu}$ which can be used to measure ν.

As the quenched disorder in our Hamiltonian (2) breaks the symmetry between the space and imaginary time directions, we need to distinguish the linear system size L in the two space directions from the size L_τ in the imaginary time direction. (L_τ corresponds to the inverse physical temperature of the original quantum model (1).) If the putative disordered critical point fulfills conventional power-law dynamical scaling, the finite-size scaling form of the average Binder cumulant then reads

$$g_{\mathrm{av}}(r, L, L_\tau) = X_{g_{\mathrm{av}}}(rL^{1/\nu}, L_\tau / L^z) \tag{4}$$

where z is the dynamical critical exponent, and $X_{g_{\rm av}}$ is the dimensionless scaling function which now depends on two arguments. Note that some quantum phase transitions in disordered systems feature exotic activated dynamical scaling instead of power-law scaling, for example the ferromagnetic transition in the random transverse-field Ising model [39, 40], the pairbreaking superconductor-metal quantum phase transition [41, 42, 43, 44, 45], and magnetic transitions in itinerant systems [46, 47]. For activated dynamical scaling, the scaling combination L_τ/L^z in Eq. (4) needs to be replaced by $\ln(L_\tau)/L^\psi$ where ψ is the tunneling exponent. Based on the classification of disordered quantum phase transitions developed in References [48, 18], we do not expect the superfluid-Mott glass transition to show activated scaling. We will return to this point in the concluding section.

How can one perform a finite-size scaling analysis of Monte Carlo data based on the scaling form (4) of the average Binder cumulant? If the value of z is known, the analysis is as simple as in the isotropic case: One chooses system sizes L and L_τ such that $L_\tau = c\, L^z$ were c is a constant. Then the $g_{\rm av}$ vs. r curves for systems of different sizes cross at criticality [with the value $g_{\rm av}(0, L, c\, L^z) = X_{g_{\rm av}}(0, c)$] which can be used to locate the critical point. However, in the absence of a value for z, this approach breaks down because the correct shapes (aspect ratios) of the samples are not known.

A method for finding the correct sample shape within the simulations [29, 30, 31, 32] can be based on the following property of the Binder cumulant: For fixed L, $g_{\rm av}$ as a function of L_τ has a peak at position $L_\tau^{\rm max}$ and value $g_{\rm av}^{\rm max}$. The peak position marks the *optimal* sample shape, where the ratio L_τ/L behaves like the corresponding ratio of the correlation lengths in time and space directions, ξ_τ/ξ_s. (If the aspect ratio deviates from the optimal one, the system can be decomposed into independent units either in space or in time direction, and thus $g_{\rm av}$ decreases.) At criticality, $L_\tau^{\rm max}$ must be proportional to L^z, fixing the second argument of the scaling function $X_{g_{\rm av}}$. This implies that the peak value $g_{\rm av}^{\rm max}$ at criticality is independent of L and that the $g_{\rm av}$ vs. r curves of samples of the optimal shape ($L_\tau = L_\tau^{\rm max}$) cross at $r = 0$.

In our simulations, we use an iterative approach. We start from a guess for z and the corresponding sample shapes. The approximate crossing of the $g_{\rm av}$ vs. r curves for these samples gives an estimate for T_c. At this temperature, we next analyze $g_{\rm av}$ as a function of L_τ for fixed L. The values of $L_\tau^{\rm max}$ give improved estimates for the optimal sample shapes and thus for z. After iterating this procedure three or four times, the values of T_c and z will have converged with reasonable accuracy.

Once z and T_c are determined, the finite-size scaling analysis proceeds as usual, based on the scaling forms

$$m = L^{-\beta/\nu} X_m(rL^{1/\nu}, L_\tau/L^z) \,, \tag{5}$$

$$\chi = L^{\gamma/\nu} X_\chi(rL^{1/\nu}, L_\tau/L^z) \tag{6}$$

for the order parameter m and its susceptibility χ. Here, X_m and X_χ are dimensionless scaling functions, and β and γ are the order parameter and susceptibility critical exponents, respectively.

In addition to these thermodynamic quantities, we also calculate the correlation lengths ξ_s and ξ_τ is the space and imaginary time directions, respectively. They are obtained, as usual, from the second moment of the spin-spin correlation function [49, 50, 51] and can be expressed in terms of the Fourier transform $\tilde{G}(q_s, q_\tau)$ of the correlation function,

$$\xi_s = \left[\left(\frac{\tilde{G}(0,0) - \tilde{G}(q_{s0},0)}{q_{s0}^2 \, \tilde{G}(q_{s0},0)} \right)^{1/2} \right]_{\rm dis} \,, \tag{7}$$

$$\xi_\tau = \left[\left(\frac{\tilde{G}(0,0) - \tilde{G}(0,q_{\tau 0})}{q_{\tau 0}^2 \, \tilde{G}(0,q_{\tau 0})} \right)^{1/2} \right]_{\rm dis} \,. \tag{8}$$

Here, $q_{s0} = 2\pi/L$ and $q_{\tau 0} = 2\pi/L_\tau$ are the minimum values of the wave numbers q_s and q_τ that fit into a system of linear size L and L_τ in space and imaginary time direction, respectively. The reduced correlation lengths ξ_s/L and ξ_τ/L_τ have scale dimension zero,

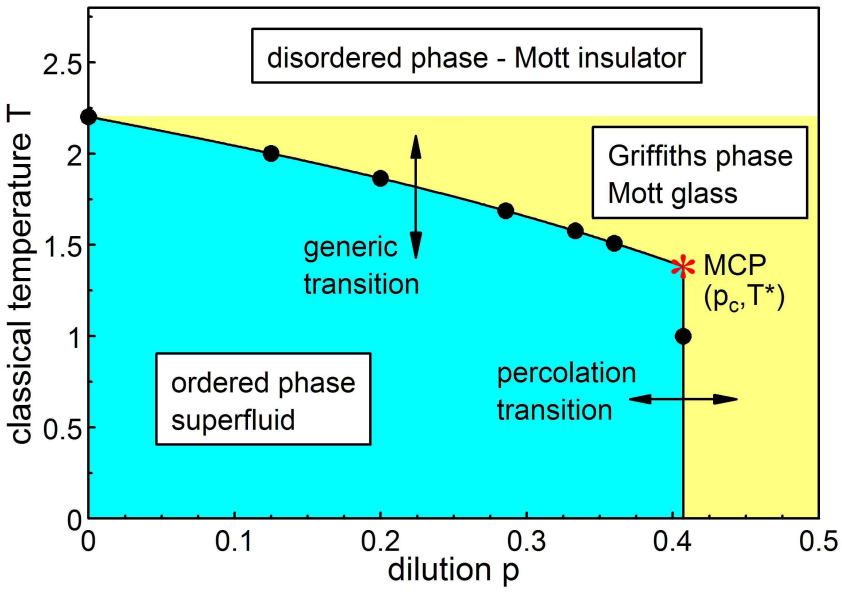

Figure 2. Phase diagram of the classical XY model (2) as a function of classical temperature and dilution. MCP is the multicritical point that separates the generic and percolation transitions. The big dots mark the numerically determined transition points. The lines are guides for the eye only.

their scaling forms therefore read

$$\xi_s/L = X_{\xi_s}(rL^{1/\nu}, L_\tau/L^z) , \tag{9}$$

$$\xi_\tau/L_\tau = X_{\xi_\tau}(rL^{1/\nu}, L_\tau/L^z) . \tag{10}$$

3. MONTE CARLO SIMULATIONS

3.1. OVERVIEW

Our Monte Carlo simulations of the classical XY model (2) combine the Wolff cluster algorithm [52] with conventional Metropolis updates [53]. Specifically, a full Monte Carlo sweep consists of a Metropolis sweep over the lattice followed by a Wolff sweep. (A Wolff sweep is defined as a number of cluster flips such that the total number of flipped spins equals the number of lattice sites.) The Wolff algorithm greatly reduces the critical slowing

down, and the Metropolis updates equilibrate small disconnected clusters of sites that are missed in the construction of the Wolff clusters (this becomes important at higher dilutions p).

We simulate systems with linear sizes up to $L = 150$ in space direction and up to $L_\tau = 1792$ in the imaginary time direction at dilutions $p = 0$, 1/8, 1/5, 2/7, 1/3, 9/25 and the percolation threshold $p_c = 0.407253$.

The simulation of disordered systems requires a high numerical effort because many samples with different disorder configurations need to be studied to compute averages, variances, and distributions of observables. For good performance, one must thus carefully optimize the number n_s of samples (i.e., disorder configurations) and the number n_m of measurements during the simulation of each sample. Based on the consideration in References [54, 55, 31, 32, 56], we have chosen rather short runs of $n_m = 500$ full sweeps per sample (with a measurement after each sweep) but large numbers of disorder configurations ranging from $n_s = 10\,000$ to $50\,000$ depending on the system size. The equilibration period is taken to be 100 full sweeps, significantly longer than the actual equilibration times that reach 30 to 40 sweeps at maximum. Short Monte Carlo runs can lead to biases in some of the observables. To eliminate these, we have implemented improved estimators along the lines discussed in the appendix of Reference [56].

The phase diagram resulting from these simulations is shown in Figure 2. The critical temperature $T_c(p)$ decreases with increasing dilution from its clean value $T_c(0)$, as expected. For dilutions above the percolation threshold $p_c = 0.407253$, the lattice consists of disconnected finite-size clusters. Therefore, long-range superfluid order is impossible. Right at p_c, there is an infinite cluster of dimension $1 + d_f$ where $d_f = 91/48$ is the dimensionality of the critical percolation cluster in two dimensions, and the extra 1 stems from the imaginary time direction. As $1 + d_f$ is larger than the lower critical dimension $d_c^- = 2$ of the XY model, the XY model on the critical percolation cluster orders below a multicritical temperature T^*. This implies that the phase boundary coincides with the

classical percolation threshold for $T < T^*$ (see also Reference [57]). We thus identify two different phase transitions, (i) the generic superfluid-Mott glass transition for $p < p_c$ and (ii) a percolation transition across the lattice percolation threshold.

In the following sections, we discuss the critical behaviors of these transitions in detail. To test our codes, we have also studied the clean limit $p = 0$ using system sizes up to 224^3 sites. By analyzing the crossings of the Binder cumulant and the reduced correlation length, we find a critical temperature $T_c(0) = 2.201844(4)$. Finite-size scaling then gives the critical exponents $\beta/\nu = 0.518(3)$, $\gamma/\nu = 1.961(3)$, and $\nu = 0.673(2)$. Within their errors, they agree well with high-precision results for the three-dimensional XY universality class [35].

As a further test for the universality of the (generic) critical behavior, we also perform exploratory simulations of a soft-spin version of the classical Hamiltonian. They are discussed in Section 3.4.

3.2. GENERIC SUPERFLUID-MOTT GLASS TRANSITION

To analyze the critical behavior of the generic transition occurring for $0 < p < p_c$, we consider five different dilutions, $p = 1/8$, 1/5, 2/7, 1/3, and 9/25. As described in Section 2.2, we use an iterative procedure that consists of two types of simulation runs. The first are runs right at T_c for systems with several different L_τ for each L. Finite-size scaling of the Binder cumulant at T_c as a function of L and L_τ gives the optimal sample shapes and the dynamical exponent z. In the second set of simulations, we vary the temperature over a range in the vicinity of T_c, but we consider only the optimal shapes found in the first part. Finite-size scaling of the order parameter, susceptibility, Binder cumulant, and correlation length as functions of L and T then yields the critical exponents β/ν, γ/ν, and ν.

The inset of Figure 3 shows the Binder cumulant g_{av} as a function of L_τ for several $L = 10$ to 100 at the estimated critical temperature $T_c = 1.577$ for dilution $p = 1/3$. As expected at the critical point, the maximum Binder cumulant $g_{\mathrm{av}}^{\mathrm{max}}$ for each of the curves

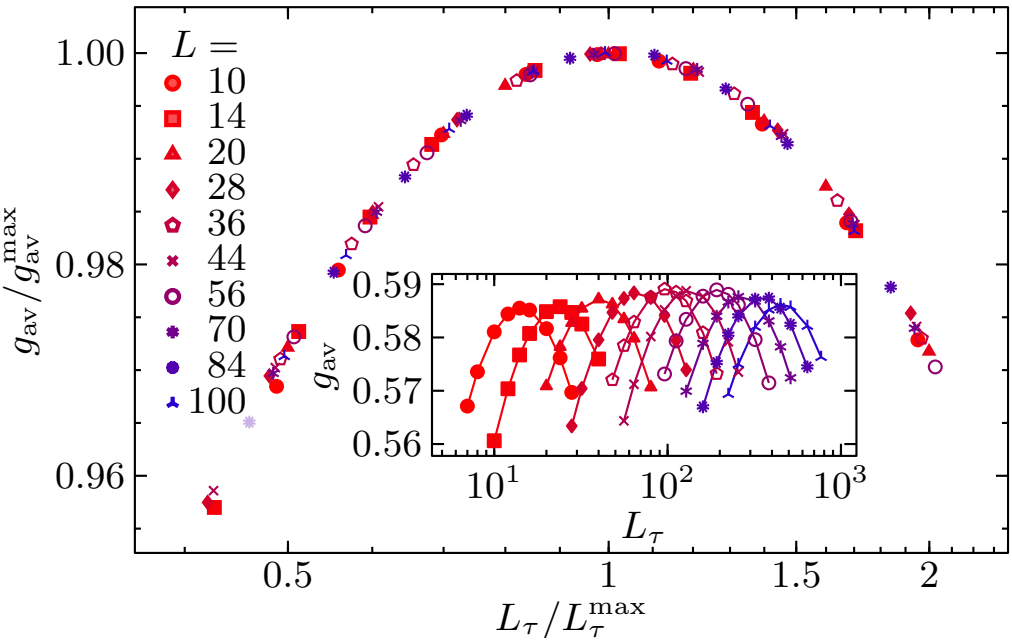

Figure 3. Binder cumulant $g_{\rm av}$ as a function of L_τ for several L at the critical temperature $T_c = 1.577$ for dilution $p = 1/3$. The relative statistical error of $g_{\rm av}$ is between 0.05% and 0.1%. Inset: Raw data $g_{\rm av}$ vs. L_τ. Main panel: Scaling plot $g_{\rm av}/g_{\rm av}^{\rm max}$ vs. $L_\tau/L_\tau^{\rm max}$.

does not depend on L. (The remaining weak variation visible in the Figure can be attributed to corrections to scaling, see below.) To generate a scaling plot that tests the scaling form (4), we now fit each $g_{\rm av}$ vs. L_τ curve with an inverted parabola in $\ln L_\tau$. The vertex of this parabola yields the position $L_\tau^{\rm max}$ of the maximum and its value $g_{\rm av}^{\rm max}$. When plotting $g_{\rm av}/g_{\rm av}^{\rm max}$ vs. $L_\tau/L_\tau^{\rm max}$ the data scale very well, as can be seen in the resulting scaling plot in the main panel of Figure 3. This demonstrates that the Binder cumulant fulfills Eq. (4) with high accuracy. We have created the corresponding scaling plots for all the other dilutions, $p = 1/8$, 1/5, 2/7, and 9/25, with analogous results. [2]

[2]For low dilutions p, the parabola fits of $g_{\rm av}$ vs. L_τ are affected by corrections to scaling for small L and L_τ. We thus slightly adjust $L_\tau^{\rm max}$ and $g_{\rm av}^{\rm max}$ to further improve the quality of the data collapse onto a common master curve. This applies to the four smallest system sizes L for $p = 1/8$ and 1/5 and the three smallest sizes for $p = 2/7$. The resulting change of the value of z is about 0.01, well below the error due to the uncertainty in T_c.

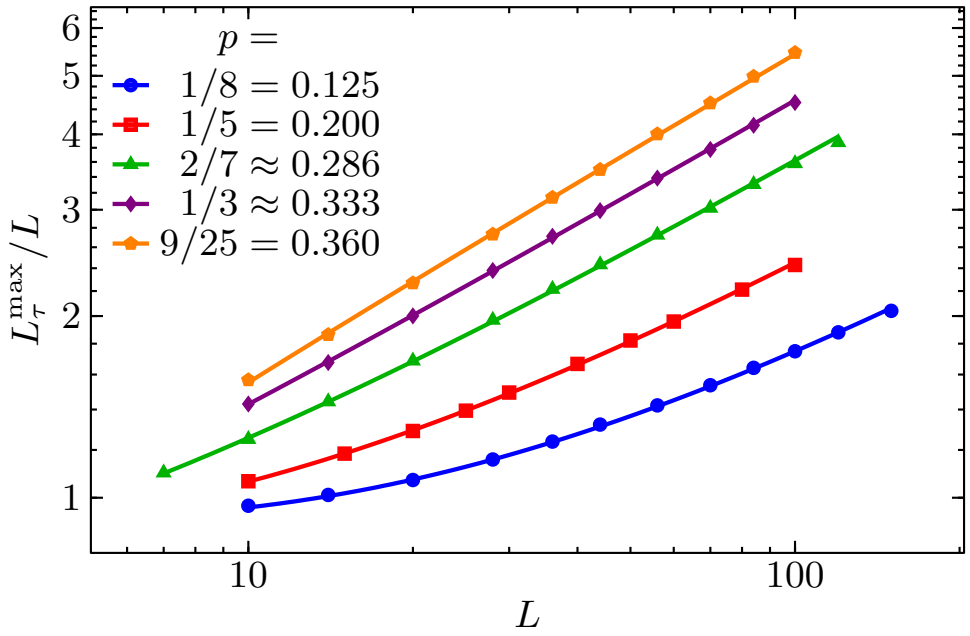

Figure 4. Double logarithmic plot of $L_\tau^{\max}/L$ vs. L for several dilutions p below the percolation threshold. Solid lines at fits to $L_\tau^{\max} = aL^z(1 + bL^{-\omega})$ giving $z = 1.526(5)$ and $\omega = 0.76(2)$. The statistical errors of the data are well below a symbol size (The statistical error of $L_\tau^{\max}$ is determined by repeating the scaling analysis for 1000 synthetic data sets that add to the original data set a Gaussian random noise that corresponds to the uncertainties of the data.)

To determine the dynamical critical exponent z, we now analyze the dependence of the positions $L_\tau^{\max}$ of the maximum on L. According to Eq. (4), we expect the power-law dependence $L_\tau^{\max} \sim L^z$. In Figure 4, we plot $L_\tau^{\max}$ vs. L for all dilutions $p < p_c$. The curves show significant deviations from pure power-law behavior, in particular for the smaller dilutions, indicating that the crossover from clean to disordered critical behavior is slow. The resulting corrections to scaling are strong and cannot be neglected. Pure power-law fits of the data would therefore only yield effective, scale-dependent exponents. To determine the true asymptotic exponents, we include the leading corrections to scaling via the ansatz $L_\tau^{\max} = aL^z(1 + bL^{-\omega})$ with universal (dilution-independent) critical exponents z and ω but dilution-dependent prefactors a and b. The exponent values resulting from a combined fit of the data for all five dilutions are $z = 1.526(5)$ and $\omega = 0.76(2)$. The

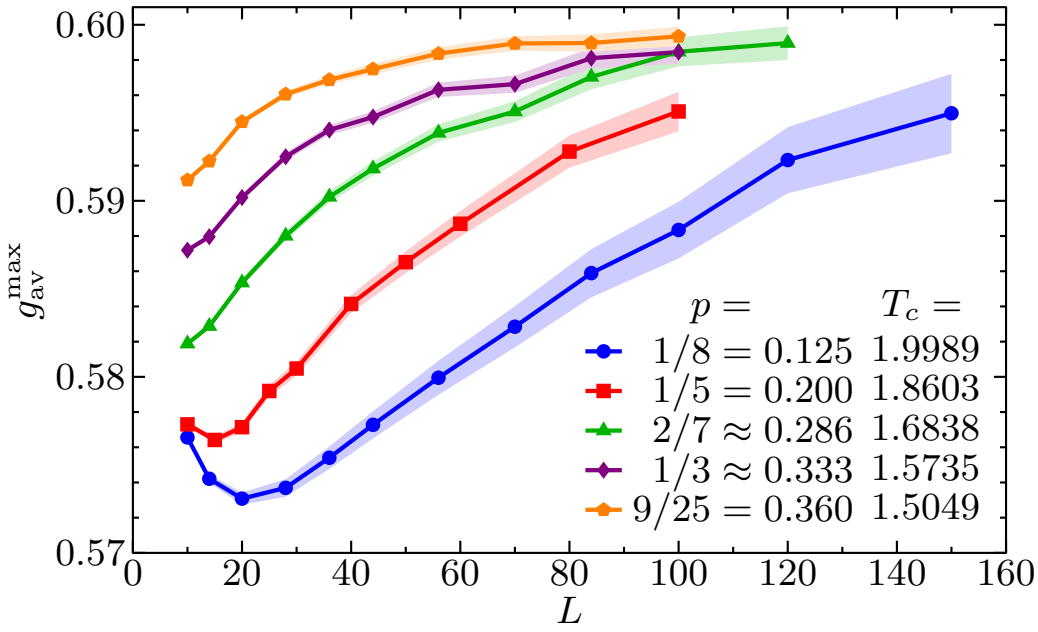

Figure 5. $g_{\rm av}^{\rm max}$ vs. L at the improved estimates for T_c. The statistical errors of the data points are about a symbol size or smaller. The shading represents the range of $g_{\rm av}^{\rm max}$ values for temperatures T within $T_c \pm 0.0002$ and is intended to illustrate to what extent the extrapolation depends on T. Based on these data we estimate that the error of T_c does not exceed 0.001.

fit is of good quality giving $\tilde{\chi}^2 \approx 1.4$. [We denote the reduced sum of squared errors of the fit (per degree of freedom) by $\tilde{\chi}^2$ to distinguish it from the susceptibility χ.] The fit is also robust against removing complete data sets or removing points from the upper or lower end of each set. Interestingly, the leading corrections to scaling appear to vanish somewhere between $p = 1/3$ and 9/25, as the prefactor b of the correction term changes sign. Correspondingly, pure power-law fits of the $p = 1/3$ and 9/25 data yield $z = 1.502$ and 1.546, respectively. These values are close to the estimate from the combined fit and nicely bracket it on both sides. An additional significant source of errors is the uncertainty of the critical temperature. To assess its effect on the dynamical exponent, we repeat the $L_\tau^{\rm max}$ vs. L analysis (for dilutions $p = 1/3$ and 9/25) at temperatures slightly above and below our

estimated T_c ($\Delta T_c \approx 0.003$, roughly at the boundaries of our confidence intervals). This leads to shifts in z of about 0.01 to 0.02. Our final estimate for the dynamical critical exponent therefore reads $z = 1.52(3)$.

To find the remaining critical exponents, we now turn to the Monte Carlo runs that use the optimal sample shapes $(L, L_\tau^{\max})$. According to Eqs. (5) and (6), β/ν and γ/ν can be obtained from the L dependence of the order parameter and susceptibility at T_c of the optimally shaped samples. As we expect corrections to scaling to be important, we again include subleading terms in our fit functions, $m = aL^{-\beta/\nu}(1 + bL^{-\omega})$ for the order parameter and $\chi = aL^{\gamma/\nu}(1 + bL^{-\omega})$ for the susceptibility. Here β/ν, γ/ν, and ω are the universal, dilution-independent critical exponents while the coefficients a and b are again non-universal. (Note that a and b generally differ from quantity to quantity; we use the same symbols to avoid cluttering up the notation too much.) When performing fits of our data to these expressions, we noticed, however, that the quality of the fits is extremely sensitive to small changes of the estimates for T_c (much more so than in the analysis of the dynamical exponent z above). To determine higher accuracy estimates of T_c, we use the criterion that the value of $g_{\rm av}^{\max}$ at criticality should approach a *dilution-independent* constant with $L \to \infty$ at a universal critical point. Varying T until this criterion is fulfilled yields improved estimates for the critical temperatures, viz. $T_c = 1.9989$ for $p = 1/8$, $T_c = 1.8603$ for $p = 1/5$, $T_c = 1.6838$ for $p = 2/7$, $T_c = 1.5735$ for $p = 1/3$, and $T_c = 1.5049$ for $p = 9/25$. We estimate the error of these values to be about 0.001. Figure 5 shows the resulting dependence $g_{\rm av}^{\max}$ on L. In the large-L limit, $g_{\rm av}^{\max}$ approaches the value 0.599(2). Note that the non-monotonic behavior of $g_{\rm av}^{\max}$ for weak dilutions suggests that at least two corrections to scaling terms contribute at small L.

Using the improved critical temperatures, we now proceed to determine β/ν and γ/ν. Figure 6 shows the order parameter m at T_c as a function of L for all dilutions $p < p_c$. The combined fit of all data to $m = aL^{-\beta/\nu}(1 + bL^{-\omega})$ is of good quality ($\tilde{\chi}^2 \approx 0.64$) if the smallest system sizes are excluded (see Figure). Interestingly, the sizes that need to

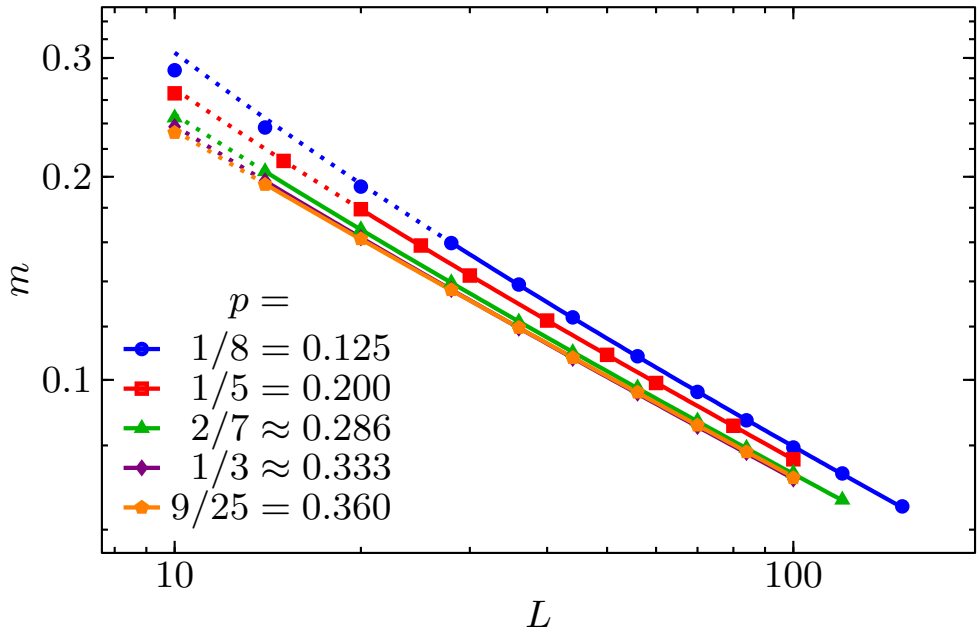

Figure 6. Double logarithmic plot of m vs. L for several dilutions p below the percolation threshold. Solid lines at fits to $m = aL^{-\beta/\nu}(1 + bL^{-\omega})$ giving $\beta/\nu = 0.480(8)$ and $\omega = 0.82(2)$. The lines are dotted in the regions not included in the fit. The statistical errors of the data are well below a symbol size.

be excluded are exactly those for which $g_{\mathrm{av}}^{\mathrm{max}}$ in Figure 5 appears to be dominated by the second subleading correction to scaling term.) The exponents resulting from the fit read $\beta/\nu = 0.480(8)$ and $\omega = 0.82(2)$. To assess the error arising from the uncertainty in T_c, we repeat the analysis for temperatures $T_c \pm \Delta T_c$ with $\Delta T_c = 0.001$. This leads to shifts of β/ν of about 0.01. Our final estimate therefore reads $\beta/\nu = 0.48(2)$.

The system-size dependence of the order parameter susceptibility χ at criticality is presented in Figure 7 for all dilutions $p < p_c$. After excluding the smallest system sizes (see Figure), the combined fit of all data to $\chi = aL^{\gamma/\nu}(1 + bL^{-\omega})$ is again of good quality ($\tilde{\chi}^2 \approx 1.5$) and yields the exponents $\gamma/\nu = 2.524(8)$ and $\omega = 0.77(1)$. After including potential errors from the uncertainty in T_c and the fit range, the final exponent estimate is $\gamma/\nu = 2.52(4)$.

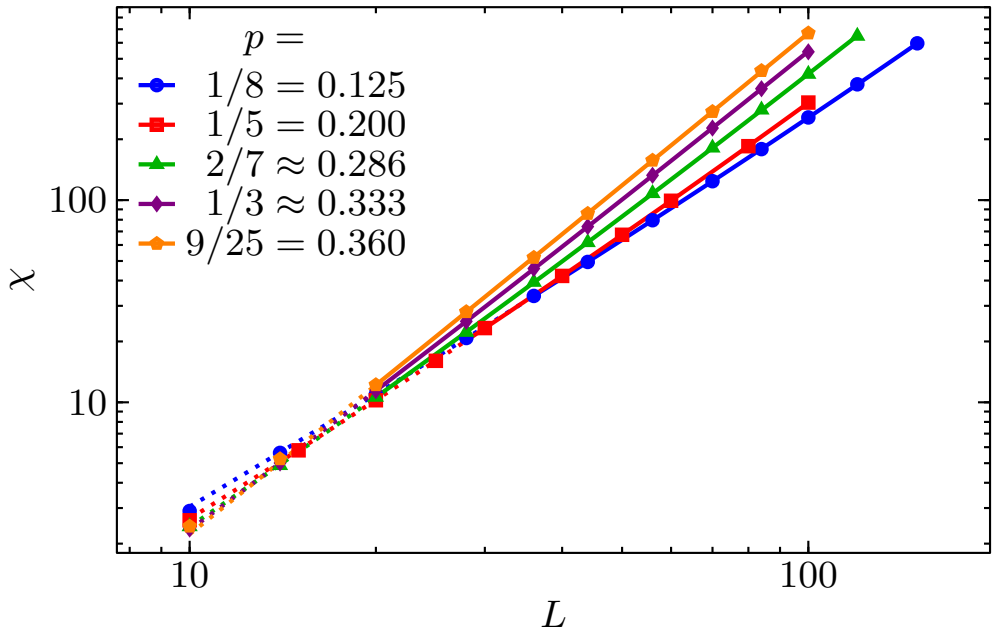

Figure 7. Double logarithmic plot of χ vs. L for several dilutions p below the percolation threshold. Solid lines at fits to $\chi = aL^{\gamma/\nu}(1 + bL^{-\omega})$ giving $\gamma/\nu = 2.524(8)$ and $\omega = 0.77(1)$. The lines are dotted in the regions not included in the fit. The statistical errors of the data are well below a symbol size.

So far, the analysis has focused on the behavior right at T_c. To find a complete set of critical exponents, we now determine the correlation length exponent ν which requires off-critical data. Figure 8 shows the temperature dependence of the Binder cumulant $g_{\rm av}$ and the reduced correlation length ξ_τ/L_τ for systems of optimal shape but different sizes at dilution $p = 1/3$. Both quantities have scale dimension zero, therefore, the curves for different system sizes are expected to cross at the critical temperature T_c. The Figure demonstrates that the crossings for both quantities shift with increasing L, reflecting significant corrections to scaling. According to Eqs. (4) and (8), the slopes $(d/dT)g_{\rm av}$ and $(d/dT)\xi_\tau/L_\tau$ at the critical temperature T_c vary as $L^{1/\nu}$ with system size. To extract the slopes, we fit straight lines (for ξ_τ/L_τ) or quadratic parabolas (for $g_{\rm av}$) to the data close to T_c. The resulting slopes are shown as a function of system size in Figures 9 and 10, respectively.

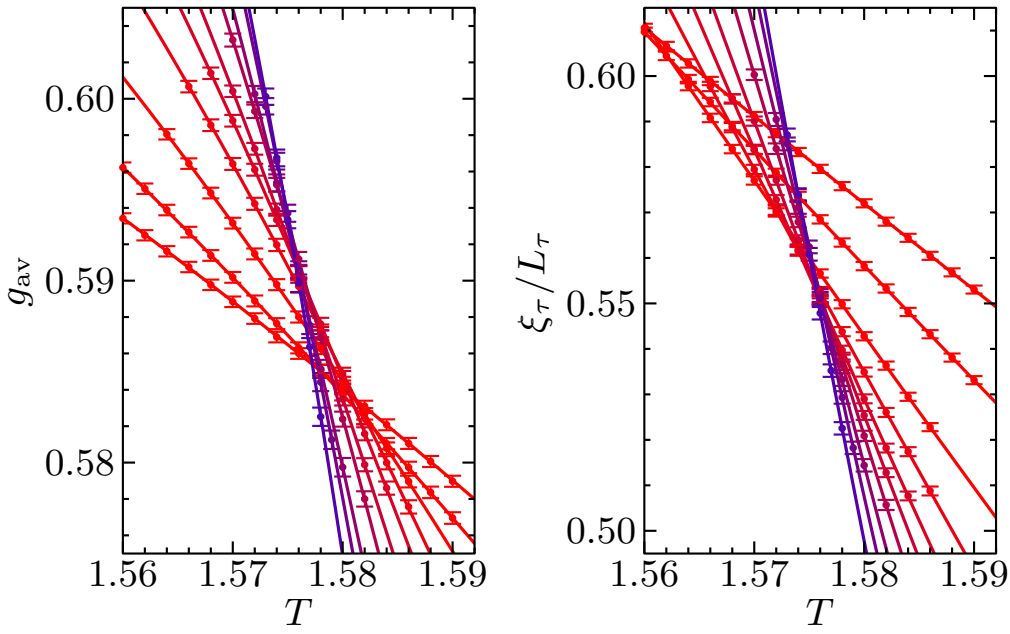

Figure 8. Average Binder cumulant $g_{\rm av}$ and reduced correlation length ξ_τ/L_τ as functions of temperature for dilution $p = 1/3$ and systems of optimal shape. System sizes range from $L = 10$ to 100 (as listed in Figure 3) with increasing slope.

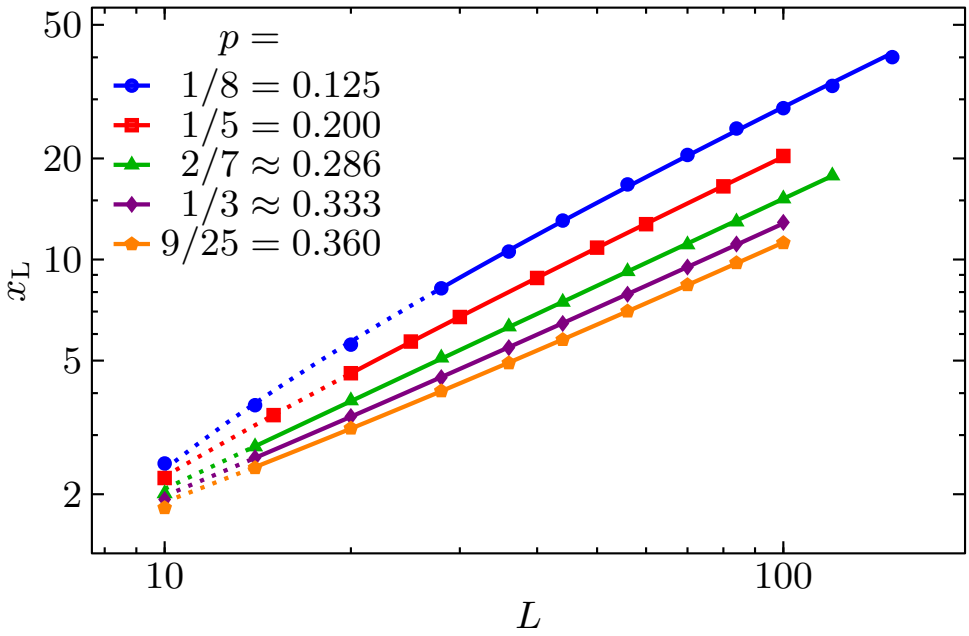

Figure 9. Slope $x_L = (d/dT)\xi_\tau/L_\tau$ at criticality vs. system size L for optimally shaped samples at different dilutions p. Solid lines at fits to $x_L = aL^{1/\nu}(1 + bL^{-\omega})$ giving $\nu = 1.165(6)$ and $\omega = 0.74(1)$. The lines are dotted in the regions not included in the fit.

The exponent ν is now obtained from fits of the slopes to the form $aL^{-1/\nu}(1+bL^{-\omega})$. In the case of the reduced correlation length ξ_τ/L_τ (Figure 9) a combined fit of all dilutions $p < p_c$ is of good quality after the smallest system sizes have been excluded ($\tilde{\chi}^2 \approx 1.2$) and yields $\nu = 1.165(6)$ as well as $\omega = 0.74(1)$. The corresponding fit of the slopes of the Binder cumulant has a somewhat poorer quality ($\tilde{\chi}^2 \approx 5.5$) and is not very stable with respect to adding and removing data points at the ends of the interval. The resulting exponents $\nu = 1.146(16)$ and $\omega = 0.97(23)$ have therefore larger errors. In addition to the slopes of the Binder cumulant g_{av} and the reduced correlation length ξ_τ/L_τ at T_c, we have also studied the slopes of ξ_s/L and $\ln m$ (not shown). After we account for the differences between all these estimates and include potential errors from the uncertainty in T_c (by repeating the analysis at temperatures $T_c \pm 0.001$) we arrive at the final estimate $\nu = 1.16(5)$. This value fulfills the inequality [58] $d\nu > 2$.

The critical exponents β/ν, γ/ν, and z are not independent of each other as they must fulfill the hyperscaling relation $2\beta/\nu + \gamma/\nu = d + z$ where $d = 2$ is the space dimensionality. Our values, $\beta/\nu = 0.48(2)$, $\gamma/\nu = 2.52(4)$, and $z = 1.52(3)$ fulfill this relation within their error bars. We also note that all our estimates for the leading irrelevant exponent ω are roughly consistent with each other, giving us confidence that our results represent true asymptotic rather than effective critical exponents.

3.3. PERCOLATION TRANSITION

We now turn to the percolation transition that occurs when the system is tuned through the percolation threshold p_c at low (classical) temperatures (see Figure 2). The critical behavior of this transition stems from the critical geometry of the percolating lattice while the dynamical fluctuations of the rotor variables are uncritical and "just go along for the ride" (the rotor model on each of the percolation clusters is locally ordered). Vojta and

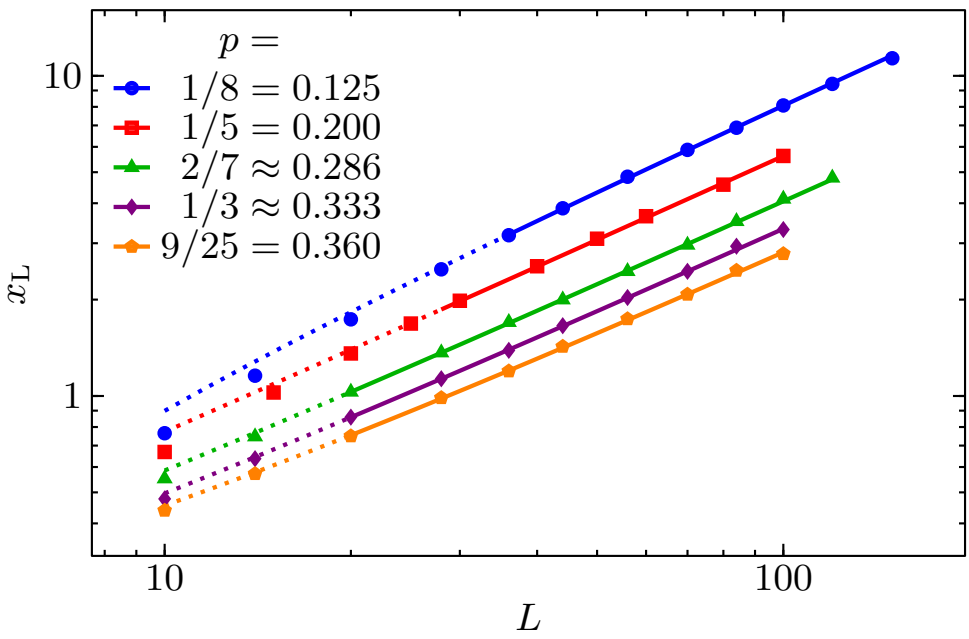

Figure 10. Slope $x_L = (d/dT)g_{\rm av}$ at criticality vs. system size L for optimally shaped samples at different dilutions p. Solid lines at fits to $x_L = aL^{1/\nu}(1 + bL^{-\omega})$ giving $\nu = 1.146(16)$ and $\omega = 0.97(23)$. The lines are dotted in the regions not included in the fit.

Schmalian [33] developed a theory of this percolation quantum phase transition. It predicts critical behavior governed by the lattice percolation exponents. For two space dimensions it yields the exact exponent values $\beta = 5/36$, $\gamma = 59/12$, $\nu = 4/3$, and $z = 91/48$.

To test these predictions, we perform simulations at dilution $p = p_c = 0.407253$ and temperature $T = 1.0$. These calculations require a particularly high numerical effort, because the large value of z leads to a rapid increase with L of the optimal system size $L_\tau^{\rm max}$ in imaginary time direction. We have thus restricted the simulations to sizes up to $L = 56$ and $L_\tau = 1792$ using between 10 000 and 50 000 disorder configurations.

The data analysis proceeds in analogy to Section 3.2. We obtain $L_\tau^{\rm max}$ from the maxima of the Binder cumulant $g_{\rm av}$ as a function of L_τ at fixed L. In Figure 11, we present a plot of $L_\tau^{\rm max}$ vs. L. The data can be fitted with high quality ($\tilde{\chi}^2 \approx 0.4$) to the predicted power law $L_\tau^{\rm max} \sim L^{91/48}$. After having found $L_\tau^{\rm max}$, we calculate the order parameter and susceptibility right at criticality for optimally shaped samples of different sizes. The

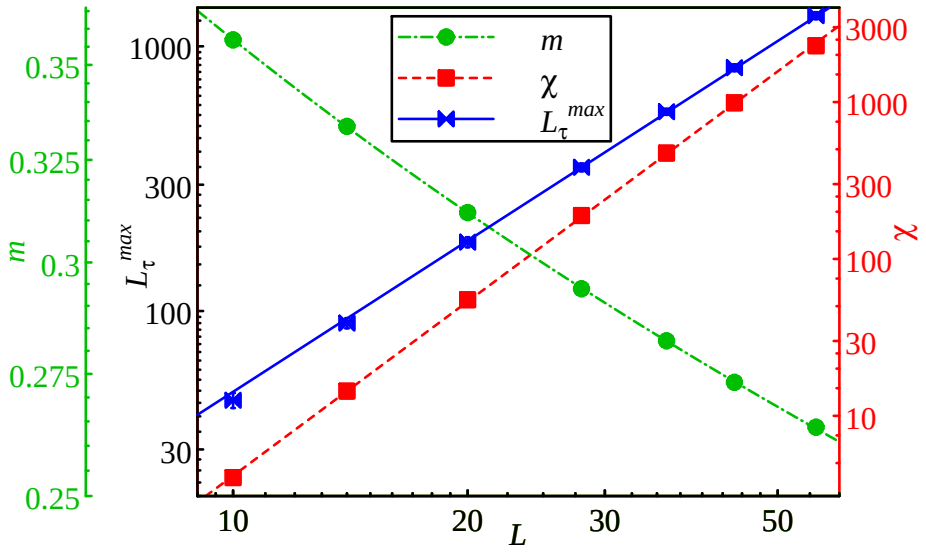

Figure 11. Double logarithmic plots of $L_\tau^{\max}$, m and χ for dilution $p = p_c = 0.407253$ and $T = 1.0$. The lines are fits to the predictions of the Reference [33], namely $L_\tau^{\max} \sim L^{91/48}$ and $\chi \sim L^{59/16}$. For the order parameter, a subleading correction is included via $m = aL^{-5/48}(1+bL^{-\omega})$. The statistical errors are of the order of the symbol size or smaller.

resulting data are also presented in Figure 11. The susceptibility data can be fitted well to the predicted power law $\chi \sim L^{59/16}$ giving $\tilde{\chi}^2 \approx 0.8$. The exponent $\beta/\nu = 5/48$ is very small, corresponding to a slow decay of the order parameter m with L. Subleading corrections are thus much more visible as indicated by the curvature of the m vs. L curve in Figure 11. We have therefore fitted the order parameter to $m = aL^{-5/48}(1+bL^{-\omega})$. This fit is again of high quality, with $\tilde{\chi}^2 \approx 0.5$.

Our simulation data thus agree nearly perfectly with the critical behavior predicted in Reference [33].

3.4. SOFT-SPIN MODEL

We also consider a soft-spin version of the classical Hamiltonian to test whether or not its critical exponents agree with those of the hard-spin model analyzed above, as is expected from universality. The soft-spin Hamiltonian reads

$$\begin{aligned} H_{\text{soft}} &= -\sum_{\langle i,j\rangle,t} \epsilon_i \epsilon_j \mathbf{S}_{i,t} \cdot \mathbf{S}_{j,t} - \sum_{i,t} \epsilon_i \mathbf{S}_{i,t} \cdot \mathbf{S}_{i,t+1} \\ &\quad -\frac{1}{2} \sum_{i,t} \epsilon_i |\mathbf{S}_{i,t}|^2 + \sum_{i,t} \epsilon_i \left(|\mathbf{S}_{i,t}|^2 \right)^2 \end{aligned} \tag{11}$$

where $\mathbf{S}_{i,t}$ now represents an unrestricted two-component vector. We perform Monte-Carlo simulations of this soft-spin model using the efficient Worm algorithm [59], studying dilutions $p = 0.286$ and 0.337. The system sizes range from $L = 8$ to 24 with L_τ fixed at $L_\tau = L^z$ using the dynamical exponent value found in Section 3.2 [3].

We now analyze the correlation length ξ_τ in imaginary time direction (equivalent to the inverse energy gap of the corresponding quantum model) on the disordered side of the phase transition. According to Eq. (10), its scaling form for samples of shape $L_\tau = L^z$ can be written as $\xi_\tau = L^z X_{\xi_\tau}(rL^{1/\nu}, 1)$. Thus, if we plot ξ_τ/L^z vs. $(T - T_c)L^{1/\nu}$, the data for different sizes and temperatures should all fall onto a single master curve. Figure 12 presents such a plot for two site dilutions p, with the critical exponents z and ν fixed at the values found in Section 3.2.

Within their statistical errors, the data scale well. Consequently, even though we have not independently determined the critical exponents of the soft-spin model (11), the Monte Carlo data are compatible with the critical behavior found earlier.

[3] We actually use $z = 1.45$ which is close to the effective dynamical exponent found for the system size range and dilution considered.

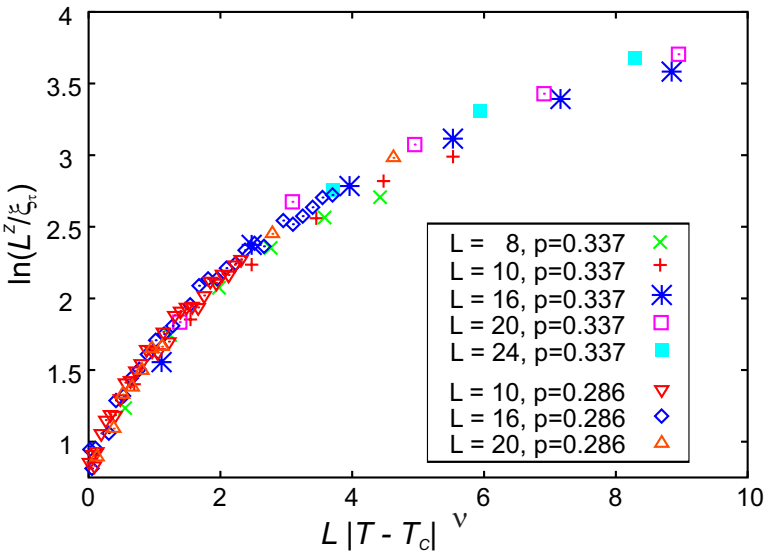

Figure 12. Scaling plot of the correlation length ξ_τ in imaginary time direction of the soft-spin model (11). Shown are data for two dilutions p, several system sizes L, and temperatures T on the disordered side of the transition. The exponents z and ν are fixed at the values found in Section 3.2. The data are averages over 100 disorder configurations. Their statistical errors are about one symbol size.

4. CONCLUSIONS

In summary, we have carried out large-scale computer simulations to determine the critical behavior of the superfluid-Mott glass quantum phase transition in two space dimensions. To this end, we have mapped a quantum rotor model with commensurate filling and off-diagonal disorder onto a (2+1)-dimensional classical XY model with columnar defects. We have then analyzed this classical system by means of Monte Carlo methods.

The corresponding clean superfluid-Mott insulator transition is in the three-dimensional XY universality class; its correlation length exponent $\nu \approx 0.6717$ violates the Harris criterion $d\nu > 2$ with $d = 2$. The clean critical behavior is therefore expected to be unstable against the columnar disorder. Accordingly, we have found that the critical behavior of the superfluid-Mott glass transition differs from that of the clean superfluid-Mott insulator transition.

Table 1. Critical exponents of the superfluid-Mott glass quantum phase transition. Upright numbers are directly given in the respective papers, italic ones were calculated using scaling relations such as $2\beta/\nu + \gamma/\nu = d + z$ and $\eta = 2 - \gamma/\nu$.

Value	This work	Reference [26]	Reference [27]	Reference [28]
ν	1.16(5)		1.09(4)	0.96(6)
z	1.52(3)	1.5(2)	1.31(7)	fixed at 1
β/ν	0.48(2)	*0.60(15)*	*1.1(2)*	
γ/ν	2.52(4)	*2.3(1)*	1.1(2)	
η	*−0.52(4)*	−0.3(1)	*0.9(2)*	

In contrast to other quantum phase transitions in disordered systems [39, 40, 41, 42, 43, 44, 45, 46, 47], the superfluid-Mott glass transition features a conventional finite-disorder critical point whose dynamical scaling is characterized by a power-law relation $\xi_\tau \sim \xi_s^z$ between the correlation lengths in the space and time directions (rather than an infinite-randomness critical point with activated dynamical scaling for which ξ_τ would grow exponentially with ξ_s). This result agrees with the general classification of phase transitions in disordered systems based on the rare region (or defect) dimensionality [48, 18]. In terms of the mapped, classical Hamiltonian (2), the rare regions in our problem are one-dimensional rods with XY order-parameter symmetry. As the lower-critical dimension of the classical XY model is $d_c^- = 2$, the rare region dimensionality fulfills $d_{RR} < d_c^-$, putting the system into the conventional class A of the classification.

For the generic transition occurring at dilutions p below the lattice percolation threshold p_c, our Monte Carlo data are described well by a universal critical behavior with dilution-independent critical exponents. The numerical estimates of the exponent values are summarized in Table 1 and compared to earlier results in the literature. Our results are in reasonable agreement with (but more accurate than) Monte Carlo simulations of a link-current model [26] that is expected to be in the same universality class as our Hamiltonian. The results in Reference [27] were obtained using a numerical implementation of the strong-disorder renormalization group. This method is expected to give approximate rather

than exact results at a conventional finite-disorder critical point such as the one under consideration here. In view of this, the agreement of ν and z can be considered satisfactory. However, the values of β/ν, γ/ν, and η (that all involve the scale dimension of the order parameter) are far away from the Monte Carlo results in this work and in Reference [26]. Our findings are also incompatible with the clean value $z = 1$ that was assumed in Reference [28].

It is interesting to consider the evolution of the dynamical exponent z with the order parameter dimensionality. The deviation of z from the clean value, which is $z = 1$ for any number of components, can be understood as a measure of the strength of the disorder effects. In the (2+1)-dimensional Heisenberg model (three order parameter components) with columnar defects, the exponent takes the value [31, 32] $z = 1.31$. The (2+1)-dimensional XY model (two components) studied in the present paper has $z = 1.52$, while the corresponding Ising model [60] (one component) features activated scaling that corresponds to $z = \infty$. The value of z thus increases monotonically with decreasing order parameter dimensionality.

In addition to the generic superfluid-Mott glass transition that occurs for dilutions $p < p_c$, we have also investigated the percolation quantum phase transition across p_c. Here, our Monte Carlo data agree very well with the predictions of the scaling theory by Vojta and Schmalian [33].

Potential routes to study the superfluid-Mott glass transition in experiment include disordered bosonic systems in ultracold atoms as well as dirty and granualar superconductors (for some superconductor-insulator transitions, there is experimental and numerical evidence for the bosonic nature of the transition). In these systems, it may be hard, though, to fulfill the condition of exact particle-hole symmetry in the presence of disorder. *Statistical* particle hole symmetry may be easier to achieve, but it is not fully resolved whether or not it would destabilize the Mott glass and turn it into a Bose glass [25, 61, 62].

Another type of experimental systems that contain Mott-glass physics are diluted anisotropic spin-1 antiferromagnets [63]. In this case, the particle-hole symmetry appears naturally as it is a consequence of the up-down symmetry of the spin Hamiltonian in the absence of an external magnetic field. Such a magnetic realization of a Mott glass (albeit in three dimensions) was recently observed in bromine-doped dichloro-tetrakis-thiourea-nickel (DTN) [9].

ACKNOWLEDGEMENTS

This work was supported in part by the NSF under Grant Nos. DMR-1205803 and DMR-1506152 as well as by funds from the UCSD Academic Senate. M.P. acknowledges support by an InProTUC scholarship of the German Academic Exchange Service. We thank Snir Gazit, Gil Refael, and Nandini Trivedi for helpful discussions.

REFERENCES

[1] B. C. Crooker, B. Hebral, E. N. Smith, Y. Takano, and J. D. Reppy. Superfluidity in a dilute bose gas. *Phys. Rev. Lett.*, 51:666–669, Aug 1983. doi: 10.1103/PhysRevLett.51.666.

[2] J. D. Reppy. ^{4}he as a dilute bose gas. *Physica B+C*, 126:335, 1984.

[3] H. S. J. van der Zant, F. C. Fritschy, W. J. Elion, L. J. Geerligs, and J. E. Mooij. Field-induced superconductor-to-insulator transitions in josephson-junction arrays. *Phys. Rev. Lett.*, 69:2971–2974, Nov 1992. doi: 10.1103/PhysRevLett.69.2971.

[4] H. S. J. van der Zant, W. J. Elion, L. J. Geerligs, and J. E. Mooij. Quantum phase transitions in two dimensions: Experiments in josephson-junction arrays. *Phys. Rev. B*, 54:10081–10093, Oct 1996. doi: 10.1103/PhysRevB.54.10081.

[5] D. B. Haviland, Y. Liu, and A. M. Goldman. Onset of superconductivity in the two-dimensional limit. *Phys. Rev. Lett.*, 62:2180–2183, May 1989. doi: 10.1103/PhysRevLett.62.2180.

[6] A. F. Hebard and M. A. Paalanen. Magnetic-field-tuned superconductor-insulator transition in two-dimensional films. *Phys. Rev. Lett.*, 65:927–930, Aug 1990. doi: 10.1103/PhysRevLett.65.927.

[7] Akira Oosawa and Hidekazu Tanaka. Random bond effect in the quantum spin system $(tl_{1-x}k_x)cucl_3$. *Phys. Rev. B*, 65:184437, May 2002. doi: 10.1103/PhysRevB.65.184437.

[8] Tao Hong, A. Zheludev, H. Manaka, and L.-P. Regnault. Evidence of a magnetic bose glass in $(CH_3)_2chnh_3Cu(Cl_{0.95}Br_{0.05})_3$ from neutron diffraction. *Phys. Rev. B*, 81: 060410, Feb 2010. doi: 10.1103/PhysRevB.81.060410.

[9] Rong Yu, Liang Yin, Neil S. Sullivan, J. S. Xia, Chao Huan, Armando Paduan-Filho, Nei F. Oliveira Jr., Stephan Haas, Alexander Steppke, Corneliu F. Miclea, Franziska Weickert, Roman Movshovich, Eun-Deok Mun, Brian L. Scott, Vivien S. Zapf, and Tommaso Roscilde. Bose glass and mott glass of quasiparticles in a doped quantum magnet. *Nature*, 489:379, 2012.

[10] M. White, M. Pasienski, D. McKay, S. Q. Zhou, D. Ceperley, and B. DeMarco. Strongly interacting bosons in a disordered optical lattice. *Phys. Rev. Lett.*, 102: 055301, Feb 2009. doi: 10.1103/PhysRevLett.102.055301.

[11] Sebastian Krinner, David Stadler, Jakob Meineke, Jean-Philippe Brantut, and Tilman Esslinger. Superfluidity with disorder in a thin film of quantum gas. *Phys. Rev. Lett.*, 110:100601, Mar 2013. doi: 10.1103/PhysRevLett.110.100601.

[12] Chiara D'Errico, Eleonora Lucioni, Luca Tanzi, Lorenzo Gori, Guillaume Roux, Ian P. McCulloch, Thierry Giamarchi, Massimo Inguscio, and Giovanni Modugno. Observation of a disordered bosonic insulator from weak to strong interactions. *Phys. Rev. Lett.*, 113:095301, Aug 2014. doi: 10.1103/PhysRevLett.113.095301.

[13] Daniel S. Fisher and Matthew P. A. Fisher. Onset of superfluidity in random media. *Phys. Rev. Lett.*, 61:1847–1850, Oct 1988. doi: 10.1103/PhysRevLett.61.1847.

[14] M. P. A. Fisher, P. B. Weichman, G. Grinstein, and D. S. Fisher. Boson localization and the superfluid-insulator transition. *Phys. Rev. B*, 40(1):546–570, Jul 1989. doi: 10.1103/PhysRevB.40.546.

[15] L. Pollet, N. V. Prokof'ev, B. V. Svistunov, and M. Troyer. Absence of a direct superfluid to mott insulator transition in disordered bose systems. *Phys. Rev. Lett.*, 103:140402, Sep 2009. doi: 10.1103/PhysRevLett.103.140402.

[16] R. B. Griffiths. Nonanalytic behavior above the critical point in a random Ising ferromagnet. *Phys. Rev. Lett.*, 23:17, 1969. doi: 10.1103/PhysRevLett.23.17.

[17] M. Thill and D. A. Huse. Equilibrium behaviour of quantum Ising spin glass. *Physica A*, 214:321, 1995. doi: 10.1016/0378-4371(94)00247-Q.

[18] T. Vojta. Rare region effects at classical, quantum, and non-equilibrium phase transitions. *J. Phys. A*, 39:R143, 2006. doi: 10.1088/0305-4470/39/22/R01.

[19] Peter B. Weichman and Ranjan Mukhopadhyay. Critical dynamics of the dirty boson problem: Revisiting the equality $z = d$. *Phys. Rev. Lett.*, 98:245701, Jun 2007. doi: 10.1103/PhysRevLett.98.245701.

[20] Anand Priyadarshee, Shailesh Chandrasekharan, Ji-Woo Lee, and Harold U. Baranger. Quantum phase transitions of hard-core bosons in background potentials. *Phys. Rev. Lett.*, 97:115703, Sep 2006. doi: 10.1103/PhysRevLett.97.115703.

[21] Hannes Meier and Mats Wallin. Quantum critical dynamics simulation of dirty boson systems. *Phys. Rev. Lett.*, 108:055701, Jan 2012. doi: 10.1103/PhysRevLett.108.055701.

[22] Ray Ng and Erik S. Sørensen. Quantum critical scaling of dirty bosons in two dimensions. *Phys. Rev. Lett.*, 114:255701, Jun 2015. doi: 10.1103/PhysRevLett.114.255701.

[23] Juan Pablo Álvarez Zúñiga, David J. Luitz, Gabriel Lemarié, and Nicolas Laflorencie. Critical properties of the superfluid¯bose-glass transition in two dimensions. *Phys. Rev. Lett.*, 114:155301, Apr 2015. doi: 10.1103/PhysRevLett.114.155301.

[24] T. Giamarchi, P. L. Doussal, and E. Orignac. Competition of random and periodic potentials in interacting fermionic systems and classical equivalents: The mott glass. *Phys. Rev. B*, 64:245119, Dec 2001. doi: 10.1103/PhysRevB.64.245119.

[25] Peter B. Weichman and Ranjan Mukhopadhyay. Particle-hole symmetry and the dirty boson problem. *Phys. Rev. B*, 77:214516, Jun 2008. doi: 10.1103/PhysRevB.77.214516.

[26] Nikolay Prokof'ev and Boris Svistunov. Superfluid-insulator transition in commensurate disordered bosonic systems: Large-scale worm algorithm simulations. *Phys. Rev. Lett.*, 92:015703, Jan 2004. doi: 10.1103/PhysRevLett.92.015703.

[27] S. Iyer, D. Pekker, and G. Refael. Mott glass to superfluid transition for random bosons in two dimensions. *Phys. Rev. B*, 85:094202, Mar 2012. doi: 10.1103/PhysRevB.85.094202.

[28] Mason Swanson, Yen Lee Loh, Mohit Randeria, and Nandini Trivedi. Dynamical conductivity across the disorder-tuned superconductor-insulator transition. *Phys. Rev. X*, 4:021007, Apr 2014. doi: 10.1103/PhysRevX.4.021007.

[29] M. Guo, R. N. Bhatt, and D. A. Huse. Quantum critical behavior of a three-dimensional Ising spin glass in a transverse magnetic field. *Phys. Rev. Lett.*, 72:4137, 1994.

[30] H. Rieger and A. P. Young. Zero-temperature quantum phase transition of a two-dimensional Ising spin glass. *Phys. Rev. Lett.*, 72:4141, 1994.

[31] R. Sknepnek, T. Vojta, and M. Vojta. Exotic vs. conventional scaling and universality in a disordered bilayer quantum Heisenberg antiferromagnet. *Phys. Rev. Lett.*, 93: 097201, 2004.

[32] T. Vojta and R. Sknepnek. Quantum phase transitions of the diluted o(3) rotor model. *Phys. Rev. B.*, 74:094415, 2006.

[33] T. Vojta and J. Schmalian. Percolation quantum phase transitions in diluted magnets. *Phys. Rev. Lett.*, 95:237206, 2005.

[34] M. Wallin, E. S. Sorensen, S. M. Girvin, and A. P. Young. Superconductor-insulator transition in two-dimensional dirty boson systems. *Phys. Rev. B*, 49:12115, 1994.

[35] Massimo Campostrini, Martin Hasenbusch, Andrea Pelissetto, and Ettore Vicari. Theoretical estimates of the critical exponents of the superfluid transition in *he*4 by lattice methods. *Phys. Rev. B*, 74(14):144506, Oct 2006. doi: 10.1103/PhysRevB.74.144506.

[36] A. B. Harris. Effect of random defects on the critical behaviour of Ising models. *J. Phys. C*, 7:1671, 1974. doi: 10.1088/0022-3719/7/9/009.

[37] M. N. Barber. Finite-size scaling. In C. Domb and J. L. Lebowitz, editors, *Phase Transitions and Critical Phenomena*, volume 8, pages 145–266. Academic, New York, 1983.

[38] J. Cardy, editor. *Finite-size scaling*. North Holland, Amsterdam, 1988.

[39] D. S. Fisher. Random transverse field Ising spin chains. *Phys. Rev. Lett.*, 69:534, 1992.

[40] D. S. Fisher. Critical behavior of random transverse-field Ising spin chains. *Phys. Rev. B*, 51:6411, 1995. doi: 10.1103/PhysRevB.51.6411.

[41] J. A. Hoyos, C. Kotabage, and T. Vojta. Effects of dissipation on a quantum critical point with disorder. *Phys. Rev. Lett.*, 99:230601, 2007. doi: 10.1103/PhysRevLett.99.230601.

[42] T. Vojta, C. Kotabage, and J. A. Hoyos. Infinite-randomness quantum critical points induced by dissipation. *Phys. Rev. B*, 79:024401, 2009. doi: 10.1103/PhysRevB.79.024401.

[43] Adrian Del Maestro, Bernd Rosenow, Markus Müller, and Subir Sachdev. Infinite randomness fixed point of the superconductor-metal quantum phase transition. *Phys. Rev. Lett.*, 101:035701, 2008.

[44] Adrian Del Maestro, Bernd Rosenow, José A. Hoyos, and Thomas Vojta. Dynamical conductivity at the dirty superconductor-metal quantum phase transition. *Phys. Rev. Lett.*, 105:145702, Oct 2010. doi: 10.1103/PhysRevLett.105.145702.

[45] Ying Xing, Hui-Min Zhang, Hai-Long Fu, Haiwen Liu, Yi Sun, Jun-Ping Peng, Fa Wang, Xi Lin, Xu-Cun Ma, Qi-Kun Xue, Jian Wang, and X. C. Xie. Quantum griffiths singularity of superconductor-metal transition in ga thin films. *Science*, 350 (6260):542–545, 2015. ISSN 0036-8075. doi: 10.1126/science.aaa7154.

[46] S. Ubaid-Kassis, T. Vojta, and A. Schroeder. Quantum Griffiths phase in the weak itinerant ferromagnetic alloy $Ni_{1-x}V_x$. *Phys. Rev. Lett.*, 104:066402, 2010.

[47] T. Vojta. Quantum Griffiths effects and smeared phase transitions in metals: theory and experiment. *J. Low Temp. Phys.*, 161:299, 2010. doi: 10.1007/s10909-010-0205-4.

[48] T. Vojta and J. Schmalian. Quantum Griffiths effects in itinerant Heisenberg magnets. *Phys. Rev. B*, 72:045438, 2005. doi: 10.1103/PhysRevB.72.045438.

[49] F. Cooper, B. Freedman, and D. Preston. Solving phi4 field theory with Monte-carlo. *Nucl. Phys. B*, 210:210, 1982.

[50] J. K. Kim. Application of finite size scaling to Monte-Carlo simulations. *Phys. Rev. Lett.*, 70:1735, 1993.

[51] S. Caracciolo, A. Gambassi, M. Gubinelli, and A. Pelissetto. Finite-size correlation length and violations of finite-size scaling. *Eur. Phys. J. B*, 20:255, 2001. doi: 10.1007/BF01352587.

[52] U. Wolff. Collective Monte-Carlo updating for spin systems. *Phys. Rev. Lett.*, 62:361, 1989.

[53] N. Metropolis, A. Rosenbluth, M. Rosenbluth, and A. Teller. Equation of state calculations by fast computing machines. *J. Chem. Phys.*, 21:1087, 1953.

[54] H. G. Ballesteros, L. A. Fernández, V. Martín-Mayor, A. Muñoz Sudupe, G. Parisi, and J. J. Ruiz-Lorenzo. Critical exponents of the three-dimensional diluted ising model. *Phys. Rev. B*, 58:2740–2747, Aug 1998. doi: 10.1103/PhysRevB.58.2740.

[55] H. G. Ballesteros, L. A. Fernandez, V. Martin-Mayor, A. Munoz Sudupe, G. Parisi, and J. J. Ruiz-Lorenzo. The four-dimensional site-diluted ising model: A finite-size scaling study. *Nucl. Phys. B*, 512:681, 1998.

[56] Qiong Zhu, Xin Wan, Rajesh Narayanan, José A. Hoyos, and Thomas Vojta. Emerging criticality in the disordered three-color ashkin-teller model. *Phys. Rev. B*, 91:224201, Jun 2015. doi: 10.1103/PhysRevB.91.224201.

[57] T. Vojta and J. A. Hoyos. Quantum phase transitions on percolating lattices. In J. Boronat, G. Astrakharchik, and F. Mazzanti, editors, *Recent Progress in Many-Body Theories*, page 235. World Scientific, Singapore, 2008.

[58] J. T. Chayes, L. Chayes, D. S. Fisher, and T. Spencer. Finite-size scaling and correlation lengths for disordered systems. *Phys. Rev. Lett.*, 57:2999, 1986.

[59] Nikolay Prokof'ev and Boris Svistunov. Worm algorithms for classical statistical models. *Phys. Rev. Lett.*, 87:160601, Sep 2001. doi: 10.1103/PhysRevLett.87.160601.

[60] O. Motrunich, S. C. Mau, D. A. Huse, and D. S. Fisher. Infinite-randomness quantum Ising critical fixed points. *Phys. Rev. B*, 61:1160, 2000. doi: 10.1103/PhysRevB.61.1160.

[61] Ehud Altman, Yariv Kafri, Anatoli Polkovnikov, and Gil Refael. Superfluid-insulator transition of disordered bosons in one dimension. *Phys. Rev. B*, 81:174528, May 2010. doi: 10.1103/PhysRevB.81.174528.

[62] Yancheng Wang, Wenan Guo, and Anders W. Sandvik. Anomalous quantum glass of bosons in a random potential in two dimensions. *Phys. Rev. Lett.*, 114:105303, Mar 2015. doi: 10.1103/PhysRevLett.114.105303.

[63] Tommaso Roscilde and Stephan Haas. Mott glass in site-diluted $s = 1$ antiferromagnets with single-ion anisotropy. *Phys. Rev. Lett.*, 99:047205, Jul 2007. doi: 10.1103/PhysRevLett.99.047205.

II. QUANTUM CRITICAL BEHAVIOR OF A THREE-DIMENSIONAL SUPERFLUID-MOTT GLASS TRANSITION

Jack Crewse[1], Cameron Lerch[1], Thomas Vojta[1]
[1] Department of Physics, Missouri University of Science and Technology
Rolla, MO 65409, USA

ABSTRACT

The superfluid to insulator quantum phase transition of a three-dimensional particle-hole symmetric system of disordered bosons is studied. To this end, a site-diluted quantum rotor Hamiltonian is mapped onto a classical (3+1)-dimensional XY model with columnar disorder and analyzed by means of large-scale Monte Carlo simulations. The superfluid-Mott insulator transition of the clean, undiluted system is in the 4D XY universality class and shows mean-field critical behavior with logarithmic corrections. The clean correlation length exponent $\nu = 1/2$ violates the Harris criterion, indicating that disorder must be a relevant perturbation. For nonzero dilutions below the lattice percolation threshold of $p_c = 0.688392$, our simulations yield conventional power-law critical behavior with dilution-independent critical exponents $z = 1.67(6)$, $\nu = 0.90(5)$, $\beta/\nu = 1.09(3)$, and $\gamma/\nu = 2.50(3)$. The critical behavior of the transition across the lattice percolation threshold is controlled by the classical percolation exponents. Our results are discussed in the context of a classification of disordered quantum phase transitions, as well as experiments in superfluids, superconductors and magnetic systems.

1. INTRODUCTION

Models of disordered and interacting bosons can be employed to describe a wide variety of physical phenomena including helium absorbed in porous media [1, 2], superconducting thin films [3, 4], Josephson junction arrays [5, 6], ultracold atoms in disordered optical lattices [7, 8, 9], and certain disordered quantum magnets [10, 11, 12, 13, 14].

It is well established [15, 16, 17] that the Mott-insulating and superfluid phases of these models are always separated by an insulating "glass" phase in which rare large regions of local superfluid order (superfluid "puddles") coexist with the insulating bulk. The glass phase thus acts as a Griffiths phase [18, 19, 20, 21] of the superfluid-Mott insulator quantum phase transition.

The nature of the glassy intermediate phase depends on the qualitative properties of the disorder. For generic disorder (realized, e.g., via a random potential for the bosons), it is the so-called Bose glass, a compressible gapless insulator. The zero-temperature phase transition between the superfluid and Bose glass ground states has recently reattracted lots of attention as new analytical [22], numerical [23, 24, 25, 26, 27], and experimental [12, 28, 13] work has challenged the scaling relation [16, 17] $z = d$ between the dynamical exponent z and the space dimensionality d as well as the value of the crossover exponent ϕ that governs the shape of the finite-temperature phase boundary.

If the system is particle-hole symmetric even in the presence of disorder, the intermediate phase between superfluid and Mott insulator is not a Bose glass but the *incompressible* gapless Mott glass [29, 30]. (This state is sometimes called random-rod glass because in a classical representation the disorder takes the form of infinitely long parallel rods.) The zero-temperature phase transition between the superfluid and Mott glass ground states has received less attention than the Bose glass transition, perhaps because in some experimental applications the condition of exact particle-hole symmetry is hard to realize and requires fine

tuning. Note, however, that the particle-hole symmetry appears naturally in magnetic realizations of disordered boson physics due to the up-down symmetry of the spin Hamiltonian in the absence of an external magnetic field.

We have recently determined the quantum critical behavior of the superfluid-Mott glass transition in two space dimensions using large-scale Monte-Carlo simulations [31], resolving earlier contradicting predictions in the literature [32, 33, 34]. However, magnetic realizations of the Mott glass state have mostly been observed in *three-dimensional* disordered magnets. To the best of our knowledge, quantitative results for the three-dimensional superfluid-Mott glass transition do not yet exist.

To investigate this transition, we analyze a site-diluted three-dimensional quantum rotor model with particle-hole symmetry. We map this quantum Hamiltonian onto a classical $(3+1)$-dimensional XY model with columnar defects. We then carry out Monte Carlo simulations for systems of up to 56 million lattice sites, averaging each data set over 2500 to 20,000 disorder configurations. For dilutions p below the lattice percolation threshold $p_c \approx 0.688392$,[35] we find the superfluid-Mott glass quantum phase transition to be characterized by universal (dilution-independent) critical exponents. The dynamical exponent takes the value $z = 1.67(6)$, and the correlation length exponent is $\nu = 0.90(5)$, fulfilling the inequality $\nu > 2/d$.[36, 37] For the order parameter exponent β and the susceptibility exponent γ, we find $\beta/\nu = 1.09(3)$ and $\gamma/\nu = 2.50(3)$, respectively. This gives an anomalous dimension of $\eta = -0.50(3)$. These exponents fulfill the hyperscaling relation $2\beta/\nu + \gamma/\nu = d + z$. As a byproduct, our simulations also yield the critical behavior of the clean (undiluted) four-dimensional XY model with high accuracy. It is characterized by mean-field exponents with logarithmic corrections (as expected at the upper critical dimension) and agrees well with the predictions of a generalized scaling theory[38].

Our paper is organized as follows. Section 2 defines the three-dimensional quantum rotor Hamiltonian and the quantum-to-classical mapping to a $(3+1)$-dimensional classical XY model. It also introduces our finite-size scaling technique (that does not require prior

knowledge of the dynamical exponent) as well as the generalized scaling theory [38] for the clean case. Monte Carlo results for the clean and disordered phase transitions are presented in Section 3. We summarize and conclude in Section 4.

2. THEORY

2.1. DILUTED ROTOR MODEL

We investigate the superfluid-Mott glass transition by means of a site-diluted quantum rotor model residing on a three-dimensional cubic lattice,

$$H = \frac{U}{2} \sum_i \epsilon_i (\hat{n}_i - \bar{n}_i)^2 - J \sum_{\langle ij \rangle} \epsilon_i \epsilon_j \cos(\hat{\phi}_i - \hat{\phi}_j), \tag{1}$$

where $\hat{n}_i$, $\bar{n}_i$, $\hat{\phi}_i$ are the number operator, offset charge, and phase operator of site i, respectively. U and J represent, respectively, the charging energy and Josephson junction coupling of the sites. We define the dilution, or impurity concentration, as the probability p, that a site is vacant. The independent quenched, random variables ϵ_i then take on the values 0 (vacancy) with probability p and 1 (occupied site) with probability $1 - p$.

The superfluid and Mott glass states can be modeled by this Hamiltonian when considering a particle-hole symmetric system with offset charges $\bar{n}_i = 0$ and commensurate (integer) fillings $\langle \hat{n}_i \rangle$. The phase diagram of this Hamiltonian has been extensively studied [17, 22]. For dominant charging energy, $U \gg J$, the ground state is a Mott insulator. For dominant Josephson junction coupling, $J \gg U$, the ground state of the system instead becomes a superfluid. Of course, this behavior is only relevant for dilutions below the lattice percolation threshold, $p_c \approx 0.688392$. Dilutions above p_c cause the lattice to break down into disconnected finite-size clusters, preventing the establishment of any long-range ordered superfluid phase. Between the superfluid and Mott insulator phases a third, intermediate phase emerges. In our particle-hole symmetric case, this is the Mott glass,

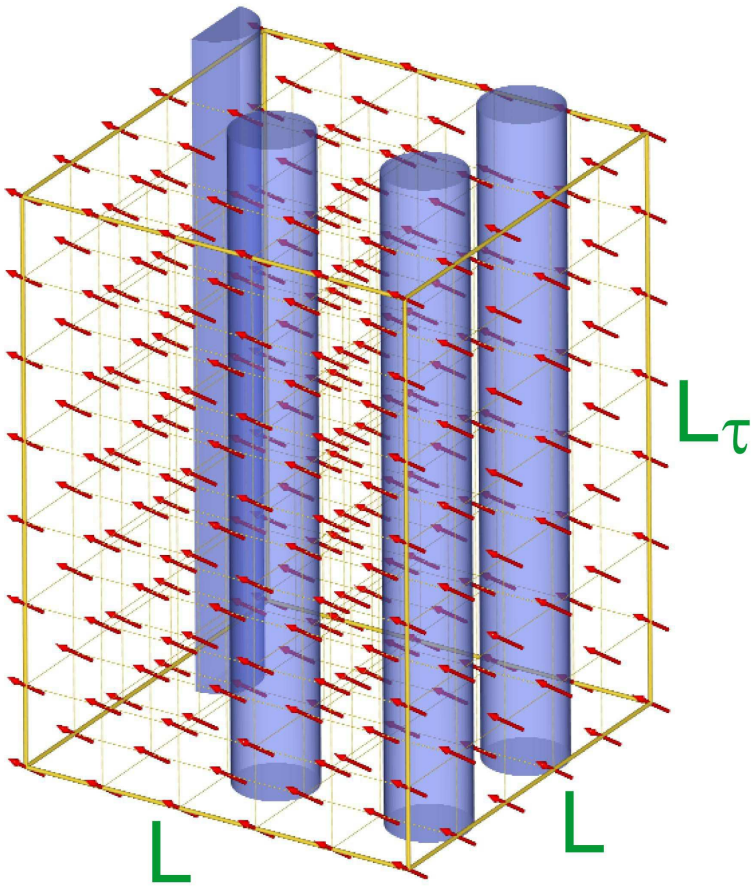

Figure 1. (2+1)-dimensional analog of the system (2). Arrows are the classical spins **S**. Columns represent the site-vacancies perfectly correlated in imaginary-time. A true sketch of the system (2) would be four-dimensional with vacant 'columns' in the imaginary-time dimension.

an incompressible, gapless insulator. The quantum phase transition from the superfluid to the Mott glass state is the focus of the present investigation. A detailed discussion of these phases and their properties can be found, e.g., in Reference [30].

2.2. QUANTUM-TO-CLASSICAL MAPPING

As we are interested only in universal properties of the transition, we simplify our study of the critical behavior by mapping the 3-dimensional quantum Hamiltonian (1) onto a classical Hamiltonian of total dimensionality $D = d + 1 = 4$.[39] The mapping gives (see

Figure 1)

$$H_{cl} = -J_s \sum_{\langle ij \rangle,\tau} \epsilon_i \epsilon_j \mathbf{S}_{i,\tau} \cdot \mathbf{S}_{j,\tau} - J_\tau \sum_{i,\tau} \epsilon_i \mathbf{S}_{i,\tau} \cdot \mathbf{S}_{i,\tau+1} \tag{2}$$

with $\mathbf{S}_{i,\tau}$ being an O(2) unit vector at space coordinate i and imaginary-time coordinate τ. Within this mapping, the "classical" temperature T of the Hamiltonian (2) does not refer to the physical temperature of the quantum system (which is zero at the quantum phase transition). Instead, the constants J_s/T and J_τ/T that appear in the classical partition function represent the coupling constants J and U of the quantum system, and the "classical" temperature is used to tune the couplings and drive the system through the transition. Additionally, the expected universality of the critical behavior allows us to ignore the exact numerical values of J_s and J_τ, so we set $J_s = J_\tau = 1$ in the following.

2.3. CLEAN (UNDILUTED) CRITICAL BEHAVIOR

In the clean limit $p = 0$ (no vacancies) the Hamiltonian (2) becomes isotropic in the space and imaginary time dimensions, thus simplifying the system to the four-dimensional classical XY model. This places the clean system at the upper-critical dimension $D_c^+ = 4$ of the XY universality class. Renormalization group calculations have shown that the transition at D_c^+ exhibits mean-field critical behavior with logarithmic corrections to scaling[38]. These calculations yield a scaling form for the free energy

$$f_L(r, H) = L^{-4} \mathcal{F}\left(rL^2 (\ln L)^{1/10}, HL^3 (\ln L)^{1/4}\right) \tag{3}$$

where $r = (T - T_c)/T_c$ and H represent the reduced temperature and field conjugate to the order parameter, respectively. Appropriate derivatives of $f_L(r, H)$ yield the dependencies of the order parameter m and its susceptibility χ on the system size L at criticality

$$m \propto L^{-1}(\ln L)^{1/4} \tag{4}$$

$$\chi \propto L^2(\ln L)^{1/2}. \tag{5}$$

This implies $\beta/\nu = 1$ and $\gamma/\nu = 2$ for the order parameter and susceptibility critical exponents, respectively. The correlation length exponent can also be extracted via the quantity $d(\ln m)/dT$, which from (3) leads to the scaling form

$$\frac{d(\ln m)}{dT} \propto L^2(\ln L)^{1/10} \tag{6}$$

implying a correlation length exponent $\nu = 1/2$. This value, however, violates the Harris criterion[36] for stability of phase transitions against weak disorder, $d\nu > 2$, where $d = 3$ is the number of dimensions with randomness, i.e., the space dimensionality. Thus the clean XY critical point is unstable against the columnar defects we introduce. As a result, we expect the diluted system to exhibit new critical behavior and exponents.

2.4. ANISOTROPIC FINITE-SIZE SCALING

Variables of scale dimension zero are especially useful in the determination of a system's critical behavior within the framework of finite-size scaling[40]. For example, central to our study is the Binder cumulant

$$g_{av} = \left[1 - \frac{\langle|\mathbf{m}|^4\rangle}{3\langle|\mathbf{m}|^2\rangle^2}\right]_{\text{dis}} \tag{7}$$

where $\mathbf{m} = (1/N)\sum_{i,\tau}\mathbf{S}_{i,\tau}$ is the order parameter (N being the total number of lattice sites of the classical Hamiltonian (2)). Additionally, $\langle ... \rangle$ denotes the Monte Carlo average, and $[...]_{\text{dis}}$ an average over disorder configurations. In the thermodynamic limit, g_{av} is expected to take the value $2/3$ in the superfluid phase and the value $1/3$ in both the Mott glass and Mott insulator phases. We also study the correlation lengths in the space and imaginary-time directions [41, 42, 43]

$$\xi_s = \left[\left(\frac{\tilde{G}(0,0) - \tilde{G}(q_{s0},0)}{q_{s0}^2\tilde{G}(q_{s0},0)}\right)^{1/2}\right]_{\text{dis}}, \tag{8}$$

$$\xi_\tau = \left[\left(\frac{\tilde{G}(0,0) - \tilde{G}(0,q_{\tau 0})}{q_{\tau 0}^2\tilde{G}(0,q_{\tau 0})}\right)^{1/2}\right]_{\text{dis}} \tag{9}$$

where $\tilde{G}(q_{s0}, q_{\tau 0})$ is the Fourier transform of the spin-spin correlation function, q_{s0} and $q_{\tau 0}$ are the minimum wavelengths in the space and imaginary-time directions, respectively.

For an isotropic system of system size L, and distance $r = (T - T_c)/T_c$ from criticality, the Binder cumulant has the finite-size scaling form $g_{av}(r, L) = X(rL^{1/\nu})$. This guarantees that at $r = 0$, the g_{av} vs r plots for different system sizes will cross at a value $g_{av}(0, L) = X(0)$, allowing us to easily locate T_c. However, the introduction of quenched disorder in the space dimensions breaks the isotropy between space and imaginary time, thus requiring us to distinguish the system sizes L in the space direction and L_τ, in the imaginary-time direction.

The finite-size scaling form of the Binder cumulant now depends on the relation between L and L_τ. For conventional power-law scaling it reads

$$g_{av}(r, L, L_\tau) = X_{g_{av}}(rL^{1/\nu}, L_\tau/L^z) \tag{10}$$

where z is the dynamical exponent, whereas for activated scaling the term L_τ/L^z in (10) is replaced by $\ln(L_\tau)/L^\psi$ with ψ the tunneling exponent. A classification scheme based on the dimensionality of locally ordered rare regions in the disordered system suggest that we

should expect power-law scaling [20, 44]. Rare region dimensionality for our XY model is $d_{RR} = 1$ (infinitely extended rare regions in the single imaginary-time direction). The lower critical dimension of the XY model is $D_c^- = 2$, thus we have $d_{RR} < D_c^-$. This puts the system (2) firmly into class A of the classification implying power-law dynamical scaling[44]. This also means that our system is not expected to display power-law Griffiths singularities. Instead observables such as the order parameter susceptibility χ show conventional behavior. Specifically, χ will remain finite in the Mott glass phase, and rare regions make exponentially small contributions.

For anisotropic systems, we must modify our approach to finite-size scaling. Due to our initial ignorance of the dynamical exponent z, we do not know the appropriate sample sizes $L \times L_\tau$ to fix the second argument of the scaling function (10) in the simulations. We can take advantage of some of the Binder cumulant's properties to find the appropriate ratios ("optimal shapes") of L_τ/L and thus our dynamical exponent z.[45, 46, 47] For a fixed spatial size L, g_{av} as a function of L_τ will exhibit a maximum at the point $(L_\tau^{\max}, g_{av}^{\max})$. At this point the ratio L_τ/L behaves like the corresponding ratio of correlation lengths ξ_τ/ξ_s and designates the "optimal shape" for that given L. For values of L_τ above or below the maximum, the system can be decomposed into independent blocks which decreases the value of g_{av}. At criticality $L_\tau^{\max}$ is proportional to L^z. Samples of optimal shape thus fix the second argument of the scaling form (10), allowing one to carry out the rest of the finite-size scaling analysis as usual.

Actually carrying out the calculations requires an iterative approach. An educated guess is made for an initial value of the dynamical exponent z (e.g. the value calculated for the (2+1)d case)[31]. The (approximate) crossings of the g_{av} vs r curves for samples of the resulting shapes give an estimate for T_c. The temperature is then fixed at this estimate of T_c and g_{av} as a function of L_τ is analyzed. The points of maximum value $g_{av}^{\max}$ at $L_\tau^{\max}$ can then be calculated and give improved estimates for the optimal shapes and thus an improved estimate on z. For $T > T_c$ the $g_{av}^{\max}$ values will tend towards their disordered

(decreasing) values with increasing system size, for values $T < T_c$ they tend towards their ordered (increasing) values for increasing system size. Thus, for a given estimate for T_c, the trends of $g_{av}^{\max}$ with system size allow us to determine how to adjust our T_c estimate for the next iteration. Using this procedure the values of T_c and z converge quickly, requiring only about 3-5 iterations.

Once we have determined the value of z for the system, the usual finite-size analysis can be carried out with the scaling forms

$$m = L^{-\beta/\nu} X_m(rL^{1/\nu}, L_\tau/L^z) \tag{11}$$

$$\chi = L^{\gamma/\nu} X_\chi(rL^{1/\nu}, L_\tau/L^z) \tag{12}$$

where β and γ are the order parameter and susceptibility critical exponents and the functions X_m and X_χ are scaling functions. Analogously, the reduced correlation lengths ξ_s/L and ξ_τ/L_τ take the scaling forms

$$\xi_s/L = X_{\xi_s}(rL^{1/\nu}, L_\tau/L^z), \tag{13}$$

$$\xi_\tau/L_\tau = X_{\xi_\tau}(rL^{1/\nu}, L_\tau/L^z). \tag{14}$$

We can also establish information about the compressibility κ and superfluid density ρ_s of the system. Under the quantum-to-classical mapping, the compressibility $\kappa = \partial\langle n\rangle/\partial\mu$ and superfluid density ρ_s map, respectively, onto the spinwave stiffnesses in imaginary-time and space dimensions as

$$\rho_{cl,\tau} = L_\tau^2(\partial^2 f/\partial\theta^2)_{\theta=0} \tag{15}$$

$$\rho_{cl,s} = L^2(\partial^2 f/\partial\theta^2)_{\theta=0} \tag{16}$$

where f is the free energy density for twisted boundary conditions (i.e. the XY spins of the classical model $\mathbf{S}_{i,\tau}$ at $\tau = 0$ ($i = 0$) are at an angle θ with respect to the spins at the boundary $\tau = L_\tau$ ($i = L$)). Explicitly, for the XY model considered here (15) takes the form[48]

$$\rho_{cl,\tau} = \frac{1}{N}\sum_{i,\tau}\langle \mathbf{S}_{i,\tau}\cdot\mathbf{S}_{i,\tau+1}\rangle - \frac{\beta}{N}\left\langle\left\{\sum_{i,\tau}\hat{k}\cdot(\mathbf{S}_{i,\tau}\times\mathbf{S}_{i,\tau+1})\right\}^2\right\rangle \tag{17}$$

where $\hat{k}$ represents the unit vector perpendicular to the XY plane of the spins. The space stiffness $\rho_{cl,s}$ takes an analogous form. These quantities are expected to exhibit power-law scaling behavior according to the scaling forms

$$\rho_{cl,s} = L^{-y_s}X_{\rho_s}(rL^{1/\nu}, L_\tau/L^z) \tag{18}$$

$$\rho_{cl,\tau} = L^{-y_\tau}X_{\rho_\tau}(rL^{1/\nu}, L_\tau/L^z) \tag{19}$$

where X_{ρ_s} and X_{ρ_τ} are scaling functions, while $y_s = d + z - 2$ and $y_\tau = d - z$ are the scale dimensions of the spinwave stiffnesses in space and imaginary-time, respectively [30]. Both stiffnesses are expected to be nonzero in the superfluid phase. In both the Mott insulator and the Mott glass phases, they are expected to vanish. (Note that the Mott glass is an *incompressible* insulator.)

3. MONTE CARLO SIMULATIONS

3.1. OVERVIEW

Our investigation consists of Monte Carlo simulations of the classical XY model (2) with both the standard single-spin-flip Metropolis[49] algorithm, as well as the cluster-update Wolff[50] algorithm. Both algorithms are used throughout the simulations and one "full sweep" is defined as a Metropolis sweep over the entire lattice and a Wolff sweep. A Wolff sweep in our simulations flips a number of clusters such that the total number of

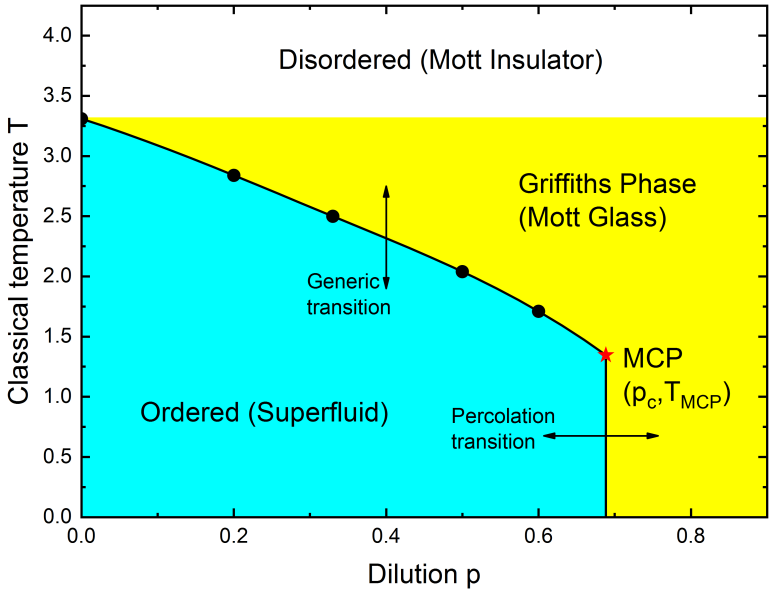

Figure 2. Phase diagram of the classical (3+1)-dimensional XY model with respect to classical temperature T and dilution p. The multi-critical point (MCP) is estimated as the intersection of a spline interpolation of the numerical critical temperatures (dots) and the percolation transition at p_c. The errors of the calculated T_c are smaller than the symbol size.

spins flipped in the clusters is equal to the number of spins in the system. While the Wolff algorithm alone is sufficient to equilibrate clean systems, highly dilute systems can exhibit small disconnected clusters that the Metropolis algorithm can more effectively equilibrate.

We simulate a range of dilutions $p = 0, 1/3, 1/2, 3/5$ and $p = p_c \approx 0.688392$ with system sizes up to $L = 80$ in the space dimensions and $L_\tau = 320$ in the imaginary-time dimension. All data need to be averaged over a large number of independent dilution configurations. This increases the computational effort needed for meaningful results. Best performance can be achieved with a rather small number of measurements sweeps, N_m, but a large number of disorder realizations (samples), N_s.[51, 52] To this end, we have chosen $N_m = 500$ and $N_s = 4000 - 20000$ (depending on system size). To eliminate biases due to the short measurements, we use improved estimators[53]. To ensure complete equilibration of the system we have chosen $N_{eq} = 100$ equilibration sweeps to be carried out before each

measurement. We have confirmed that 100 sweeps are sufficient by comparing the results of the simulations with hot starts (spins initially randomly oriented) and cold starts (spins initially aligned) and verifying that they agree within their error bars.

The phase diagram resulting from the simulations is presented in Figure 2. As expected, the transition temperatures $T_c(p)$ decrease with increasing dilution from the clean value $T_c(0)$. The generic transition ends at the multi-critical point, which we have estimated from the intersection of a spline fit of the calculated $T_c(p)$ and the lattice percolation threshold $p_c = 0.688392$.

3.2. CLEAN CRITICAL BEHAVIOR

First, we analyze the phase transition of the clean, undiluted system ($p = 0$). Since the clean system is isotropic, we choose samples with $L = L_\tau$ between 10 and 80. The critical temperature is determined from the crossings of the g_{av} vs T curves for different L and the corresponding crossings of the ξ/L vs T curves. Extrapolating to $L \to \infty$ yields a critical temperature $T_c(0) = 3.31445(3)$.

Figure 3 shows both order parameter and susceptibility as functions of system size right at the critical temperature. Fits of the order parameter data to the scaling form $m = aL^{-\beta/\nu}(\ln(L/L_0))^{\omega}$ are of good quality (reduced chi-squared $\tilde{\chi}^2 \approx 0.3$) and give critical exponents $\beta/\nu = 1.008(12)$ and $\omega = 0.25(8)$. Considering the same fits for various temperatures within the error bars of our critical temperature estimate, leads to variation in β/ν of around 0.02. Our final estimate for the order parameter exponent is $\beta/\nu = 1.00(2)$.

Fits of the susceptibility to the scaling form $\chi = aL^{\gamma/\nu}(\ln(L/L_0))^{\omega'}$ are less stable. We fit the data to the scaling form with the irrelevant exponent fixed at it's predicted value $\omega' = 1/2$ from equation (5). This yields a critical exponent $\gamma/\nu = 2.00(2)$ with reduced chi-squared $\tilde{\chi}^2 \approx 0.65$. Susceptibility fits are more sensitive to errors in critical temperature, having a variation in γ/ν of about 0.04 for temperatures within our error bar estimates. Our final estimate for the susceptibility critical exponent is $\gamma/\nu = 2.00(6)$.

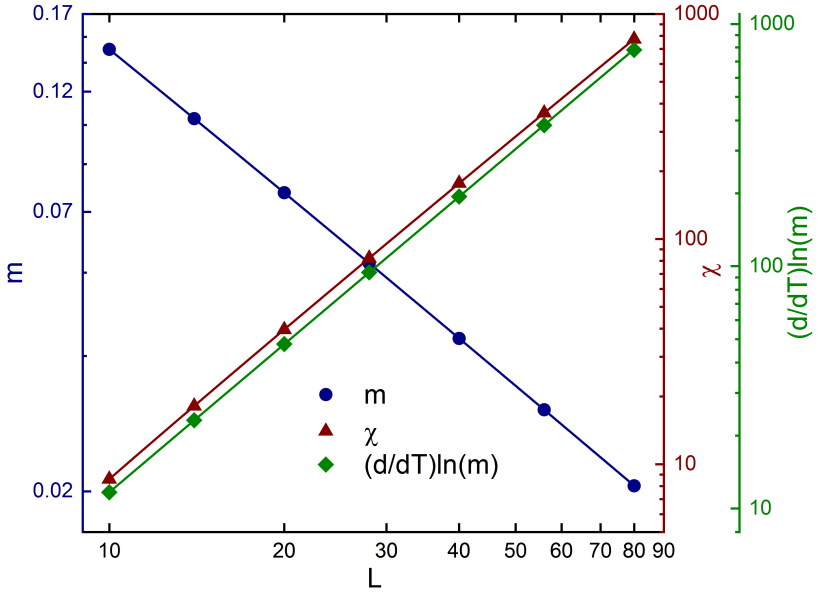

Figure 3. Order parameter m and susceptibility χ vs system size L for the clean case ($p = 0$). Solid lines are fits to $m = aL^{-\beta/\nu}(\ln(L/L_0))^{\omega}$ and $\chi = aL^{\gamma/\nu}(\ln(L/L_0))^{\omega}$ that yield $\beta/\nu = 1.008(12)$ and $\gamma/\nu = 2.00(1)$, respectively. Statistical errors are of the order of the symbol size.

Lastly, we find the correlation length critical exponent via slopes of the Binder cumulant g_{av}, reduced correlation length ξ/L and logarithm of the order parameter $\ln(m)$, with respect to temperature. Equation (6) predicts a value of $\nu = 1/2$ for the correlation length critical exponent for $(d/dT)\ln(m)$ and universality implies the same scaling form holds for g_{av} & ξ/L. Fitting the data for $(d/dT)\ln(m)$ to the scaling form $aL^{1/\nu}\ln(L/L_0)^{\bar{\omega}}$ with irrelevant exponent fixed at the theoretical value $\bar{\omega} = 1/10$ yields the critical exponent $\nu = 0.50(2)$ for an acceptable fit ($\tilde{\chi}^2 \approx 4$). Similar analysis for $(d/dT)g_{av}$ and $(d/dT)(\xi/L)$ yields $\nu = 0.50(2)$ and $\nu = 0.49(4)$, respectively. Our final estimate for the correlation length critical exponent is $\nu = 0.50(6)$.

Finally, we note that pure power-law fits to the data show significantly larger $\tilde{\chi}^2$ values. This further justifies the logarithmic corrections in the scaling forms (4) - (6). In summary, all of our Monte Carlo results for the clean case are in good agreement with the scaling theory of Reference [38].

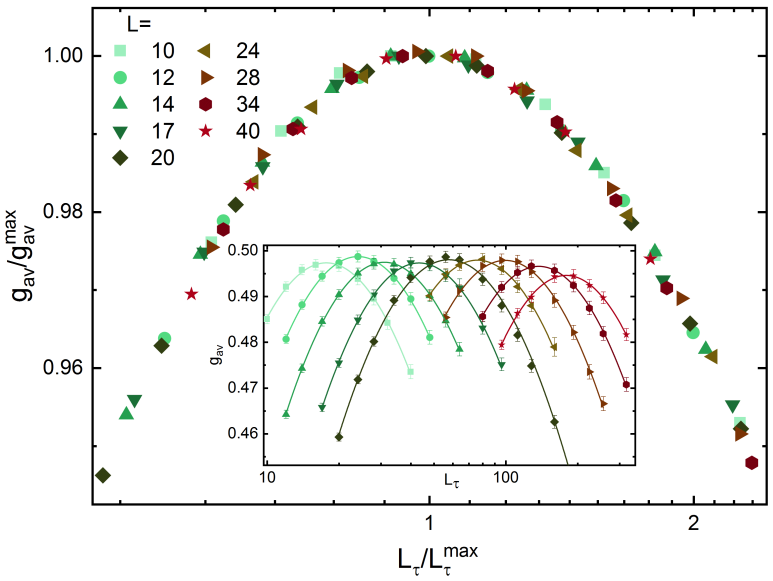

Figure 4. Binder cumulant g_{av} as a function of L_τ for several L and dilution $p = 0.5$ at the critical temperature $T_c = 2.037$. Plotting $g_{av}/g_{av}^{\max}$ in the main panel eliminates the leading additive correction to scaling from the analysis.

3.3. DISORDERED CASE: GENERIC TRANSITION

The finite-size scaling analysis of the generic transition, $(0 < p < p_c)$ is carried out as described in Section 2.4. Determining a full set of critical exponents requires first finding the optimal shapes and calculating the dynamical exponent z in order to fix the second argument of our scaling forms (10) - (19). This is achieved using the iterative procedure also outlined in Section 2.4.

Figures 4 and 5 show an example of this analysis. Specifically, Figure 4 presents the Binder cumulant g_{av} for the dilution $p = 0.5$ as a function of L_τ for system sizes $L = 10 - 40$ at the estimated critical temperature. The raw data are shown in the inset; as expected, $g_{av}^{\max}$ at the critical point is (roughly) independent of L and exhibits a maximum at $L_\tau^{\max}$ for each system size. Remaining variation of $g_{av}^{\max}$ is due to the uncertainty in T_c for the large system sizes and corrections to scaling for small system sizes (both of these will be discussed further below). The main panel is a scaling plot demonstrating that the Binder

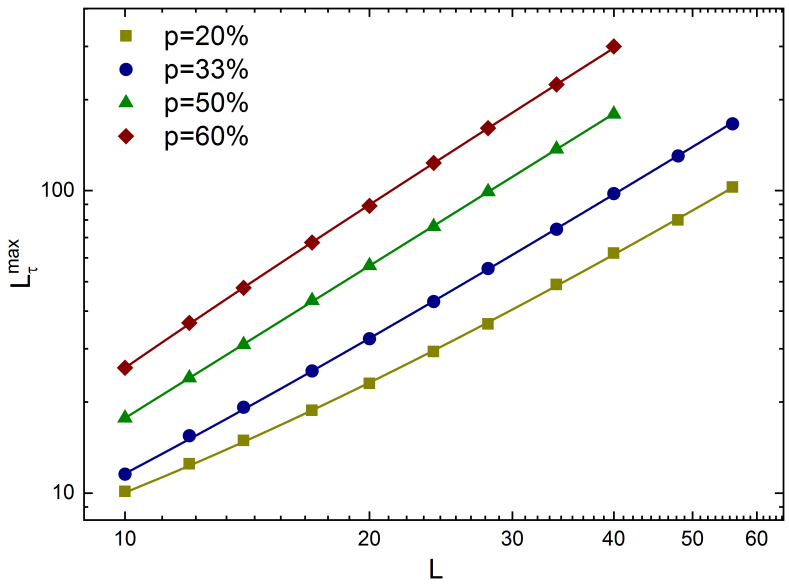

Figure 5. Log-log plots of $L_\tau^{\max}$ vs L. Solid lines are fits to $L_\tau^{\max} = aL^z(1 + bL^{-\omega})$ yielding $z = 1.672(9)$ and $\omega = 1.18(5)$. Statistical errors are of the order of the symbol size.

cumulant fulfills the scaling form (10) to a high degree of accuracy and variations due to uncertainty in T_c and corrections to scaling simply shift the $g_{\rm av}$ vs. L_τ curves up or down. Corresponding scaling plots were also constructed with analogous results for the remaining dilutions $p = 1/5, 1/3$, and $3/5$.

Determining z requires analyzing the position $L_\tau^{\max}$ of these maxima which we have found via quadratic fits of g_{av} vs $\ln L_\tau$. Plots of $L_\tau^{\max}$ vs L are shown in Figure 5. As can be seen, the data show significant corrections to scaling (deviations from straight lines), especially for smaller dilutions. Neglecting them by fitting the data via pure power laws would yield only effective, scale-dependent exponents. Therefore, we include the leading-order correction to scaling via the ansatz $L_\tau^{\max} = aL^z(1 + bL^{-\omega})$ with dilution-independent critical exponents z and ω but dilution-dependent prefactors a and b. This yields true asymptotic, scale-independent critical exponents. Combined fits of all four dilution data sets gives exponents $z = 1.672(9)$ and $\omega = 1.18(5)$ with an acceptable reduced chi-squared $\tilde{\chi}^2 \approx 2.69$. If we consider the robustness of the combined fits against removal of upper and

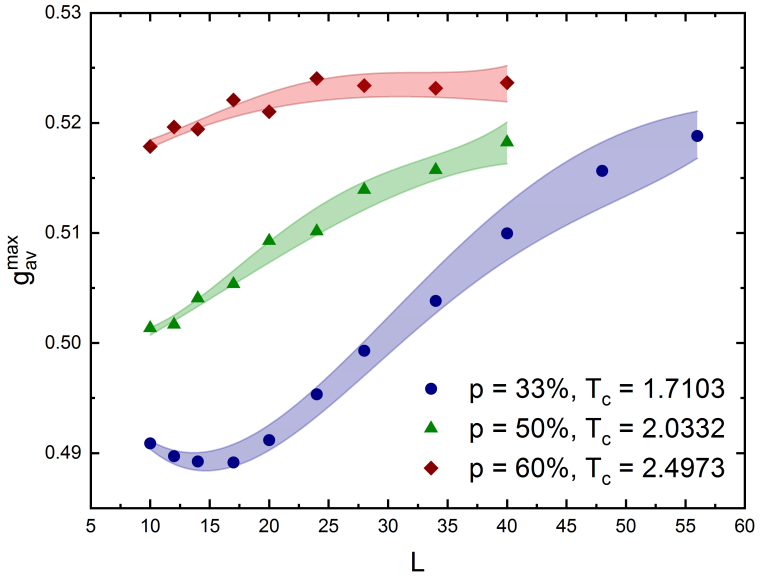

Figure 6. $g_{av}^{\max}$ vs L for the improved estimates for T_c. Shaded regions represent the the range values for which the criterion is also satisfied. From this we estimate an error on T_c of no more than 0.0003. Statistical errors are of the order of the symbol size or smaller. The remaining variation of $g_{av}^{\max}$ likely stems from the discreteness of L_τ.

lower data points from each set as well as removal of entire dilution sets, we come to an estimate for the dynamical critical exponent of $z = 1.67(4)$. We also note that the leading corrections to scaling vanish close to $p = 1/2$ where the prefactor b changes sign and is effectively zero for our fits of $p = 1/2$. The vanishing of these corrections is also reinforced by the comparison of pure power-law fits and fits to scaling forms including subleading corrections. For the $p = 1/2$, power-law fits yield $z = 1.671(3)$, where the fits including the subleading corrections yields $z = 1.66(1)$. The global, dilution independent value for the dynamical exponent is also bracketed nicely by the values obtained upon pure power-law fits of the largest system sizes for the dilutions $p = 1/3$ and $p = 3/5$, which yield $z = 1.592(6)$ and $z = 1.767(7)$, respectively. To estimate the error of z stemming from the uncertainty in T_c, we have repeated the analysis for appropriately chosen temperatures slightly above

and below our estimate for T_c. Variation of the dynamical exponent within this range of temperatures is about 0.03. After considering this uncertainty in T_c, statistical error and the robustness of our fits, we come to our final estimate of the dynamical exponent $z = 1.67(6)$.

To complete our set of critical exponents, we now analyze the Monte Carlo runs for systems of optimal shape and in the vicinity of their critical temperature $T_c(p)$. With L_τ/L^z fixed by the optimal shapes found above, the scaling forms (11) and (12) are then used to extract β/ν and γ/ν from the L dependence of the order parameter m and susceptibility χ at $T_c(p)$. We again fit the data with leading corrections to scaling included via the ansatz $m = aL^{-\beta/\nu}(1 + bL^{-\omega})$ and $\chi = aL^{\gamma/\nu}(1 + bL^{-\omega})$ with universal exponents but dilution-dependent prefactors. However, the combined fits of these data proved to be very sensitive to small changes in $T_c(p)$ (much more so than the fit determining z). This indicates that our critical temperature estimates (originally found from the crossings of the curves of dimensionless quantities versus temperature) are not the true critical temperatures. Thus, to improve our critical temperature estimates, we impart the criterion that at criticality the value of $g_{av}^{\max}$ should approach a dilution-independent value as $L \longrightarrow \infty$. We can adjust our estimates for $T_c(p)$ until this criterion is satisfied, with $g_{av}^{\max}$ approaching dilution and system size independent values, as is shown in Figure 6.[31] This adjustment of the critical temperatures yields our final estimates: $T_c(1/5) = 2.837$, $T_c(1/3) = 2.4973$, $T_c(1/2) = 2.0332$, $T_c(3/5) = 1.7103$. The data can also be seen to satisfy this criterion for a small range of temperatures, thus we assign an error to our estimated critical temperatures of no more than ± 0.0003. The data in Figure 6 clearly demonstrates that the systems with dilutions $p = 1/3$ and $p = 1/2$ show pronounced corrections to scaling. They are still crossing over from the clean critical fixed point to the asymptotic regime even at the largest L. Moreover, $g_{av}^{\max}$ for small system sizes exhibits non-monotonous behavior, from which we conclude that there are at least two corrections to scaling contributing for the smallest dilutions and system sizes.

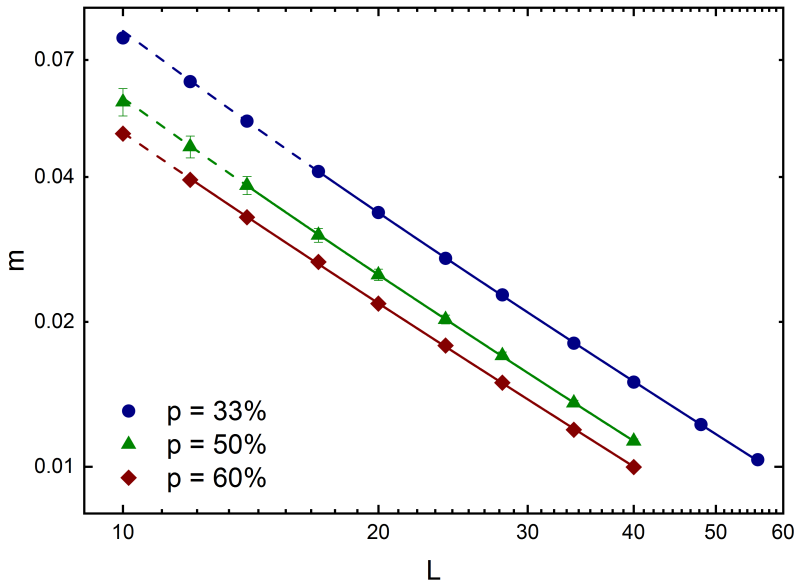

Figure 7. Log-log plot of m vs L at the critical temperature. Solid lines are fits to $m = aL^{-\beta/\nu}(1 + bL^{-\omega})$ that yield $\beta/\nu = 1.087(11)$ and $\omega = 1.22(7)$. Lines are dashed in regions that are not included in the fit. Statistical errors are of the order of the symbol size unless shown explicitly in the plot.

With the improved estimates for T_c, we proceed to fit the three largest dilutions ($p = 1/5, 1/3, 3/5$) with the above scaling ansatz to find β/ν and γ/ν. Order parameter m versus system size L for the three dilutions is shown in Figure 7. We perform a combined fit with $m = aL^{-\beta/\nu}(1 + bL^{-\omega})$. Leaving out the system sizes most affected by the second sub-leading corrections to scaling mentioned above, we get good fits ($\tilde{\chi}^2 \approx 0.43$) that result in a critical exponent $\beta/\nu = 1.087(11)$ and correction exponent $\omega = 1.22(7)$. Fits to the same data for slightly adjusted temperatures within the estimated error ($T_c \pm 0.0003$) lead to variation in the critical exponent of about 0.02. Our final estimate for the order parameter critical exponent then reads $\beta/\nu = 1.09(3)$.

Figure 8 shows the order parameter susceptibility χ as a function of system size L at criticality. Fitting to the ansatz with leading-order corrections $\chi = aL^{\gamma/\nu}(1 + bL^{-\omega})$, and again dropping the system sizes most affected by sub-leading order corrections, we arrive

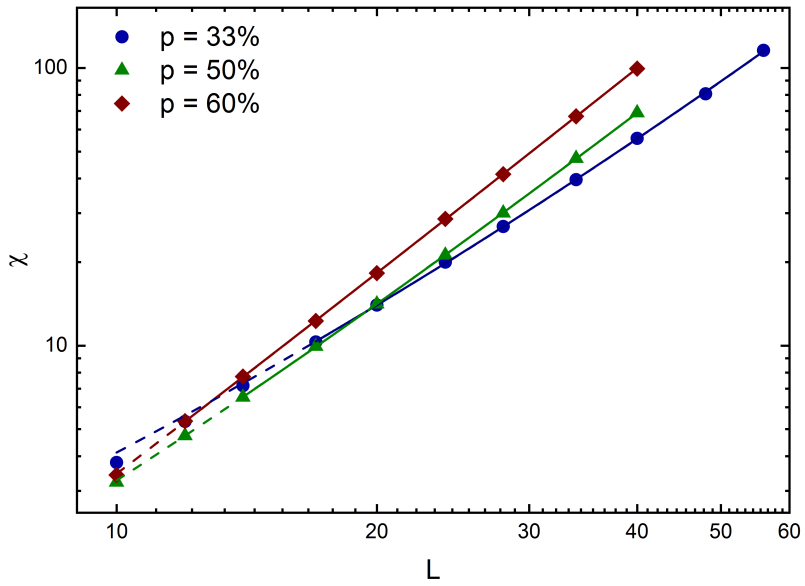

Figure 8. Log-log plot of χ vs L at the critical temperature. Solid lines are fits to $\chi = aL^{\gamma/\nu}(1 + bL^{-\omega})$ that yield $\gamma/\nu = 2.495(7)$ and $\omega = 1.16(2)$. Lines are dashed in regions that are not included in the fit. Statistical errors are of the order of the symbol size.

at a good fit ($\tilde{\chi}^2 \approx 1.3$) that yields the critical exponent $\gamma/\nu = 2.495(7)$ and correction exponent $\omega = 1.16(2)$. After considering the uncertainties in T_c and fit range, as we did for β/ν, we come to the final estimate for the susceptibility exponent $\gamma/\nu = 2.50(3)$.

We now move to determining the correlation length critical exponent. This can be determined by considering the slopes of g_{av} and ξ_τ/L_τ as functions of temperature. Figure 9 shows off-critical data g_{av} and ξ_τ/L_τ for dilution $p = 1/3$, as functions of temperature. Since both quantities have scale dimension zero, they should cross directly at the critical temperature. However, it is clear in the data that a shift occurs in these crossings for increasing system size L, thus we still expect significant corrections to scaling. Equations (10) and (13) show that the correlation exponent can be extracted from finite-size scaling of $(d/dT)g_{av}$ and $(d/dT)\xi_\tau/L_\tau$, which each vary as $L^{1/\nu}$ with system size. Extracting the slopes of each of these functions is done by linear fits to the data in the vicinity of the critical temperature. Figure 10 shows the slopes of the Binder cumulant g_{av} as a function of system size. Again, to account for the corrections to scaling, we fit this data with the ansatz scaling

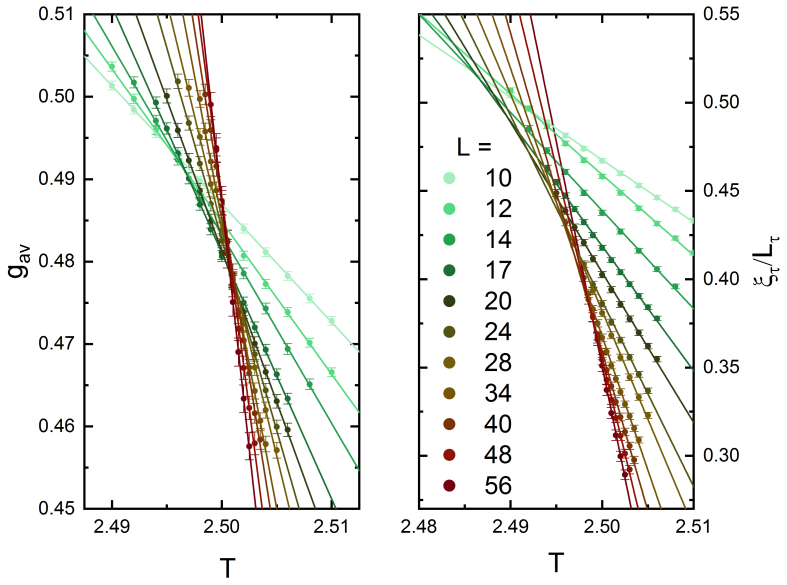

Figure 9. Binder cumulant g_{av} and reduced correlation function ξ_τ/L_τ for systems of optimal shape and dilution $p = 1/3$. Plotted are system sizes $L = 10 - 56$ with increasing slope.

form $aL^{1/\nu}(1 + bL^{-\omega})$. Combined fits to $(d/dT)g_{av}$ lead to $\nu = 0.90(2)$ and $\omega = 1.17(8)$ with a reduced chi-squared $\tilde{\chi} \approx 2.2$. Similar fits of the reduced correlation length ξ_τ/L_τ are of good quality ($\tilde{\chi}^2 \approx 1.15$) when the smallest system sizes are left out giving a correlation exponent of $\nu = 0.894(4)$ and correction exponent $\omega = 1.16(10)$. Similar analysis carried out on $(d/dT)\xi_s/L$ yields nearly identical results. Considering the robustness of the fits against removal of upper and lower data points, we are led to a somewhat larger error, leading to a final estimate that reads $\nu = 0.90(5)$.

The critical exponents must satisfy the hyperscaling relationship $2\beta/\nu+\gamma/\nu = d+z$, where $d = 3$ is the spatial dimension. Our values $\beta/\nu = 1.09(3)$, $\gamma/\nu = 2.50(3)$, and $z = 1.67(6)$ fulfill this relationship nicely within the error bars. We can also assign a value to the anomalous dimension η, defined via the decay of the critical correlation function in space, $G(\mathbf{x}) \sim |\mathbf{x}|^{-(d+z-2+\eta)}$. It measures the deviation of G from a hypothetical Gaussian

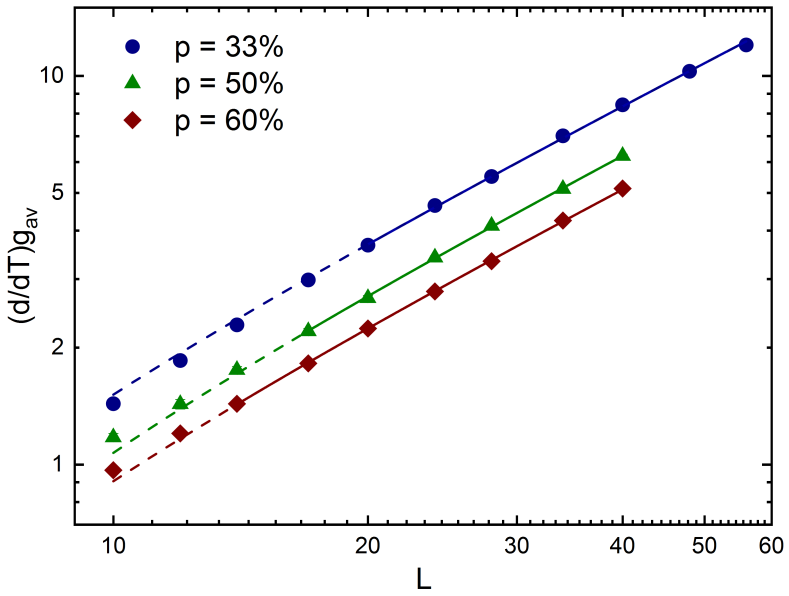

Figure 10. Log-log plot of $(d/dT)g_{av}$ vs L. Solid lines are fits to $g_{av} = aL^{1/\nu}(1 + bL^{-\omega})$ that yield $\nu = 0.90(2)$ and $\omega = 1.17(8)$. Lines are dashed in regions that are not included in the fit. Statistical errors are of order of the symbol size.

theory [4]. This anomalous dimension η can be calculated via the relationship $\eta = 2 - \gamma/\nu$, giving the result $\eta = -0.50(3)$. Additionally, the inequality $d\nu > 2$ is now fulfilled for our correlation exponent $\nu = 0.90(5)$. Because the critical exponents satisfy the hyperscaling relationship and the values of the exponent ω that governs the corrections to scaling are consistent across the range of fits, we can conclude that the critical exponent estimates that we have obtained are the true asymptotic critical exponents.

3.4. SUPERFLUID DENSITY

A final result from our simulations is the critical behavior of the compressibility κ and superfluid density ρ_s. This is determined by considering the behavior of the spinwave stiffness of the classical Hamiltonian (2) in space and imaginary-time dimensions for opti-

[4] A purely Gaussian theory would predict a correlation function that decays as $G \sim |\mathbf{x}|^{-(d+z)+2}$ with z the dynamical exponent of the system. The anomalous dimension is the deviation of the exponent from this power-law behavior.

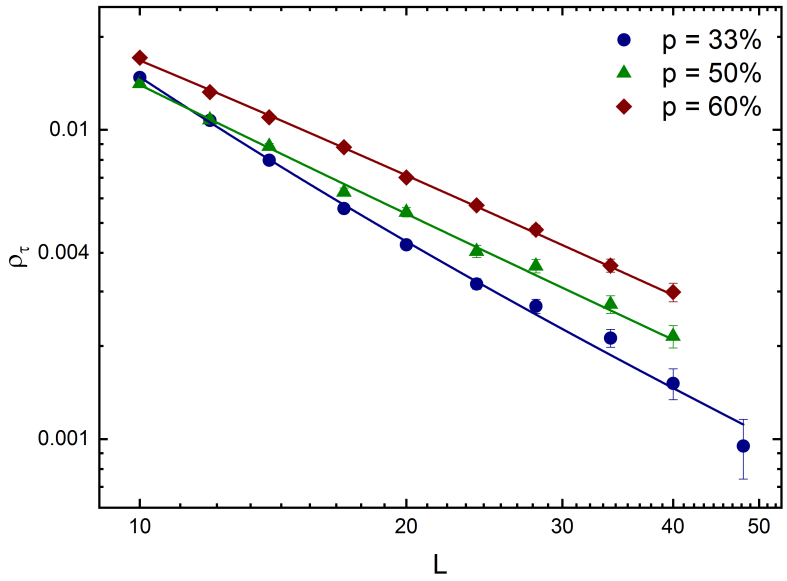

Figure 11. Log-log plot of ρ_τ vs L. Solid lines are fits to $\rho_\tau = aL^{-y_\tau}(1 + bL^{-\omega})$ that yield $y_\tau = 1.32(2)$ and $\omega = 1.19(6)$.

mally shaped systems right at the critical temperatures for the dilutions $p = 1/3, 1/2, 3/5$. Both observables, $\rho_{cl,s}$ and $\rho_{cl,\tau}$, are very close to zero and thus, noisy. A plot of $\rho_{cl,\tau}$ vs L is shown in Figure 11. Corrections to scaling are clearly relevant still, so we perform fits with first-order corrections $\rho_{cl,\tau} = aL^{-y_\tau}(1 + bL^{-\omega})$. Good fits can be obtained over the entire data set despite the noisy large system sizes ($\tilde{\chi}^2 \approx 1.03$), yielding $y_\tau = 1.32(1)$ and $\omega = 1.19(6)$. The fit is surprisingly stable against removal of data points and dilution sets. We quote our final estimate of this exponent as $y_\tau = 1.32(2)$. This satisfies the generalized Josephson relation [17] for the compressibility $y_\tau = d - z$ within error bars.

Spinwave stiffness in the space dimensions is much smaller and thus has larger statistical errors. Independent fits were not possible for this data set. However, we fit the data with the functional form $y_s = aL^{-y_s}(1+bL^{-\omega})$ fixing the exponents via the generalized Josephson relations $y_s = d + z - 2$. Fixing $y_s = 2.67$ and $\omega = 1.18$ (from earlier fits) yields a reasonable fit to the data ($\tilde{\chi}^2 \approx 0.03$), in agreement with expectations.

3.5. PERCOLATION TRANSITION

So far, we have analyzed "generic" transitions that are driven by tuning of the (classical) temperature for dilutions $p < p_c$. Another type of transition – the percolation transition – can occur by tuning the dilution concentration p through the percolation threshold p_c of the lattice at very low temperature. The critical behavior of these transitions is entirely dependent on the critical geometry of percolating lattice with the dynamics of the rotor model unaffected, remaining locally ordered on each percolating cluster. A theory has been developed [54] that predicts the critical behavior of this percolation quantum phase transition. These predictions give exponents $\beta = 0.417$, $\gamma = 4.02$, $\nu = 0.875$, and $z = 2.53$. Note that the static exponents β and ν as well as the percolation threshold p_c agree with the corresponding 3D classical percolation values (see, e.g., References [55],[56],[57])

To test these predictions we perform simulations with dilution right at the percolation threshold $p = p_c = 0.688392$ and temperature $T = 1.0$, well below the estimated multicritical temperature $T_{MCP} \approx 1.35$. The large value of the predicted z leads to the need for very large system sizes L_τ to confirm the dynamical critical exponent. To reduce the numerical effort, we simulated systems with the dynamical exponent fixed at its predicted value $z = 2.53$ and used these optimally shaped systems to confirm the remaining critical exponents. Figure 12 shows both order parameter m and susceptibility χ for these systems up to $L = 28$. Considering the small system sizes in our data, we fit both sets to their predicted scaling forms with first-order corrections included. For the order parameter exponent, theory predicts $\beta/\nu \approx 0.47657$. Fitting the data to the form $m = aL^{-\beta/\nu}(1 + bL^{-\omega})$ with the critical exponent β/ν fixed at the predicted value, leads to a good fit ($\tilde{\chi}^2 \approx 1.41$) with irrelevant exponent $\omega = 0.99(12)$. Similarly, for the susceptibility exponent theory predicts $\gamma/\nu \approx 4.59429$. Fitting this data to $\chi = aL^{\gamma/\nu}(1 + bL^{-\omega})$ while fixing the critical exponent γ/ν to it's predicted value, leads to fits of lesser quality ($\tilde{\chi}^2 \approx 5.31$), but still within reasonable agreement with the theory, and giving an irrelevant exponent $\omega = 1.26(58)$.

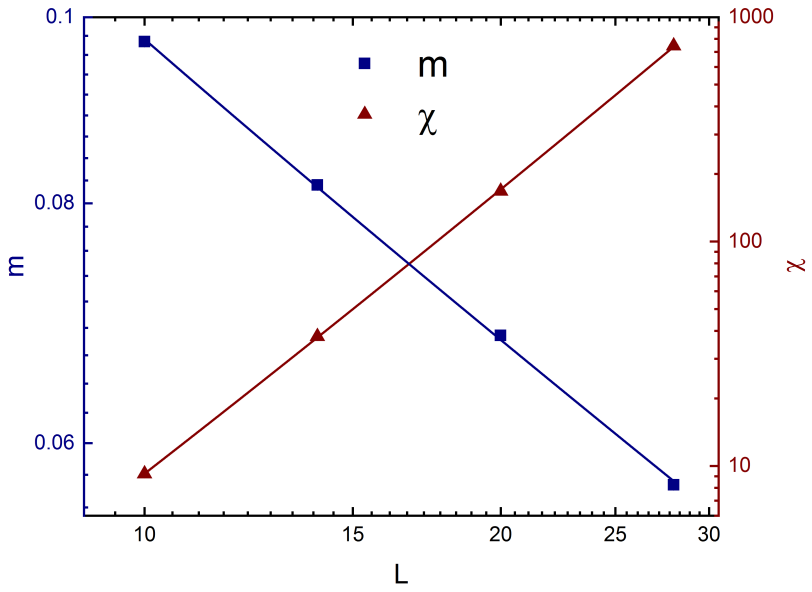

Figure 12. Log-log plot of observables m and χ for the percolation transition at $p_c = 0.688392$ and $T = 1.0$. Dashed lines are fits to the expectations [54]. Statistical errors are of the order of the symbol size.

4. CONCLUSIONS

In conclusion, we have carried out large-scale Monte Carlo simulations to determine the critical behavior of the superfluid-Mott glass quantum phase transition in three space dimensions. To do so we have mapped a site-diluted quantum rotor model with commensurate filling and off-diagonal disorder onto a (3+1)-dimensional classical XY model, and simulated it via the standard Metropolis and Wolff algorithms.

In the absence of disorder, the superfluid-Mott insulator transition falls into the four-dimensional XY universality class which features mean-field critical behavior with logarithmic corrections. The correlation exponent takes the value $\nu = 1/2$ that violates the Harris criterion $d\nu > 2$. As a consequence, the superfluid-Mott glass transition occurring in the disordered case shows critical behavior differing from that of the clean case.

Table 1. Critical exponents found in this work. Italic values are not calculated directly but represent theoretical values that we have used and/or confirmed in the simulations.

Our results	z	β/ν	γ/ν	ν	η
Clean	*1*	1.00(2)	2.00(6)	0.50(5)	0.00(5)
Diluted	1.67(6)	1.09(3)	2.50(3)	0.90(5)	−0.50(3)
Percolation	*2.53*	*0.477*	*4.594*	*0.875*	*−2.594*

This superfluid-Mott glass transition exhibits a conventional finite-disorder quantum critical point with power-law dynamical scaling $\xi_\tau \sim \xi_s^z$ between the correlation time and length. This agrees with a general classification of disordered quantum phase transitions based on rare region dimensionality in the system [20, 54]. For the classical (mapped) Hamiltonian (2), the rare regions are infinitely-long rods in the time-dimension, giving a rare region dimensionality $d_{RR} = 1$. Comparing this to the lower critical dimension of the classical XY model $D_c^- = 2$ we can see that $d_{RR} < D_c^-$, putting the system into class A (of conventional power-law scaling), as designated by the classification scheme.

For the generic transition occurring for dilutions p below the lattice percolation threshold p_c, we find universal, dilution-independent critical exponents from our Monte Carlo data. These exponents, summarized in Table 1, satisfy the hyperscaling relation as well as the Harris criterion. We have also considered the percolation transition that occurs across the percolation threshold p_c at low temperature. The critical behavior of this transition is also of conventional power-law type and our Monte Carlo data can be fitted well with theoretical behavior predicted within the scaling theory by Vojta and Schmalian[54].

An experimental realization of the three-dimensional superfluid-Mott glass transition can be found in diluted anisotropic spin-1 antiferromagnets. These systems are typically three-dimensional and exhibit particle-hole symmetry naturally as a consequence of the up-down symmetry of the Hamiltonian in the absence of external magnetic field. Such a realization was recently observed in bromine-doped dichloro-tetakic-thiourea-nickel[12].

Further experimental studies can be carried out in disordered bosonic systems such as ultracold atoms in optical lattices as well as granular superconductors. However, often only *statistical* particle-hole symmetry can be achieved in these systems. Whether or not this statistical particle-hole symmetry will destabilize the Mott glass into a Bose glass remains still unresolved.

ACKOWLEDGMENTS

This work was supported in part by the NSF under Grants No. PHY-1125915 and DMR-1506152. T.V. acknowledges the hospitality of the Kavli Institute for Theoretical Physics, where part of the work was performed.

REFERENCES

[1] B. C. Crooker, B. Hebral, E. N. Smith, Y. Takano, and J. D. Reppy. Superfluidity in a dilute bose gas. *Phys. Rev. Lett.*, 51:666–669, Aug 1983. doi: 10.1103/PhysRevLett.51.666.

[2] J. D. Reppy. ^{4}he as a dilute bose gas. *Physica B+C*, 126:335, 1984.

[3] D. B. Haviland, Y. Liu, and A. M. Goldman. Onset of superconductivity in the two-dimensional limit. *Phys. Rev. Lett.*, 62:2180–2183, May 1989. doi: 10.1103/PhysRevLett.62.2180.

[4] A. F. Hebard and M. A. Paalanen. Magnetic-field-tuned superconductor-insulator transition in two-dimensional films. *Phys. Rev. Lett.*, 65:927–930, Aug 1990. doi: 10.1103/PhysRevLett.65.927.

[5] H. S. J. van der Zant, F. C. Fritschy, W. J. Elion, L. J. Geerligs, and J. E. Mooij. Field-induced superconductor-to-insulator transitions in josephson-junction arrays. *Phys. Rev. Lett.*, 69:2971–2974, Nov 1992. doi: 10.1103/PhysRevLett.69.2971.

[6] H. S. J. van der Zant, W. J. Elion, L. J. Geerligs, and J. E. Mooij. Quantum phase transitions in two dimensions: Experiments in josephson-junction arrays. *Phys. Rev. B*, 54:10081–10093, Oct 1996. doi: 10.1103/PhysRevB.54.10081.

[7] M. White, M. Pasienski, D. McKay, S. Q. Zhou, D. Ceperley, and B. DeMarco. Strongly interacting bosons in a disordered optical lattice. *Phys. Rev. Lett.*, 102: 055301, Feb 2009. doi: 10.1103/PhysRevLett.102.055301.

[8] Sebastian Krinner, David Stadler, Jakob Meineke, Jean-Philippe Brantut, and Tilman Esslinger. Superfluidity with disorder in a thin film of quantum gas. *Phys. Rev. Lett.*, 110:100601, Mar 2013. doi: 10.1103/PhysRevLett.110.100601.

[9] Chiara D'Errico, Eleonora Lucioni, Luca Tanzi, Lorenzo Gori, Guillaume Roux, Ian P. McCulloch, Thierry Giamarchi, Massimo Inguscio, and Giovanni Modugno. Observation of a disordered bosonic insulator from weak to strong interactions. *Phys. Rev. Lett.*, 113:095301, Aug 2014. doi: 10.1103/PhysRevLett.113.095301.

[10] Akira Oosawa and Hidekazu Tanaka. Random bond effect in the quantum spin system $(tl_{1-x}k_x)cucl_3$. *Phys. Rev. B*, 65:184437, May 2002. doi: 10.1103/PhysRevB.65.184437.

[11] Tao Hong, A. Zheludev, H. Manaka, and L.-P. Regnault. Evidence of a magnetic bose glass in $(CH_3)_2chnh_3Cu(Cl_{0.95}Br_{0.05})_3$ from neutron diffraction. *Phys. Rev. B*, 81: 060410, Feb 2010. doi: 10.1103/PhysRevB.81.060410.

[12] Rong Yu, Liang Yin, Neil S. Sullivan, J. S. Xia, Chao Huan, Armando Paduan-Filho, Nei F. Oliveira Jr., Stephan Haas, Alexander Steppke, Corneliu F. Miclea, Franziska Weickert, Roman Movshovich, Eun-Deok Mun, Brian L. Scott, Vivien S. Zapf, and Tommaso Roscilde. Bose glass and mott glass of quasiparticles in a doped quantum magnet. *Nature*, 489:379, 2012.

[13] D. Hüvonen, S. Zhao, M. Månsson, T. Yankova, E. Ressouche, C. Niedermayer, M. Laver, S. N. Gvasaliya, and A. Zheludev. Field-induced criticality in a gapped quantum magnet with bond disorder. *Phys. Rev. B*, 85:100410, Mar 2012. doi: 10.1103/PhysRevB.85.100410.

[14] Andrey Zheludev and Tommaso Roscilde. Dirty-boson physics with magnetic insulators. *Comp. Ren. Phys.*, 14(8):740 – 756, 2013. ISSN 1631-0705. doi: https://doi.org/10.1016/j.crhy.2013.10.001.

[15] T. Giamarchi and H. J. Schulz. Anderson localization and interactions in one-dimensional metals. *Phys. Rev. B*, 37:325–340, Jan 1988. doi: 10.1103/PhysRevB.37.325.

[16] Daniel S. Fisher and Matthew P. A. Fisher. Onset of superfluidity in random media. *Phys. Rev. Lett.*, 61:1847–1850, Oct 1988. doi: 10.1103/PhysRevLett.61.1847.

[17] M. P. A. Fisher, P. B. Weichman, G. Grinstein, and D. S. Fisher. Boson localization and the superfluid-insulator transition. *Phys. Rev. B*, 40(1):546–570, Jul 1989. doi: 10.1103/PhysRevB.40.546.

[18] R. B. Griffiths. Nonanalytic behavior above the critical point in a random Ising ferromagnet. *Phys. Rev. Lett.*, 23:17, 1969. doi: 10.1103/PhysRevLett.23.17.

[19] M. Thill and D. A. Huse. Equilibrium behaviour of quantum Ising spin glass. *Physica A*, 214:321, 1995. doi: 10.1016/0378-4371(94)00247-Q.

[20] T. Vojta. Rare region effects at classical, quantum, and non-equilibrium phase transitions. *J. Phys. A*, 39:R143, 2006. doi: 10.1088/0305-4470/39/22/R01.

[21] T. Vojta. Quantum Griffiths effects and smeared phase transitions in metals: theory and experiment. *J. Low Temp. Phys.*, 161:299, 2010. doi: 10.1007/s10909-010-0205-4.

[22] Peter B. Weichman and Ranjan Mukhopadhyay. Critical dynamics of the dirty boson problem: Revisiting the equality $z = d$. *Phys. Rev. Lett.*, 98:245701, Jun 2007. doi: 10.1103/PhysRevLett.98.245701.

[23] Anand Priyadarshee, Shailesh Chandrasekharan, Ji-Woo Lee, and Harold U. Baranger. Quantum phase transitions of hard-core bosons in background potentials. *Phys. Rev. Lett.*, 97:115703, Sep 2006. doi: 10.1103/PhysRevLett.97.115703.

[24] Hannes Meier and Mats Wallin. Quantum critical dynamics simulation of dirty boson systems. *Phys. Rev. Lett.*, 108:055701, Jan 2012. doi: 10.1103/PhysRevLett.108.055701.

[25] Ray Ng and Erik S. Sørensen. Quantum critical scaling of dirty bosons in two dimensions. *Phys. Rev. Lett.*, 114:255701, Jun 2015. doi: 10.1103/PhysRevLett.114.255701.

[26] Juan Pablo Álvarez Zúñiga, David J. Luitz, Gabriel Lemarié, and Nicolas Laflorencie. Critical properties of the superfluid¯bose-glass transition in two dimensions. *Phys. Rev. Lett.*, 114:155301, Apr 2015. doi: 10.1103/PhysRevLett.114.155301.

[27] Zhiyuan Yao, Karine P. C. da Costa, Mikhail Kiselev, and Nikolay Prokof'ev. Critical exponents of the superfluid˘bose-glass transition in three dimensions. *Phys. Rev. Lett.*, 112:225301, Jun 2014. doi: 10.1103/PhysRevLett.112.225301.

[28] Rong Yu, Corneliu F. Miclea, Franziska Weickert, Roman Movshovich, Armando Paduan-Filho, Vivien S. Zapf, and Tommaso Roscilde. Quantum critical scaling at a bose-glass/superfluid transition: Theory and experiment for a model quantum magnet. *Phys. Rev. B*, 86:134421, Oct 2012. doi: 10.1103/PhysRevB.86.134421.

[29] T. Giamarchi, P. L. Doussal, and E. Orignac. Competition of random and periodic potentials in interacting fermionic systems and classical equivalents: The mott glass. *Phys. Rev. B*, 64:245119, Dec 2001. doi: 10.1103/PhysRevB.64.245119.

[30] Peter B. Weichman and Ranjan Mukhopadhyay. Particle-hole symmetry and the dirty boson problem. *Phys. Rev. B*, 77:214516, Jun 2008. doi: 10.1103/PhysRevB.77.214516.

[31] Thomas Vojta, Jack Crewse, Martin Puschmann, Daniel Arovas, and Yury Kiselev. Quantum critical behavior of the superfluid-mott glass transition. *Phys. Rev. B*, 94: 134501, Oct 2016. doi: 10.1103/PhysRevB.94.134501.

[32] Nikolay Prokof'ev and Boris Svistunov. Superfluid-insulator transition in commensurate disordered bosonic systems: Large-scale worm algorithm simulations. *Phys. Rev. Lett.*, 92:015703, Jan 2004. doi: 10.1103/PhysRevLett.92.015703.

[33] S. Iyer, D. Pekker, and G. Refael. Mott glass to superfluid transition for random bosons in two dimensions. *Phys. Rev. B*, 85:094202, Mar 2012. doi: 10.1103/PhysRevB.85.094202.

[34] Mason Swanson, Yen Lee Loh, Mohit Randeria, and Nandini Trivedi. Dynamical conductivity across the disorder-tuned superconductor-insulator transition. *Phys. Rev. X*, 4:021007, Apr 2014. doi: 10.1103/PhysRevX.4.021007.

[35] H.G. Ballesteros, L.A. Fernández, V.A. Martín-Mayor, A.M. Sudupe, and J.J. Ruiz-Lorenzo. Scaling corrections: site percolation and ising model in three dimensions. *J. Phys. A*, 32:1, 1999.

[36] A. B. Harris. Effect of random defects on the critical behaviour of Ising models. *J. Phys. C*, 7:1671, 1974. doi: 10.1088/0022-3719/7/9/009.

[37] J. T. Chayes, L. Chayes, D. S. Fisher, and T. Spencer. Finite-size scaling and correlation lengths for disordered systems. *Phys. Rev. Lett.*, 57:2999, 1986.

[38] R. Kenna. Finite-size scaling for $o(n)$ ϕ^4-theory at the upper critical dimension. *Nucl. Phys. B*, 691:292, 2004.

[39] M. Wallin, E. S. Sorensen, S. M. Girvin, and A. P. Young. Superconductor-insulator transition in two-dimensional dirty boson systems. *Phys. Rev. B*, 49:12115, 1994.

[40] M. N. Barber. Finite-size scaling. In C. Domb and J. L. Lebowitz, editors, *Phase Transitions and Critical Phenomena*, volume 8, pages 145–266. Academic, New York, 1983.

[41] F. Cooper, B. Freedman, and D. Preston. Solving phi4 field theory with Monte-carlo. *Nucl. Phys. B*, 210:210, 1982.

[42] J. K. Kim. Application of finite size scaling to Monte-Carlo simulations. *Phys. Rev. Lett.*, 70:1735, 1993.

[43] S. Caracciolo, A. Gambassi, M. Gubinelli, and A. Pelissetto. Finite-size correlation length and violations of finite-size scaling. *Eur. Phys. J. B*, 20:255, 2001. doi: 10.1007/BF01352587.

[44] Thomas Vojta and José A. Hoyos. Criticality and quenched disorder: Harris criterion versus rare regions. *Phys. Rev. Lett.*, 112:075702, Feb 2014. doi: 10.1103/PhysRevLett.112.075702.

[45] M. Guo, R. N. Bhatt, and D. A. Huse. Quantum critical behavior of a three-dimensional Ising spin glass in a transverse magnetic field. *Phys. Rev. Lett.*, 72:4137, 1994.

[46] H. Rieger and A. P. Young. Zero-temperature quantum phase transition of a two-dimensional Ising spin glass. *Phys. Rev. Lett.*, 72:4141, 1994.

[47] R. Sknepnek, T. Vojta, and M. Vojta. Exotic vs. conventional scaling and universality in a disordered bilayer quantum Heisenberg antiferromagnet. *Phys. Rev. Lett.*, 93: 097201, 2004.

[48] S. Teitel and C. Jayaprakash. Phase transtions in frustrated two-dimensional XY models. *Phys. Rev. B*, 27:598–601, Jan 1983. doi: 10.1103/PhysRevB.27.598.

[49] N. Metropolis, A. Rosenbluth, M. Rosenbluth, and A. Teller. Equation of state calculations by fast computing machines. *J. Chem. Phys.*, 21:1087, 1953.

[50] U. Wolff. Collective Monte-Carlo updating for spin systems. *Phys. Rev. Lett.*, 62:361, 1989.

[51] H. G. Ballesteros, L. A. Fernández, V. Martín-Mayor, A. Muñoz Sudupe, G. Parisi, and J. J. Ruiz-Lorenzo. Critical exponents of the three-dimensional diluted ising model. *Phys. Rev. B*, 58:2740–2747, Aug 1998. doi: 10.1103/PhysRevB.58.2740.

[52] H. G. Ballesteros, L. A. Fernandez, V. Martin-Mayor, A. Munoz Sudupe, G. Parisi, and J. J. Ruiz-Lorenzo. The four-dimensional site-diluted ising model: A finite-size scaling study. *Nucl. Phys. B*, 512:681, 1998.

[53] Qiong Zhu, Xin Wan, Rajesh Narayanan, José A. Hoyos, and Thomas Vojta. Emerging criticality in the disordered three-color ashkin-teller model. *Phys. Rev. B*, 91:224201, Jun 2015. doi: 10.1103/PhysRevB.91.224201.

[54] T. Vojta and J. Schmalian. Percolation quantum phase transitions in diluted magnets. *Phys. Rev. Lett.*, 95:237206, 2005.

[55] Junfeng Wang, Zongzheng Zhou, Wei Zhang, Timothy Garoni, and Youjin Deng. Bond and site percolation in three dimensions. *Phys. Rev. E.*, 87:052107, 2014.

[56] X Xu, J. Wang, J-P. Lv, and Y. Deng. *Front. Phys.*, 9:113, 2014.

[57] D. Stauffer and A. Aharony. *Introduction to Percolation Theory*. CRC Press, Boca Raton, 1991.

III. COLLECTIVE MODES AT A DISORDERED QUANTUM PHASE TRANSITION

Martin Puschmann[1], Jack Crewse[1], José Hoyos[2], Thomas Vojta[1]
[1] Department of Physics, Missouri University of Science and Technology
Rolla, MO 65409, USA
[2] Instituto de Física de São Carlos, Universidade de São Paulo,
C.P. 369, São Carlos, São Paulo 13560-970, Brazil

ABSTRACT

We study the collective excitations, i.e., the Goldstone (phase) mode and the Higgs (amplitude) mode, near the superfluid–Mott glass quantum phase transition in a two-dimensional system of disordered bosons. Using Monte Carlo simulations as well as an inhomogeneous quantum mean-field theory with Gaussian fluctuations, we show that the Higgs mode is strongly localized for all energies, leading to a noncritical scalar response. In contrast, the lowest-energy Goldstone mode undergoes a striking delocalization transition as the system enters the superfluid phase. We discuss the generality of these findings and experimental consequences, and we point out potential relations to many-body localization.

Understanding the rich behavior that arises when many quantum particles interact with each other remains one of the major challenges of modern condensed matter physics. Zero-temperature phase transitions between different quantum ground states have emerged as a central ordering principle in this field [1, 2, 3, 4, 5, 6]. These quantum phase transitions (QPTs) control large regions of a material's phase diagram and lead to unconventional thermodynamic and transport properties. Moreover, fluctuations associated with these transitions can induce novel phases, increasing the complexity of quantum matter.

Since impurities, defects, and other types of quenched disorder are unavoidable in most condensed matter systems, the effects of randomness on QPTs have been studied intensively over the last two decades, leading to the discovery of exotic phenomena such as

infinite-randomness critical points [7, 8], smeared phase transitions [9, 10], and quantum Griffiths singularities [11, 12]. Today, the thermodynamics of many disordered QPTs is well understood, and classification schemes [13, 14, 15] have been established based on the scaling of the disorder strength under coarse graining as well as on the importance of rare disorder fluctuations (see, e.g., Reference [16, 17, 18] and references therein).

Much less is known about the character and dynamics of excitations at disordered QPTs even though excitations are crucial for a host of experiments ranging from inelastic neutron scattering in magnetic materials to various electrical and thermal transport measurements. Of particular interest are the collective excitations that emerge in systems with spontaneously broken continuous symmetries. These include one or more Goldstone modes that are related to oscillations of the order parameter direction and an amplitude (Higgs) mode that is related to oscillations of the order parameter magnitude. Examples of such modes can be found in superfluids, superconductors, incommensurate charge density waves, as well as planar and Heisenberg magnets (see, e.g., References [19, 20]).

In this Letter, we therefore investigate the excitations close to a paradigmatic disordered QPT, the superfluid-Mott glass transition of disordered bosons, by means of Monte Carlo simulations and an inhomogeneous mean-field theory with Gaussian fluctuations. Our results can be summarized as follows. Even though the thermodynamic critical behavior of the superfluid-Mott glass transition is of conventional power-law type [21, 22], the Higgs and Goldstone modes feature unconventional dynamics that violates naive scaling. Specifically, the Higgs mode is strongly localized, resulting in a broad, noncritical spectral density close to the QPT. In contrast, the incipient Goldstone mode features a striking delocalization transition as the system enters the superfluid phase, irrespective of the disorder strength.

In the remainder of this Letter, we first introduce our model and then discuss the Monte Carlo simulations. To explain the unusual, noncritical response observed in these simulations, we study Gaussian fluctuations about an inhomogeneous quantum mean-field theory. We also discuss possible experiments, and consider relations to many-body localization.

We start from a square-lattice Bose-Hubbard Hamiltonian

$$H = \frac{1}{2}\sum_i U_i(n_i - \bar{n})^2 - \sum_{\langle ij\rangle} J_{ij}(a_i^\dagger a_j + \text{h.c.}) \tag{1}$$

with large integer filling $\bar{n}$. Here $a_i^\dagger$ and a are the boson creation and annihilation operators at site i, and $n_i = a_i^\dagger a_i$ is the number operator. If the interactions U_i and the nearest-neighbor hopping terms J_{ij} are spatially uniform, the system undergoes a QPT between a superfluid ground state (for $J \gg U$) and a gapped, incompressible Mott insulator (for $J \ll U$). In the presence of quenched disorder, these two bulk phases are separated by the Mott glass phase, a gapless but incompressible insulator [23, 24]. In the following, we introduce the disorder via site dilution, i.e., we randomly remove a nonzero fraction p of lattice sites while the U_i and J_{ij} of the remaining sites stay uniform.

To study the collective modes across the superfluid-Mott glass transition, we map the Bose-Hubbard model (1) onto a $(2 + 1)$-dimensional XY model [25] with columnar defects. We then perform large-scale Monte Carlo simulations for lattices with linear sizes of up to $L = 256$ and $L_\tau = 512$ in the space and imaginary time directions. The phase diagram and the thermodynamic critical behavior (which is of conventional power-law type) are known accurately from earlier studies [22, 26]. For details of the simulations and the data analysis see the Supplemental Material.[5]

[5]See Supplementary Material with References [27, 28, 29, 30, 31, 32, 33, 34, 35, 36, 37, 38, 39] for details of the Monte Carlo simulations, the scaling form of the scalar susceptibility, the maximum-entropy method, and the quantum mean-field theory.

To analyze the Higgs mode, we compute the (disorder-averaged) imaginary-time scalar susceptibility,

$$\chi_{\rho\rho}(\mathbf{x},\tau) \;=\; \langle\rho(\mathbf{x},\tau)\rho(0,0)\rangle - \langle\rho(\mathbf{x},\tau)\rangle\langle\rho(0,0)\rangle \tag{2}$$

and its Fourier transform $\tilde{\chi}_{\rho\rho}(\mathbf{q}, i\omega_m)$. Here, $\rho(\mathbf{x},\tau)$ is the local order parameter amplitude, obtained as the average of the XY variables over a small (five-site) cluster. The dynamic susceptibility is given by the analytic continuation from imaginary Matsubara frequencies $i\omega_m$ to real frequencies ω,

$$\chi_{\rho\rho}(\mathbf{q},\omega) = \tilde{\chi}_{\rho\rho}(\mathbf{q}, i\omega_m \to \omega + i0^+) \; . \tag{3}$$

Unfortunately, the analytic continuation is an ill-posed problem and sensitive to Monte Carlo noise. To overcome this problem, we employ a maximum-entropy (MaxEnt) method [40]. Its technical details and robustness are discussed in the Supplementary Material. Generalizing scaling arguments of Podolsky and Sachdev [41] to the disordered case suggests that the singular part of the scalar susceptibility in d space dimensions has the form

$$\chi_{\rho\rho}(\mathbf{q},\omega) = \omega^{[(d+z)\nu-2]/(\nu z)} X(\mathbf{q}r^{-\nu}, \omega r^{-\nu z}) \tag{4}$$

where r is the distance from criticality, ν is the correlation length exponent, z is the dynamical exponent, and X is a universal scaling function.

We now turn to the results of the Monte Carlo simulations. Figure 1 shows the spectral function $\chi''_{\rho\rho}(\mathbf{q},\omega)$ at $\mathbf{q} = 0$ on superfluid side of the QPT, contrasting the clean case ($p = 0$) with a diluted case ($p = 1/3$). The clean spectral function features a pronounced low-energy Higgs peak that softens as the transition is approached. The low-energy part of $\chi''_{\rho\rho}$ fulfills the scaling form (4) in good approximation, using the exponents $\nu = 0.671$ and

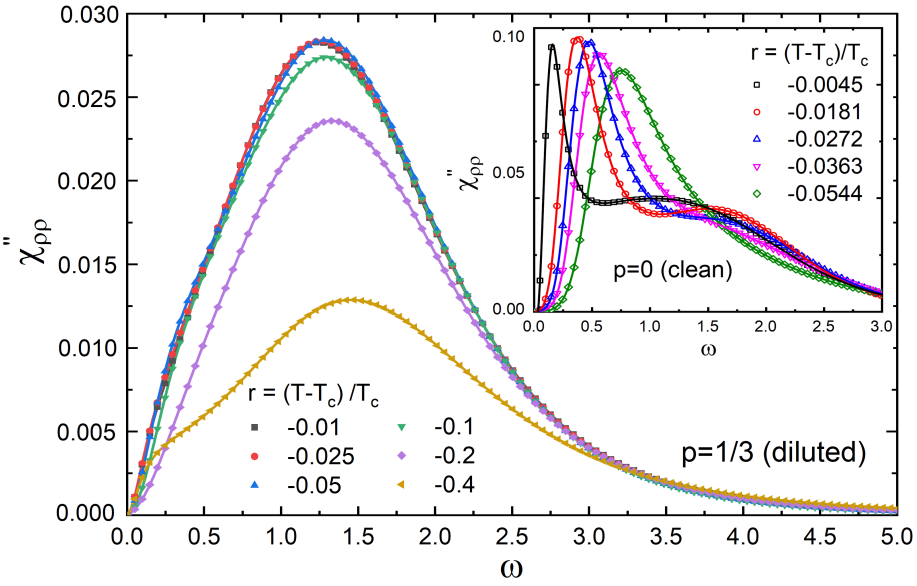

Figure 1. Spectral function $\chi''_{\rho\rho}(\mathbf{q} = 0, \omega)$ for different distances r from criticality on the superfluid side of the transition. Main panel: dilution $p = 1/3$, results averaged over 10,000 samples of sizes $L = 100, L_\tau = 452$. Inset: clean case ($p = 0$), $L = L_\tau = 128$. Statistical errors are small, about one symbol size; variations of the MaxEnt parameters can shift the peak positions systematically by up to about 10%. T is the Monte Carlo temperature, not the physical temperature of the Bose-Hubbard Hamiltonian.

$z = 1$ of the clean 3d XY universality class [42] (see Figure S1 in the Suppl. Material). These findings agree with previous simulations of the Higgs mode at the clean superfluid-Mott insulator transition [43, 44].

The spectral function of the diluted system behaves very differently. Instead of a narrow low-energy peak, it features a broad maximum at higher energies. Importantly, the position of this maximum is only weakly dependent on the distance r from criticality; it does not vanish for $r \to 0$. This behavior violates the scaling form (4), implying that the scalar susceptibility is dominated by a noncritical contribution.

We also study the dispersion $\omega_H(\mathbf{q})$ of the peak position as a function of the wave vector $\mathbf{q}$; the results are presented in Figure 2. In the clean case, the data show the behavior expected for a $z = 1$ quantum critical point. The low-energy dispersion is linear, $\omega_H \sim |\mathbf{q}|$,

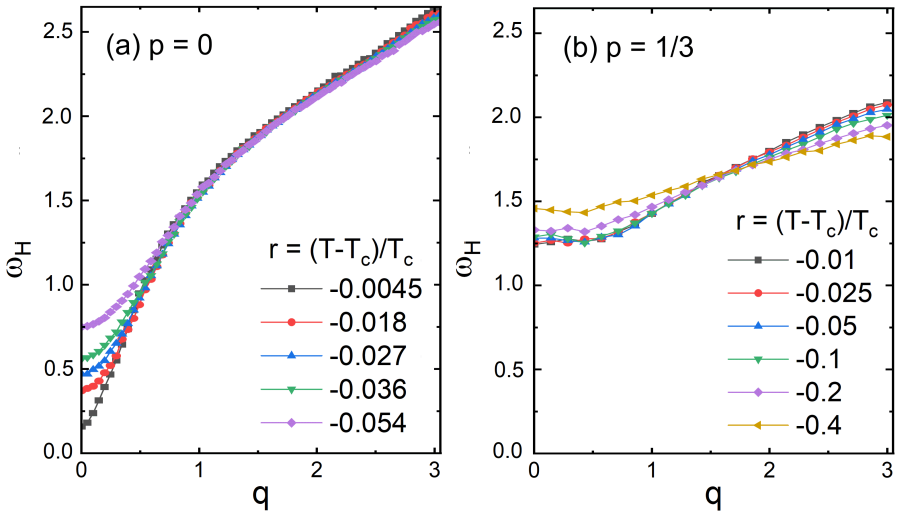

Figure 2. Peak position ω_H of the spectral function $\chi''_{\rho\rho}(\mathbf{q}, \omega)$ vs. wave vector $|\mathbf{q}|$ (along the coordinate directions) for different distances r from criticality. (a) dilution $p = 0$. (b) $p = 1/3$. The simulation parameters agree with Figure 1. Statistical errors are about a symbol size or less.

at criticality. As r increases, it crosses over to the quadratic form $\omega_H = m_H + c\mathbf{q}^2$. In contrast, the dispersion of the diluted system does not change much with the distance from criticality, and the peak energy ω_H is almost independent of $\mathbf{q}$ for small wave vectors.

What causes the broad, uncritical scalar response near the superfluid-Mott glass transition? Potential reasons include increased damping and localization effects. To gain further insight and to disentangle these possibilities, we complement the Monte Carlo simulations by an inhomogeneous mean-field theory with Gaussian fluctuations. Our approach generalizes the theories of References [45, 46] to the disordered case. It is also related to the bond-operator method for disordered magnets [47].

Close to the Mott phase, particle number fluctuations are small. We thus truncate the local Hilbert space at site j to three basis states, $|-_j\rangle$, $|0_j\rangle$, and $|+_j\rangle$, corresponding to the boson numbers $n_j = \bar{n} - 1, \bar{n}$, and $\bar{n} + 1$, respectively. The mean-field theory derives

from the variational ground state wave function $|\Phi_0\rangle = \prod_j |\phi_{0j}\rangle$ with

$$\begin{aligned} |\phi_{0j}\rangle &= \cos(\theta_j/2)|0_j\rangle \\ &\quad + \sin(\theta_j/2)\left(e^{i\eta_j}|+_j\rangle + e^{-i\eta_j}|-_j\rangle\right)/\sqrt{2}\,. \end{aligned} \tag{5}$$

It captures both the Mott state, $\theta_j = 0$, and the superfluid state, $\theta_j > 0$, with the local superfluid order parameter $\langle a_j^\dagger\rangle \propto \psi_j = \sin\theta_j e^{-i\eta_j}$.

The variational ground state energy $E_0 = \langle\Phi_0|H|\Phi_0\rangle$ is minimized by uniform phases $\eta_j = \eta = \text{const}$ (which we set to zero in the following) and mixing angles θ_i that fulfill the mean-field equations

$$U_i \sin\theta_i - 4\bar{n}\cos\theta_i \sum_j J_{ij}\sin\theta_j = 0\,. \tag{6}$$

To describe excitations on top of the mean-field ground state, we rotate the basis in the three-state local Hilbert space of site j to $|\phi_{0j}\rangle, |\phi_{Hj}\rangle, |\phi_{Gj}\rangle$ where

$$\begin{aligned} |\phi_{Hj}\rangle &= \sin(\theta_j/2)|0_j\rangle - \cos(\theta_j/2)\left(|+_j\rangle + |-_j\rangle\right)/\sqrt{2} \\ |\phi_{Gj}\rangle &= i\left(|+_j\rangle - |-_j\rangle\right)/\sqrt{2} \end{aligned} \tag{7}$$

are related to changes of order parameter magnitude and phase, respectively, compared to $|\phi_{0j}\rangle$. The boson operators $b_{0j}^\dagger$, $b_{Hj}^\dagger$, and $b_{Gj}^\dagger$ create these states out of the fictitious vacuum and fulfill the local constraint $\sum_\alpha b_{\alpha j}^\dagger b_{\alpha j} = 1$. We now rewrite the Hamiltonian (1) in terms of the b bosons, using the constraint to eliminate ("fully condense") b_{0j} such that $b_{Hj}^\dagger$ and $b_{Gj}^\dagger$ create excitations on top of the mean-field ground state. To quadratic (Gaussian) order in b, the Hamiltonian decouples into Higgs and Goldstone parts, $H = E_0 + H_H + H_G$, which

both take the form

$$H_\alpha = \sum_i A_{\alpha i} b^\dagger_{\alpha i} b_{\alpha i} + \sum_{\langle ij \rangle} B_{\alpha ij} (b^\dagger_{\alpha i} + b_{\alpha i})(b^\dagger_{\alpha j} + b_{\alpha j}) \ , \tag{8}$$

($\alpha = H, G$). The coefficients $A_{\alpha i}$ and $B_{\alpha ij}$ are nonuniform and depend on the mixing angles θ_i. H_H and H_G can be diagonalized numerically by bosonic Bogoliubov transformations, $b_{\alpha j} = \sum_k (u_{\alpha jk} d_{\alpha k} + v^*_{\alpha jk} d^\dagger_{\alpha k})$.

We now present the results of the mean-field theory. In the absence of dilution, $p = 0$, the mean-field equation (6) can be solved analytically. A superfluid solution appears for $U < U_c^0 = 4\bar{n}Jz$ where $z = 4$ is the coordination number of the lattice; it has a uniform mixing angle $\cos\theta = U/U_c^0$ and order parameter $\psi = (1 - U/U_c^0)^{1/2}$. As the system is translationally invariant, all excitations have plane wave character. In the superfluid phase, the Goldstone mode is gapless while the gapped Higgs mode softens at the QPT. In the insulating phase the two modes are gapped and degenerate. All clean mean-field results agree with earlier work [45].

The behavior changes dramatically in the presence of disorder. Figure 3 shows the average and typical order parameter for site dilutions $p = 1/8$ and $1/3$, resulting from a numerical solution of the mean-field equations (6) [6]. As expected, the onset of superfluidity is suppressed compared to the clean case, $p = 0$. The large difference between the average and typical order parameter for $U/(\bar{n}J)$ slightly below the onset of superfluidity indicates the coexistence of superfluid puddles with insulating regions, characteristic of a Griffiths phase (which is wider for stronger dilution). At lower U, the order parameter is only moderately inhomogeneous.

Turning to excitations on top of the mean-field ground state, Figure 4a visualizes examples of the lowest-energy eigenstates in both the Higgs and Goldstone channels for dilution $p = 1/3$. Clearly, these states show nontrivial localization proper-

[6] For each lattice, we only consider the infinite percolation cluster as finite clusters cannot support superfluid long-range order.

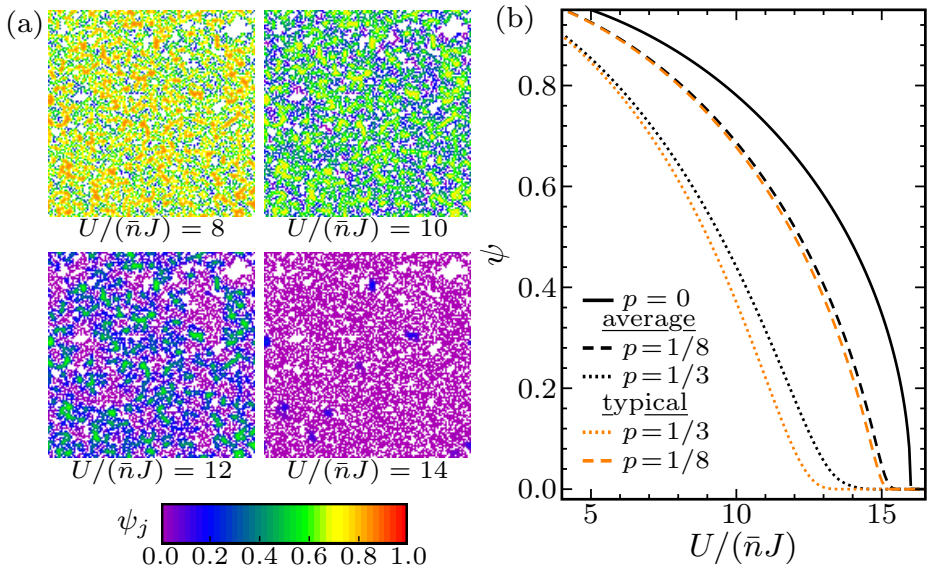

Figure 3. (a) Local order parameter ψ_j for several $U/(\bar{n}J)$ for for a system of 128^2 sites with dilution $p = 1/3$. (b) Average and typical (geometric average) local order parameter ψ as function of $U/(\bar{n}J)$ for dilutions $p = 0, 1/8$, and $1/3$, using 1000 disorder realizations. Statistical errors are comparable to the line widths.

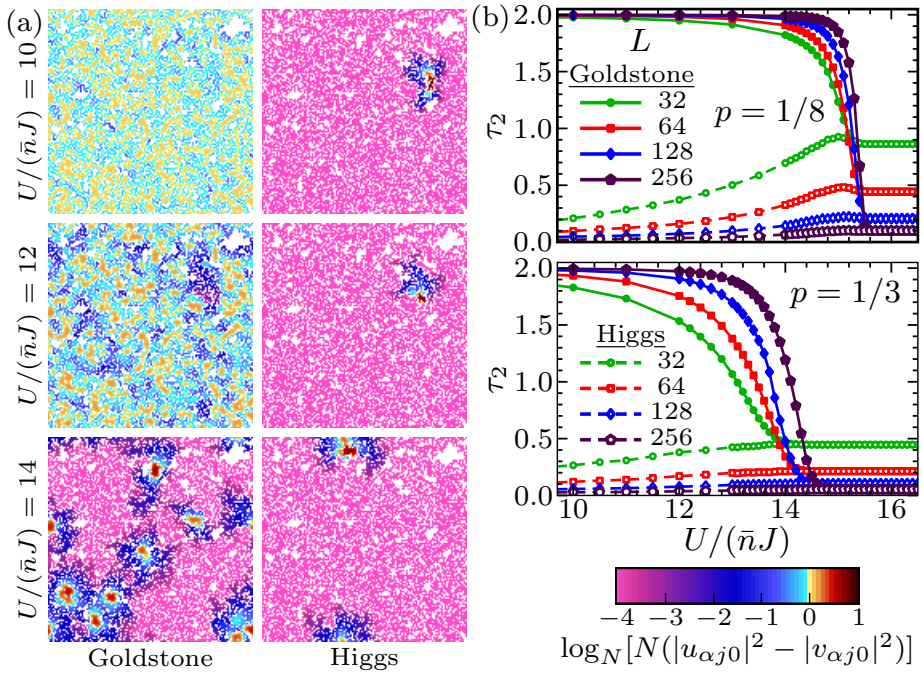

Figure 4. (a) Wave functions of the lowest-energy Goldstone and Higgs modes for $p = 1/3$ and several $U/(\bar{n}J)$, visualized as $|u_{\alpha j0}|^2 - |v_{\alpha j0}|^2$. (b) Generalized dimension τ_2 of the lowest-energy Goldstone and Higgs modes vs. interaction $U/(\bar{n}J)$ for $p = 1/8$ and $1/3$ (averaged over 1000 disorder realizations). Statistical errors are smaller than the symbol size.

ties. To characterize the localization, we calculate the inverse participation number $P^{-1}(0) = \sum_j (|u_{\alpha j0}|^2 - |v_{\alpha j0}|^2)^2$ [47] and the corresponding generalized dimension $\tau_2(0) = \ln P(0)/\ln L$ [7]. The dependence of τ_2 on the interaction U for the lowest-energy eigenstates in the Higgs and Goldstone channels is presented in Figure 4b. For both weak and strong dilutions, $p = 1/8$ and 1/3, we observe the same behavior. In the insulating phase, both excitations are degenerate and strongly localized as indicated by the rapid drop of τ_2 towards zero with increasing L.

Upon entering the superfluid phase with decreasing U, the two excitations evolve in opposite direction. The Higgs mode becomes even more localized, reflected in a further decrease of τ_2. In contrast, the lowest Goldstone excitation undergoes a rapid delocalization transition. Its dimension τ_2 increases quickly, and its L-dependence changes sign. It now increases towards $\tau_2 = 2$ with increasing L, indicating an extended state. Within our numerical accuracy, the crossing of the τ_2 vs. $U/(\bar{n}J)$ curves coincides with the onset of superfluid order. In fact, we have derived an analytic expression for the wave function of the lowest Goldstone excitation in the superfluid phase that proves that it is extended whenever the system features a macroscopic order parameter.

We also study the dependence of the localization on the excitation energy (see Supplementary Materials). On the insulating side, the excitations are strongly localized for all energies, and the same is true for the Higgs mode in the superfluid phase. Goldstone excitations with nonzero energy appear to be localized as well, with a localization length that diverges with vanishing energy. We do not find any evidence for a mobility edge at nonzero energy, in contrast to the Bose glass results reported in Reference [48].

To establish a connection to the Monte Carlo simulations, we compute the spectral densities of the Higgs and Goldstone Green functions $\chi_{\alpha jk}(t) = -i\Theta(t)\langle[b^\dagger_{\alpha j}(t) + b_{\alpha j}(t), b^\dagger_{\alpha k}(0) + b_{\alpha k}(0)]\rangle$ with $\alpha = G, H$. Figure 5 shows the spectral densities at zero wave vector for several interactions $U/(\bar{n}J)$, comparing the clean case with dilution $p = 1/3$.

[7] In our numerical calculations, we compute τ_2 via the box-counting method, see the Suppl. Material.

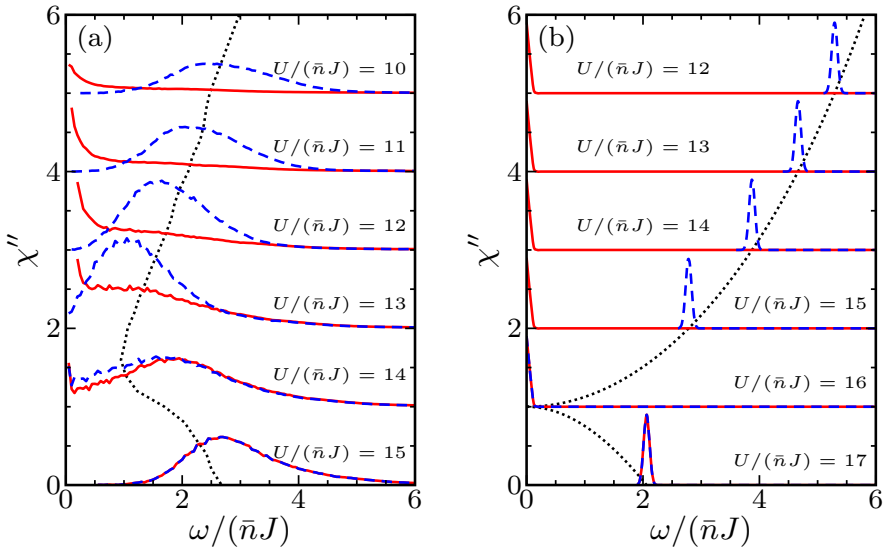

Figure 5. Spectral functions $\chi''(\mathbf{q} = 0, \omega)$ of the Goldstone (solid lines) Higgs (dashed lines) excitations for several interactions $U/(\bar{n}J)$. The curves are shifted upwards with increasing U. Dotted lines mark the position of the Higgs peak in χ''. (a) Dilution $p = 1/3$ (240 disorder realizations, statistical errors are comparable to the line widths). (b) Clean case, $p = 0$; here the peaks in the figure represent δ functions.

The spectral densities of the diluted system are very broad, even though the eigenmodes are noninteracting within the Gaussian approximation and thus have no intrinsic width. This demonstrates that the broadening of χ'' is due to disorder-induced localization effects. Moreover, the peak in the Higgs spectral function does not soften at the superfluid-Mott glass transition, mirroring the Monte Carlo results in Figure 1. In contrast, the clean spectral functions show the expected δ peaks at energies corresponding to the Higgs and Goldstone masses.

To summarize, we found the Higgs mode to be strongly localized across the superfluid-Mott glass QPT; the scalar response is thus noncritical and violates naive scaling. The lowest Goldstone excitation, in contrast, delocalizes upon entering the superfluid phase. Higher-energy Goldstone excitations are localized, implying the absence of a nonzero-energy mobility edge for the excitations.

The mean-field theory used in the second half of this Letter provides only an approximate description of the superfluid-Mott glass transition. In particular, it does not correctly capture rare regions effects because it cannot describe the fluctuations of large superfluid puddles in an insulating matrix. Whereas rare regions are known to be unimportant for the thermodynamics of this QPT [16, 17, 18], their effects on excitations are less well understood. Moreover, the Gaussian approximation for H_H and H_G neglects anharmonic effects (which could be included by keeping higher-order terms in the expansion of H). However, the agreement between the mean-field results and the numerically exact Monte Carlo simulations gives us confidence in their validity.

Potential routes to analyze the superfluid-Mott glass transition experimentally include ultracold atoms, dirty and granular superconductors, as well as diluted quantum antiferromagnets. Recently, the effects of the Higgs mode on the dynamical conductivity in disordered superconducting thin films were modeled by a bosonic Hamiltonian similar to ours [49, 50]. The Monte Carlo data in these papers appear to be compatible with a more conventional scenario in which the Higgs response sharpens and softens as the QPT is approached. We believe that this may stem from the comparatively weak disorder used in References [49, 50] which causes a slow crossover to the disordered behavior [8].

In conclusion, our work demonstrates that disordered QPTs can feature unconventional collective excitations even if their thermodynamic critical behavior is completely regular. This implies a number of important general questions about collective modes at disordered QPTs: Can one classify the excitation dynamics along similar lines as the thermodynamics? What is the character (and critical behavior) of the delocalization transition of the Goldstone mode? Under what conditions does a mobility edge appear? Is it related to many-body localization? What role is played by the space dimensionality? These questions remain tasks for the future.

[8] This is supported by the fact that the critical behavior found in Reference [49] agreed with a clean dynamical exponent $z = 1$ rather than the disordered value $z = 1.52$ [22].

ACKNOWLEDGMENTS

This work was supported by the NSF under Grant Nos. DMR-1506152, DMR-1828489, PHY-1125915 and PHY-1607611, by Conselho Nacional de Desenvolvimento Científico e Tecnológico (CNPq) under Grant No. 312352/2018-2, and by FAPESP under Grants No. 2015/23849-7 and No. 2016/10826-1. T.V. and J.A.H. acknowledge the hospitality of the Aspen Center for Physics, and T.V. thanks the Kavli Institute for Theoretical Physics where part of the work was performed.

SUPPLEMENTARY MATERIALS

In the following sections, we provide technical details about the Monte Carlo simulations, the scaling form of the scalar susceptibility, the maximum-entropy method used to analytically continue the imaginary-frequency susceptibilities, and the quantum mean-field theory.

1. DETAILS OF THE MONTE CARLO SIMULATIONS

The Monte Carlo simulations follow the approach used in References [22, 26] to study the thermodynamic critical behavior. For large integer filling $\bar{n}$, the square-lattice Bose-Hubbard Hamiltonian

$$H = \frac{1}{2}\sum_i U_i(n_i-\bar{n})^2 - \sum_{\langle ij\rangle} J_{ij}(a_i^\dagger a_j + \text{h.c.}) \tag{9}$$

can be mapped [25] onto a classical $(2+1)$-dimensional XY model on a cubic lattice. If the disorder is introduced by means of site dilution, the resulting classical Hamiltonian reads

$$H_{\text{cl}} = -J_s \sum_{\langle i,j\rangle,\tau} \epsilon_i\epsilon_j \mathbf{S}_{i,\tau}\cdot\mathbf{S}_{j,\tau} - J_t \sum_{i,\tau} \epsilon_i \mathbf{S}_{i,\tau}\cdot\mathbf{S}_{i,\tau+1} \tag{10}$$

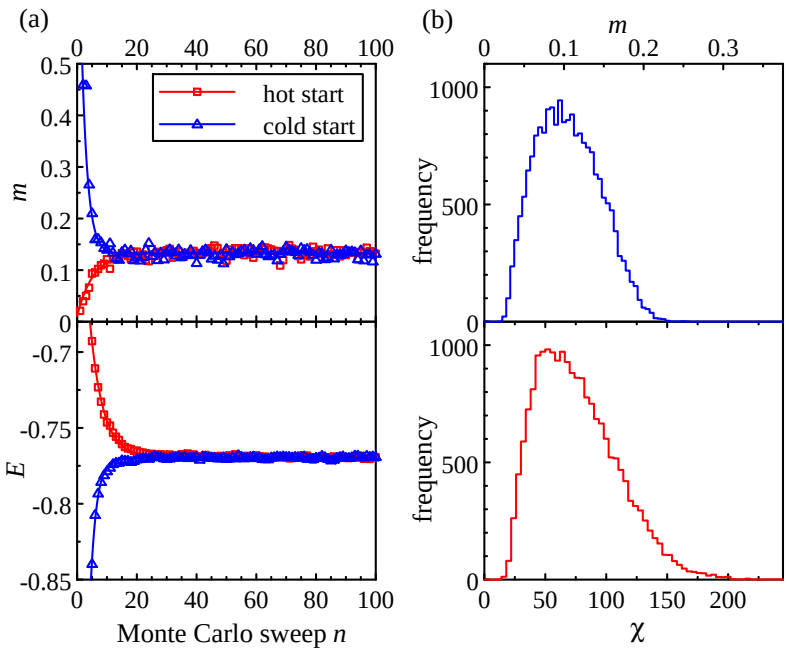

Figure 6. (a) Equilibration of energy and order parameter for a single disorder realization of size $L = 100, L_\tau = 452$, dilution $p = 1/3$, and temperature $T = T_c = 1.577$. The solid lines are fits to $E_n = E_{av} + a\exp(-n/t_{eq})$ (and analogously for m). (b) Histograms of the order parameter m and the order parameter susceptibility χ for $L = 44, L_\tau = 132$, $p = 1/3$, $T = T_c = 1.577$, using 20,000 disorder realizations. To obtain accurate values for each individual sample, 4000 measurements per sample were used in this calculation.

where $\mathbf{S}_{i,\tau}$ is a two-component unit vector at the lattice site with spatial coordinate i and "imaginary-time" coordinate τ. The independent quenched random variables ϵ_i take the values 0 (vacancy) with probability p and 1 (occupied site) with probability $1-p$. Because the vacancy positions do not depend on the imaginary-time coordinate τ, the defects in the classical model (10) are columnar. The values of the coupling constants J_s/T and J_t/T depend on the parameters of the original Bose-Hubbard model. T is the "classical" temperature of the Hamiltonian (10) whereas the physical temperature of the Bose-Hubbard model (9) maps onto the inverse system size in imaginary-time direction of the classical model. As we are interested in universal properties, the values of J_s and J_t are not important for the qualitative behavior. We therefore set $J_s = J_t = 1$ and vary the classical temperature T to tune through the transition.

We perform simulations of the classical Hamiltonian (10) by employing a combination of Wolff cluster updates [27] and Metropolis single-spin updates [28] for dilutions $p = 0, 1/8, 1/5$, and $1/3$. Specifically, a full Monte Carlo sweep consists of a Metropolis sweep followed by a Wolff sweep (a number of cluster flips such that the total number of flipped spins equals the system size). The Wolff updates greatly reduce the critical slowing down, and the Metropolis updates help equilibrate small disconnected clusters of lattice sites. The resulting equilibration and correlation times are very short. This can be seen in Figure 6(a) which shows the equilibration of the energy E and the order parameter m for a "worst-case example", i.e., high dilution, large system size, and a temperature right at criticality, $T = T_c$.

The figure demonstrates that the data for a hot start (random $\mathbf{S}$) and a cold start (all $\mathbf{S}$ perfectly aligned) rapidly overlap. Fits of the energy to $E_n = E_{av} + a \exp(-n/t_{eq})$ (and analogously for the order parameter) give equilibration times t_{eq} of about 5 sweeps or shorter, depending on the quantity and initial conditions.

Due to the large computational effort required for simulating disordered systems, one must carefully choose the number N_S of disorder realizations (samples) and the number N_M of measurements during the simulation of each sample for optimal performance. Assuming statistical independence between different measurements (quite possible with a cluster update), the variance σ_T^2 of the final result (thermodynamically and disorder averaged) for a particular observable can be estimated as

$$\sigma_T^2 \approx (\sigma_S^2 + \sigma_M^2/N_M)/N_S \tag{11}$$

where σ_S^2 is the disorder-induced variance between samples and σ_M^2 is the variance of measurements within each sample [33, 34]. Because the numerical effort is roughly proportional to $(N_M + N_E)N_S$ (where N_E is the number of equilibration sweeps per sample), the optimum value of N_M is quite small. We therefore employ a large number N_S of disorder

realizations, ranging from 10 000 to 20 000, and rather short runs of $N_M = 500$ sweeps, with measurements taken after every sweep. The equilibration period for each sample is $N_E = 100$ Monte Carlo sweeps, many times longer than the longest observed equilibration times t_{eq}. The combination of short Monte Carlo runs and large sample numbers can lead to biases in some observables, at least if the usual estimators are employed. We have corrected these biases by means of improved estimators, as discussed, e.g., in the appendix of Reference [34]. Moreover, for selected parameters, we have compared runs using as little as 250 and as many as 4000 measurement sweeps per sample and confirmed that they agree within their error bars.

To ascertain the importance of rare events, we compute the probability distributions of key observables. Figure 6(b) shows histograms of the order parameter and the order parameter susceptibility for dilution $p = 1/3$ right at the critical temperature. The distributions are moderately broad and do not feature long tails. This agrees with what is expected based on the classification of disordered phase transitions [14, 15]. The thermodynamic critical behavior of the superfluid-Mott glass transition is of conventional power-law type [22], implying a finite-disorder fixed point.

As the disorder breaks the symmetry between space and imaginary time, we need to distinguish the system sizes L (in the space directions) and L_τ (in the imaginary-time direction). Appropriate sample shapes can be found from the maxima of the Binder cumulant as described in References [29, 30, 31, 32]. This method yields combinations of L and L_τ with constant scaling ratio L_τ/L^z. To ensure that our results are not affected by finite-size effects, we use large systems with linear sizes up to $L = 256$ and $L_\tau = 512$ in the space and imaginary time directions. These sizes are much larger than the correlation lengths (in the space and imaginary time directions) of the studied excitations. For example, the smallest Higgs mass (peak frequency) for the clean system shown in the inset of Figure 1 of the main paper is $m_H \approx 0.14$ corresponding to a characteristic time of $2\pi/m_H \approx 45$, much smaller than the system size $L = L_\tau = 128$. To gain further confidence, we have

nonetheless confirmed that the results do not change for a system of size $L = L_\tau = 256$. In the presence of disorder, finite-size effects are even less of a problem because the Higgs mode localizes. (The maximum of the spectral density in the main panel of Figure 1 of the main paper is at a frequency of about 1.25 corresponding to a characteristic time of about 5). We have confirmed this by comparing the results for sizes between $L = 68, L_\tau = 256$ and $L = 109, L_\tau = 512$ for dilution $p = 1/3$.

To calculate the scalar susceptibility $\chi_{\rho\rho}$, we need to measure the local order parameter magnitude. In a "soft-spin" model, one could simply use $|\mathbf{S}_{i,\tau}|$ for this purpose. However, in our XY model, $|\mathbf{S}_{i,\tau}|$ is fixed at unity. We therefore define the local order-parameter magnitude via an average over a small five-site cluster,

$$\rho(\mathbf{x}_i, \tau) = \frac{1}{5}\left|\epsilon_i \mathbf{S}_{i,\tau} + \sum_j \epsilon_j \mathbf{S}_{j,\tau}\right| \tag{12}$$

where the sum is over the four (space) neighbors of lattice site i.

2. SCALING FORM OF THE SCALAR SUSCEPTIBILITY

Podolsky and Sachdev [41] derived a scaling form of the scalar susceptibility $\chi_{\rho\rho}$ at the clean superfluid-Mott insulator transition. We generalize this derivation to the Mott glass case by including quenched (random-mass) disorder and a dynamical exponent z different from unity. We start from a d-dimensional quantum field theory for an M-component vector order parameter ψ; it is defined by the action

$$S = \int d^d x d\tau \left[(\partial_{\mathbf{x}}\psi)^2 + (\partial_\tau \psi)^2 + (r + \delta r(\mathbf{x}))\psi^2 + u\psi^4\right] . \tag{13}$$

Here, $\delta r(\mathbf{x})$ represents the quenched random mass disorder and u is the standard quartic coefficient. For $d = 2$ and $M = 2$, the quantum phase transition of this field theory is in the same universality class as the superfluid-Mott glass transition of the Bose-Hubbard model

(9). The corresponding free-energy density is given by

$$f = -\frac{1}{\beta V} \ln Z = -\frac{1}{\beta V} \ln \int D[\psi] e^{-S} \tag{14}$$

where V is the system volume and β the inverse temperature. We take two derivatives of f w.r.t. the distance r from criticality yielding

$$\begin{aligned} \frac{\partial^2 f}{\partial r^2} &= \frac{1}{\beta V} \int d^d x d\tau \int d^d x' d\tau' \\ &\quad \times \left[\langle \psi^2(\mathbf{x}, \tau) \psi^2(\mathbf{x}', \tau') \rangle - \langle \psi^2(\mathbf{x}, \tau) \rangle \langle \psi^2(\mathbf{x}', \tau') \rangle \right] . \end{aligned} \tag{15}$$

This is the $\mathbf{q} = 0$, $\omega_n = 0$ Fourier component of the scalar susceptibility $\chi_{\rho\rho}$. (Actually, the expression yields the correlation function of the square of the order parameter magnitude rather than the magnitude itself. However, as the magnitude has a nonzero average at criticality, both these correlation functions have the same scaling behavior.)

The singular part of the free-energy density fulfills the homogeneity relation $f(r) = b^{-(d+z)} f(r b^{1/\nu})$ where b is an arbitrary scale factor. Taking two derivatives w.r.t. r gives the scale dimension of $\chi_{\rho\rho}$ as $-(d+z) + 2/\nu$. This implies the homogeneity relation

$$\chi_{\rho\rho}(r, \mathbf{q}, \omega) = b^{-(d+z)+2/\nu} \chi_{\rho\rho}(r b^{1/\nu}, \mathbf{q} b, \omega b^z) . \tag{16}$$

Setting $b = r^{-\nu}$ yields the scaling form

$$\chi_{\rho\rho}(r, \mathbf{q}, \omega) = r^{(d+z)\nu - 2} Y(\mathbf{q} r^{-\nu}, \omega r^{-\nu z}) \tag{17}$$

or, equivalently

$$\chi_{\rho\rho}(r, \mathbf{q}, \omega) = \omega^{[(d+z)\nu - 2]/(\nu z)} X(\mathbf{q} r^{-\nu}, \omega r^{-\nu z}) \tag{18}$$

as given in Eq. (4) of the main text. Setting $z = 1$ and $d = 2$, we recover the result of Podolsky and Sachdev for the clean superfluid-Mott insulator transition.

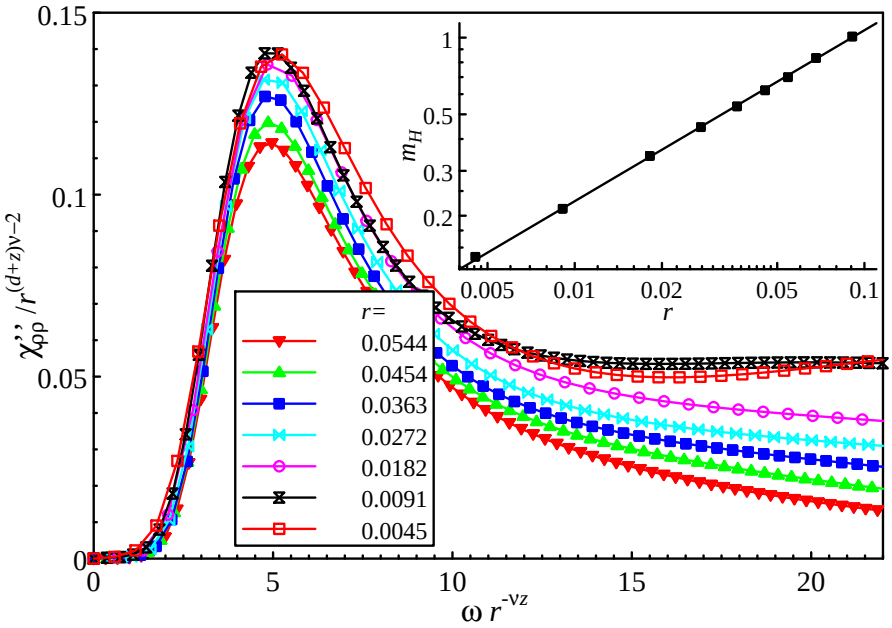

Figure 7. Scaling plot of the spectral function $\chi''_{\rho\rho}(r, \mathbf{q} = 0, \omega)$ on the superfluid side of the quantum phase transition in the undiluted case, $p = 0$. The results are averages over 2,000 samples of size $L = L_\tau = 256$. Inset: Energy of the Higgs peak in $\chi''_{\rho\rho}$, i.e., the Higgs mass m_H vs. distance from criticality r. The solid line is a fit of the expected power-law behavior $m_H \sim |r|^{\nu z}$ using the exponent values $\nu z = 0.671$ of the 3d XY universality class [42].

As an illustration, Figure 7 presents a scaling plot of our Monte Carlo data for the spectral function $\chi''_{\rho\rho}(r, \mathbf{q} = 0, \omega)$ in the undiluted case, $p = 0$. The figure shows that the low-energy part of $\chi''_{\rho\rho}$ fulfills the scaling form (17) in good approximation. For $r \lesssim 0.02$, the collapse of the Higgs peaks is nearly perfect. For larger r, the peak positions continue to follow the expected power-law behavior (as is also demonstrated in the inset of the figure) but the peak amplitudes show some deviations. This can be attributed to uncertainties of the maximum-entropy method, as is discussed in the next section.

It is interesting to analyze the scale dimension of $\chi_{\rho\rho}$ or, equivalently, the power of ω in front of the scaling function X in Eq. (18). In a disordered system, the correlation length exponent ν is known to fulfill the inequality $d\nu > 2$ [35]. The exponent of ω thus fulfills the inequality

$$[(d + z)\nu - 2]/(\nu z) > 1 \, . \tag{19}$$

This positive exponent implies that, in the presence of disorder, the amplitude of the singular part of $\chi_{\rho\rho}$ is strongly suppressed to zero as the quantum critical point is approached. Using the numerical values for z and ν found in Reference [22], the exponent takes the value $[(d+z)\nu - 2]/(\nu z) = 1.18$ in our problem.

3. MAXIMUM-ENTROPY METHOD

Within the Monte Carlo simulations, we compute the scalar susceptibility in imaginary time. The real-frequency susceptibility is given by the analytic continuation

$$\chi_{\rho\rho}(\mathbf{q}, \omega) = \tilde{\chi}_{\rho\rho}(\mathbf{q}, i\omega_m \rightarrow \omega + i0^+) \tag{20}$$

from imaginary Matsubara frequencies $i\omega_m$ to real frequencies ω. This amounts to inverting the relation

$$\tilde{\chi}_{\rho\rho}(\mathbf{q}, i\omega_m) = \frac{1}{\pi}\int_0^\infty d\omega \chi''_{\rho\rho}(\mathbf{q}, \omega)\frac{2\omega}{\omega_m^2 + \omega^2} \tag{21}$$

between the Matsubara susceptibility and the real-frequency spectral function $A(\mathbf{q}, \omega) = \chi''_{\rho\rho}(\mathbf{q}, \omega)$. Unfortunately, the kernel of this transformation, $K(\omega_m, \omega) = (2/\pi)\omega/(\omega_m^2 + \omega^2)$, is an ill-conditioned operator. This renders the inversion extremely sensitive to the unavoidable noise in the numerical data.

To overcome this problem, we employ a version of the maximum-entropy method [40]. To find the spectral function A, we minimize (with respect to the spectral function A that we wish to determine) the cost function

$$Q = \Delta - \alpha S \, . \tag{22}$$

The first term in Q, the error sum

$$\Delta = (\tilde{\chi} - KA)^T \Sigma (\tilde{\chi} - KA) \, , \tag{23}$$

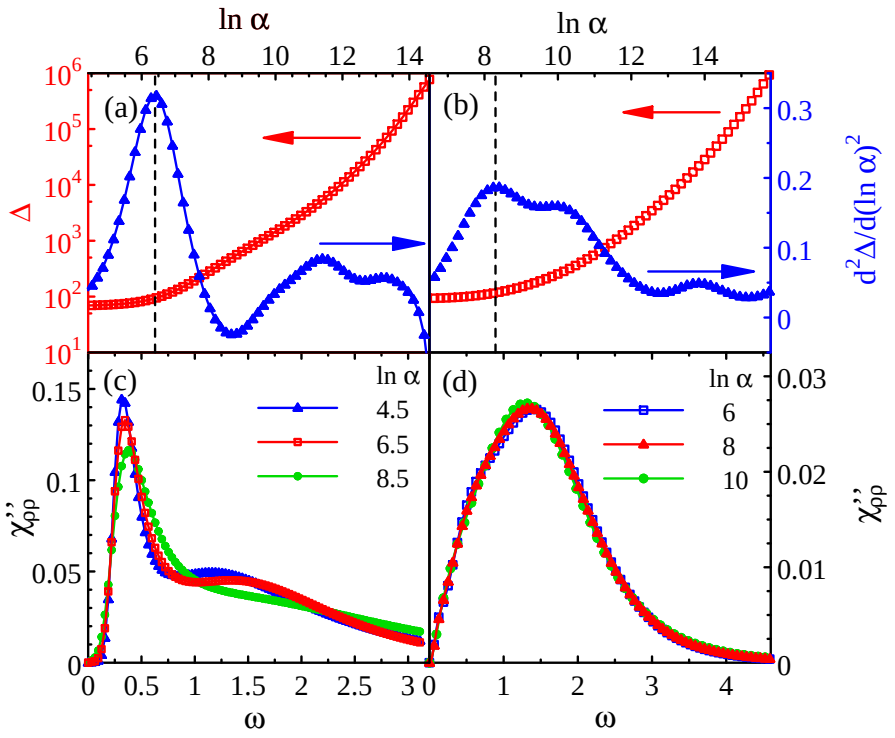

Figure 8. Maximum-entropy method for the Higgs spectral function. (a) Error sum Δ vs. $\ln\alpha$ for a clean ($p = 0$) system with $L = L_\tau = 256$ and distance $r = -0.018$ from criticality. The optimal $\ln\alpha = 6.4$ is marked by a dashed line. (b) Δ and $d^2\Delta/d(\ln\alpha)^2$ vs. $\ln\alpha$ for dilution $p = 1/3$, $L = 68$, $L_\tau = 256$ at $r = -0.049$. The optimal $\ln\alpha = 8.3$ is marked by a dashed line. (c) Spectral density $\chi''_{\rho\rho}$ for $p = 0$ and several values of $\ln\alpha$. (d) Spectral density $\chi''_{\rho\rho}$ for $p = 1/3$ and several values of $\ln\alpha$.

evaluates how well the spectral function fits the numerical data. Here, $\tilde{\chi}$ represents the numerical data for the Matsubara susceptibility, KA is a shorthand for the transformation (21), and $(\Sigma^{-1})_{mn} = \langle\tilde{\chi}(i\omega_m)\tilde{\chi}(i\omega_n)\rangle$ is the covariance matrix in Matsubara space of the numerical data. The second term in Q contains the entropy

$$S = -\sum_{\omega} A(\omega)\ln A(\omega) \tag{24}$$

of the spectral function; it regularizes the inversion. The relative weights of the two terms in Q is determined by the parameter α which we fix by a version of the L-curve method [36, 37].

The details of the maximum-entropy method, as applied to our data, are illustrated in Figure 8. Panel (a) of the figure shows the error sum Δ as a function of α for an example of a clean system, and panel (b) does the same for a diluted system with $p = 1/3$. Within the L-curve method, the optimal α is determined by the maximum of the curvature $d^2\Delta/d(\ln\alpha)^2$ which marks the crossover from fitting the data (at larger α) to fitting the Monte Carlo noise (at lower α). As a consistency check, we verify that the value of Δ at the optimal α approximately equals the number of degrees of freedom, i.e., the number $L_\tau/2$ of independent Matsubara frequencies.

Panel (c) of Figure 8 presents the resulting spectral densities for the clean example for a range of α around the optimal value, and panel (d) does the same for the diluted system. The sharp Higgs peak in the clean spectral density is affected by the value of α, but only for sizable deviations of α from its optimum value. In these cases the peak amplitude is more sensitive than the peak frequency which changes by less than 10%. In contrast, the broad "hump" in the spectral density of the diluted system remains essentially unchanged over a broad range of α values.

We have further tested the robustness of the maximum-entropy method by varying the ranges of included real and Matsubara frequencies. As long as the included frequencies cover the main features of the spectral density, this leads to small changes in $\chi''_{\rho\rho}$ of just a few percent.

We estimate the statistical error of the spectral density $\chi''_{\rho\rho}$ by means of an ensemble method. We create an ensemble of artificial data sets from the Monte Carlo data for $\chi_{\rho\rho}(\mathbf{q}, i\omega_m)$ by adding Gaussian noise to the data points, with the variance of the noise identical to the statistical uncertainties of the Monte Carlo data. We then determine $\chi''_{\rho\rho}$ for each of the data sets by a separate maximum-entropy calculation. A statistical analysis of all these results yields the error bars of $\chi''_{\rho\rho}$. Applying this method to our data, we find that the statistical errors of $\chi''_{\rho\rho}$ are small, about one symbol size in Figures 8(c) and (d).

4. INHOMOGENEOUS MEAN-FIELD APPROACH

We start from the square-lattice Bose-Hubbard Hamiltonian (9) with large integer filling $\bar{n}$. We truncate the local Hilbert space at each site j to the three basis states $|-_j\rangle$, $|0_j\rangle$, and $|+_j\rangle$, corresponding to occupation numbers $n_j = \bar{n} - 1$, $\bar{n}$, and $\bar{n} + 1$, respectively.

We now perform a basis transformation in each local Hilbert space by introducing new basis states

$$|\phi_{0j}\rangle = \cos(\theta_j/2)|0_j\rangle + \sin(\theta_j/2)\left(e^{i\eta_j}|+_j\rangle + e^{-i\eta_j}|-_j\rangle\right)/\sqrt{2}\,, \tag{25}$$

$$|\phi_{Hj}\rangle = \sin(\theta_j/2)|0_j\rangle - \cos(\theta_j/2)\left(e^{i\eta_j}|+_j\rangle + e^{-i\eta_j}|-_j\rangle\right)/\sqrt{2}\,, \tag{26}$$

$$|\phi_{Gj}\rangle = i(e^{i\eta_j}|+_j\rangle - e^{-i\eta_j}|-_j\rangle)/\sqrt{2}\,. \tag{27}$$

The inhomogeneous mean-field theory is based on a product ansatz for the ground-state wave function, $|\Phi_0\rangle = \prod_j |\phi_{0j}\rangle$. It interpolates between the Mott limit ($\theta_j = 0$) and the superfluid limit ($\theta_j = \pi/2$). The local superfluid order parameter reads $\langle a_j^\dagger\rangle \propto \psi_j = \sin\theta_j e^{-i\eta_j}$. The other two basis states, $|\phi_{Hj}\rangle$ and $|\phi_{Gj}\rangle$, correspond to changes of the order parameter amplitude and the order parameter phase, respectively, compared to the local ground state $|\phi_{0j}\rangle$. The local variational parameters, i.e., the mixing angles θ_j and the phases η_j are obtained by minimizing the ground state energy

$$\begin{aligned} E_0 &= \langle\Phi_0|H|\Phi_0\rangle \\ &= \frac{1}{2}\sum_j U_j \sin^2\frac{\theta_j}{2} - \sum_{\langle ij\rangle} \bar{n} J_{ij} \sin\theta_i \sin\theta_j \cos(\eta_i - \eta_j), \end{aligned} \tag{28}$$

leading to constant phases $\eta_j = \text{const}$ (which we set to zero) and mixing angles that fulfill the coupled mean-field equations

$$4\bar{n}\cos(\theta_i)\sum_j J_{ij}\sin(\theta_j) = U_i \sin(\theta_i)\,. \tag{29}$$

To describe excitations on top of the mean-field solution, we introduce boson operators $b_{0j}^\dagger$, $b_{Hj}^\dagger$, and $b_{Gj}^\dagger$ that create the local basis states $|\phi_{Hj}\rangle$, $|\phi_{Hj}\rangle$ and $|\phi_{Gj}\rangle$ out of the fictitious vacuum state. They fulfill the local constraint $b_{0j}^\dagger b_{0j} + b_{Hj}^\dagger b_{Hj} + b_{Gj}^\dagger b_{Gj} = 1$. We now rewrite the Bose-Hubbard Hamiltonian in terms of the b bosons and use the constraint to eliminate b_{0j}. To quadratic order in b, the excitation modes decouple and the Hamiltonian becomes the sum of a Higgs Hamiltonian and a Goldstone Hamiltonian, $H = E_0 + H_H + H_G$, with

$$H_H = -\sum_{\langle ij\rangle} \bar{n} J_{ij} \cos\theta_i \cos\theta_j (b_{Hi}^\dagger + b_{Hi})(b_{Hj}^\dagger + b_{Hj}) + \sum_i \varpi_{H,i} b_{Hj}^\dagger b_{Hj} \ , \tag{30}$$

$$H_G = -\sum_{\langle ij\rangle} \bar{n} J_{ij} \cos(\theta_i/2) \cos(\theta_j/2)(b_{Gi}^\dagger + b_{Gi})(b_{Gj}^\dagger + b_{Gj}) + \sum_i \varpi_{G,i} b_{Gj}^\dagger b_{Gj} \tag{31}$$

Each Hamiltonian describes a set of coupled harmonic oscillators with local frequencies $\varpi_{Hi} = U_i \cos(\theta_i)/2 + 2\zeta_i$ and $\varpi_{Gi} = U_i \cos^2(\theta_i/2)/2 + \zeta_i$ where $\zeta_i = \sin(\theta_i) \sum_j \bar{n} J_{ij} \sin(\theta_j)$.

The Hamiltonians H_H and H_G can each be diagonalized by Bogoliubov transformations ($\alpha = G, H$)

$$b_{\alpha j} = \sum_k (u_{\alpha jk} d_{\alpha k} + v_{\alpha jk}^* d_{\alpha k}^\dagger) \tag{32}$$

where the d bosons correspond to the collective mode eigenstates of our disordered system. The transformation coefficients u and v turn out to be real, they are given by

$$u_{\alpha jk} = \frac{1}{2}\mathcal{V}_{\alpha jk}\left(\sqrt{\varpi_{\alpha j}/\nu_{\alpha k}} + \sqrt{\nu_{\alpha k}/\varpi_{\alpha j}}\right) \ , \tag{33}$$

$$v_{\alpha jk} = \frac{1}{2}\mathcal{V}_{\alpha jk}\left(\sqrt{\varpi_{\alpha j}/\nu_{\alpha k}} - \sqrt{\nu_{\alpha k}/\varpi_{\alpha j}}\right) \ . \tag{34}$$

The matrix $\mathcal{V}_{\alpha jk}$ contains the eigenvectors (as columns) of the collective-mode eigenvalue problem

$$\sum_j X_{\alpha ij}\mathcal{V}_{\alpha jk} = \nu_{\alpha k}^2 \mathcal{V}_{\alpha ik} \tag{35}$$

where $\nu_{\alpha k}$ are the nonnegative excitation eigenfrequencies (energies). The coupling matrix X reads

$$\begin{aligned} X_{Gij} &= \varpi_{Gi}^2\delta_{ij} - 2\cos(\theta_i/2)\cos(\theta_j/2)\bar{n}J_{ij}\sqrt{\varpi_{Gi}\varpi_{Gj}} \\ X_{Hij} &= \varpi_{Hi}^2\delta_{ij} - 2\cos\theta_i\cos\theta_j\bar{n}J_{ij}\sqrt{\varpi_{Hi}\varpi_{Hj}} \end{aligned} \tag{36}$$

for the Goldstone and Higgs mode, respectively.

In terms of the d bosons, H_H and H_G are diagonal,

$$H_H = \sum_i \nu_{Hi} d_{Hi}^\dagger d_{Hi}\,, \qquad H_G = \sum_i \nu_{Gi} d_{Gi}^\dagger d_{Gi} \tag{37}$$

Using this mean-field approach, we analyze systems with site dilutions $p = 0, 1/8, 1/5,$ and $1/3$. We consider square lattices with up to 256^2 sites as well as quasi-onedimensional strips of up to 128×10^6 sites.

5. LOCALIZATION PROPERTIES OF THE HIGGS AND GOLDSTONE EXCITATIONS

To study the localization properties of the Bogoliubov states, we analyze both the participation number P and the effective fractal dimension τ_2 of the eigenstates. The inverse participation number P^{-1} of state number k is given by [47]

$$P^{-1}(k) = \sum_j (|u_{\alpha jk}|^2 - |v_{\alpha jk}|^2)^2 = \sum_j |\mathcal{V}_{\alpha jk}|^4\,. \tag{38}$$

To define the fractal dimension, we divide the system into boxes of linear size l. We define a measure

$$\mu_b = \sum_{j\in b}(|u_{\alpha jk}|^2 - |v_{\alpha jk}|^2) = \sum_{j\in b}|\mathcal{V}_{\alpha jk}|^2 \tag{39}$$

characterizing the probability of state k in box b as well as its second moment

$$P_l^{-1}(k) = \sum_b \mu_b^2 \,. \tag{40}$$

Note that we recover the participation number for box size $l = 1$, i.e., $P(k) = P_1(k)$. The corresponding fractal dimension reads

$$\tau_2(k) = \ln P_l(k)/\ln(L/l) \,. \tag{41}$$

The asymptotic value of τ_2 is obtained in the limit $L/l \to \infty$.

Figure 9 illustrates the energy dependence of the effective dimension τ_2 for Higgs and Goldstone excitations for dilution $p = 1/3$ at $U/(\bar{n}J) = 12$, slightly on the superfluid side of the transition. For the Higgs mode, τ_2 decreases with system size L for all energies indicating that the entire band is localized. The same holds for the Goldstone mode at any nonzero excitation energy. In contrast, the lowest energy Goldstone mode ($\nu_G = 0$) shows the opposite scaling behavior. τ_2 increases towards 2 with increasing L, indicating an extended state. Note that the Higgs and Goldstone modes show almost identical behavior for larger excitation energies, $\nu \gtrsim 3$, reflecting that they are still almost degenerate close to the quantum phase transition. The sharp features at energies around $\nu = 6$ are the result of the discrete character of the site dilution used to implement the disorder.

In addition to the multifractal analysis of the eigenstates, we also apply the iterative Green's function method [38, 39] to quasi-onedimensional strips. Within this methods, the localization length λ is calculated from the decay of the Green's function between the two ends of the strip. Normalizing λ by the strip width L yields a dimensionless quantity suitable

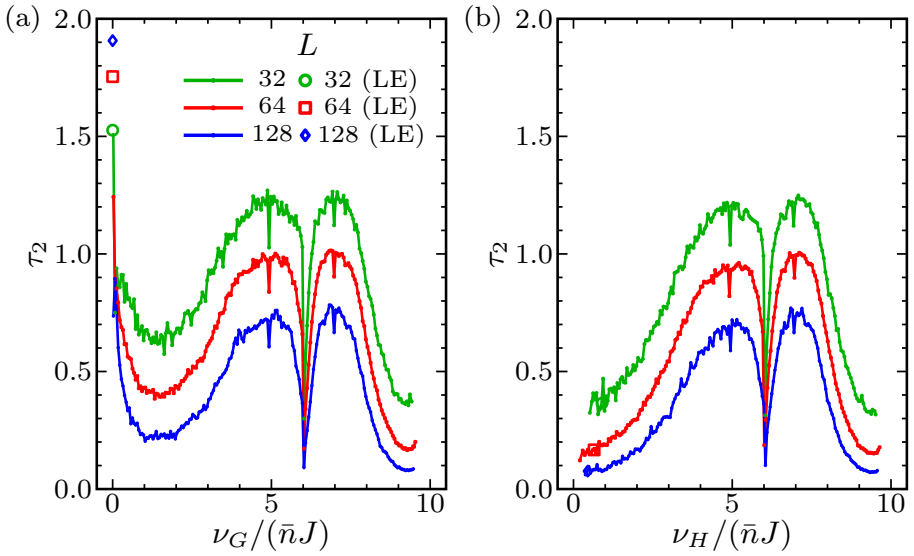

Figure 9. Generalized fractal dimension τ_2 of Goldstone (a) and Higgs (b) excitations vs. excitation energy ν for $U/(\bar{n}J) = 12$, dilution $p = 1/3$ and several system sizes L with $L/l = 8$. The solid lines represent averages of τ_2 over small energy windows (width 0.1) and 100 to 400 disorder configurations, depending on L. The values of τ_2 of the lowest-energy excitation (averaged over all disorder configurations) are shown as open symbols.

for finite-size scaling. Figure 10 presents the energy dependence of the Goldstone mode localization length for systems slightly in the superfluid phase for dilutions $p = 1/3$ and $1/8$. Specifically, it shows the scaled inverse localization length L/λ as function of the excitation energy ν_G and several strip widths L. The data for both weak and strong dilution display the same qualitative behavior. At all nonzero energies, L/λ increases with increasing strip width indicating that the Goldstone mode is localized. However, L/λ decreases rapidly as the energy ν_G approaches zero, and for $\nu_G = 0$ the inverse localization length vanishes for all strip width. These results confirm the findings of the multifractal analysis of the eigenstates above.

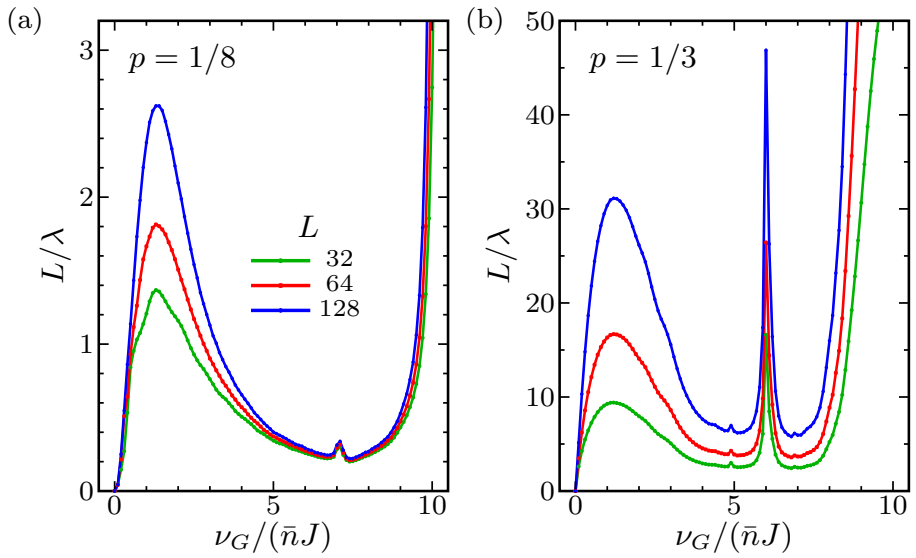

Figure 10. Scaled inverse localization length L/λ of the Goldstone excitations vs. excitation energy ν_G, calculated using the iterative Green's function method on strips of $L \times 10^6$ sites (the data are averages over 12 strips). For dilution $p = 1/3$ the data are taken at $U/(\bar{n}J) = 12$), for dilution $p = 1/8$ the data are for $U/(\bar{n}J) = 14$.

6. ANALYTIC EXPRESSION FOR THE LOWEST GOLDSTONE EXCITATION

According to Goldstone's theorem, the lowest eigenstate of the Goldstone Hamiltonian H_G must have zero energy, $\nu_{G0} = 0$, in the superfluid phase because the superfluid ground state spontaneously breaks the $U(1)$ order-parameter symmetry. For this state, the corresponding eigenvalue problem

$$\sum_j X_{Gij} \mathcal{V}_{Gj0} = \nu_{G0}^2 \mathcal{V}_{Gi0} = 0 \tag{42}$$

simplifies to a system of linear equations. A non-trivial solution of this system is given by

$$\mathcal{V}_{Gj0} = \Upsilon \frac{\sin(\theta_j/2)}{\sqrt{\varpi_{Gj}}} \tag{43}$$

as can be easily checked by inserting it back into the system (42). Here, Υ is a normalization constant. Thus, the lowest Goldstone eigenstate depends on the order parameter $\sin(\theta_j)$ and local interactions (via ϖ_{Gj}) only.

The denominator in (43) is bounded from both below and above. Specifically, in our site-diluted system, $\varpi_{Gj} \geq U/4$ and $\varpi_{Gj} \leq U/2 + 4\bar{n}J$. Consequently, the localization character of $\mathcal{V}_{Gj0}$ agrees with that of the order parameter.

Let us now assume the the system features a nonzero macroscopic order parameter ψ, i.e., an average order parameter that is nonzero in the thermodynamic limit). This implies either a more-or-less homogeneous superfluid or at lest a nonzero density of superfluid puddles. According to Eq. (43), this means that the wave function of the lowest Goldstone excitation is nonzero on a finite fraction of the sites, i.e., it is extended.

In the Mott phase, where $\sin(\theta_j)$ vanishes on all sites, the state (43) is not normalizable, indicating the absence of a zero-energy mode. It is also interesting to note that $\sin(\theta_j) = 0$ in the Mott phase implies that the disorder in the coupling matrix X_{Gij} is produced by U_i and J_{ij} only. The disorder is thus uncorrelated in space guaranteeing that all states are localized in two dimensions.

REFERENCES

[1] S. Sachdev. *Quantum phase transitions*. Cambridge University Press, Cambridge, 2011.

[2] S. L. Sondhi, S. M. Girvin, J. P. Carini, and D. Shahar. Continuous quantum phase transitions. *Rev. Mod. Phys.*, 69:315–333, Jan 1997. doi: 10.1103/RevModPhys.69.315.

[3] Thomas Vojta. Quantum phase transitions in electronic systems. *Ann. Phys. (Leipzig)*, 9(6):403–440, 2000. doi: 10.1002/1521-3889(200006)9:6¡403::AID-ANDP403¿3.0.CO;2-R.

[4] Matthias Vojta. Quantum phase transitions. *Rep. Progr. Phys.*, 66(12):2069–2110, nov 2003. doi: 10.1088/0034-4885/66/12/r01.

[5] Hilbert v. Löhneysen, Achim Rosch, Matthias Vojta, and Peter Wölfle. Fermi-liquid instabilities at magnetic quantum phase transitions. *Rev. Mod. Phys.*, 79:1015–1075, Aug 2007. doi: 10.1103/RevModPhys.79.1015.

[6] Qimiao Si and Frank Steglich. Heavy fermions and quantum phase transitions. *Science*, 329(5996):1161–1166, 2010. doi: 10.1126/science.1191195.

[7] Daniel S. Fisher. Random transverse field ising spin chains. *Phys. Rev. Lett.*, 69: 534–537, Jul 1992. doi: 10.1103/PhysRevLett.69.534.

[8] Daniel S. Fisher. Critical behavior of random transverse-field ising spin chains. *Phys. Rev. B*, 51:6411–6461, Mar 1995. doi: 10.1103/PhysRevB.51.6411.

[9] Thomas Vojta. Disorder-induced rounding of certain quantum phase transitions. *Phys. Rev. Lett.*, 90:107202, Mar 2003. doi: 10.1103/PhysRevLett.90.107202.

[10] José A. Hoyos and Thomas Vojta. Theory of smeared quantum phase transitions. *Phys. Rev. Lett.*, 100:240601, Jun 2008. doi: 10.1103/PhysRevLett.100.240601.

[11] M. Thill and D. A. Huse. Equilibrium behaviour of quantum Ising spin glass. *Physica A*, 214:321, 1995. doi: 10.1016/0378-4371(94)00247-Q.

[12] H. Rieger and A. P. Young. Griffiths singularities in the disordered phase of a quantum ising spin glass. *Phys. Rev. B*, 54:3328–3335, Aug 1996. doi: 10.1103/PhysRevB.54.3328.

[13] Olexei Motrunich, Siun-Chuon Mau, David A. Huse, and Daniel S. Fisher. Infinite-randomness quantum ising critical fixed points. *Phys. Rev. B*, 61:1160–1172, Jan 2000. doi: 10.1103/PhysRevB.61.1160.

[14] Thomas Vojta and Jörg Schmalian. Quantum griffiths effects in itinerant heisenberg magnets. *Phys. Rev. B*, 72:045438, Jul 2005. doi: 10.1103/PhysRevB.72.045438.

[15] Thomas Vojta and José A. Hoyos. Criticality and quenched disorder: Harris criterion versus rare regions. *Phys. Rev. Lett.*, 112:075702, Feb 2014. doi: 10.1103/PhysRevLett.112.075702.

[16] T. Vojta. Rare region effects at classical, quantum, and non-equilibrium phase transitions. *J. Phys. A*, 39:R143, 2006. doi: 10.1088/0305-4470/39/22/R01.

[17] T. Vojta. Quantum Griffiths effects and smeared phase transitions in metals: theory and experiment. *J. Low Temp. Phys.*, 161:299, 2010. doi: 10.1007/s10909-010-0205-4.

[18] Thomas Vojta. Disorder in quantum many-body systems. *Ann. Rev. Condens. Mat. Phys.*, 10:233–252, 2019. doi: 10.1146/annurev-conmatphys-031218-013433.

[19] C.P. Burgess. Goldstone and pseudo-goldstone bosons in nuclear, particle and condensed-matter physics. *Phys. Rep.*, 330(4):193 – 261, 2000. ISSN 0370-1573. doi: 10.1016/S0370-1573(99)00111-8.

[20] David Pekker and C.M. Varma. Amplitude/higgs modes in condensed matter physics. *Ann. Rev. Condens. Mat. Phys.*, 6(1):269–297, 2015. doi: 10.1146/annurev-conmatphys-031214-014350.

[21] Nikolay Prokof'ev and Boris Svistunov. Superfluid-insulator transition in commensurate disordered bosonic systems: Large-scale worm algorithm simulations. *Phys. Rev. Lett.*, 92:015703, Jan 2004. doi: 10.1103/PhysRevLett.92.015703.

[22] Thomas Vojta, Jack Crewse, Martin Puschmann, Daniel Arovas, and Yury Kiselev. Quantum critical behavior of the superfluid-mott glass transition. *Phys. Rev. B*, 94: 134501, Oct 2016. doi: 10.1103/PhysRevB.94.134501.

[23] T. Giamarchi, P. Le Doussal, and E. Orignac. Competition of random and periodic potentials in interacting fermionic systems and classical equivalents: The mott glass. *Phys. Rev. B*, 64:245119, Dec 2001. doi: 10.1103/PhysRevB.64.245119.

[24] Peter B. Weichman and Ranjan Mukhopadhyay. Particle-hole symmetry and the dirty boson problem. *Phys. Rev. B*, 77:214516, Jun 2008. doi: 10.1103/PhysRevB.77.214516.

[25] Mats Wallin, Erik S. Sørensen, S. M. Girvin, and A. P. Young. Superconductor-insulator transition in two-dimensional dirty boson systems. *Phys. Rev. B*, 49:12115–12139, May 1994. doi: 10.1103/PhysRevB.49.12115.

[26] Cameron Lerch and Thomas Vojta. Superfluid density and compressibility at the superfluid-mott glass transition. *Eur. Phys. J. ST*, 227(15):2275–2280, Mar 2019. ISSN 1951-6401. doi: 10.1140/epjst/e2018-800002-2.

[27] Ulli Wolff. Collective monte carlo updating for spin systems. *Phys. Rev. Lett.*, 62: 361–364, Jan 1989. doi: 10.1103/PhysRevLett.62.361.

[28] Nicholas Metropolis, Arianna W. Rosenbluth, Marshall N. Rosenbluth, Augusta H. Teller, and Edward Teller. Equation of state calculations by fast computing machines. *J. Chem. Phys.*, 21(6):1087–1092, 1953. doi: 10.1063/1.1699114.

[29] Muyu Guo, R. N. Bhatt, and David A. Huse. Quantum critical behavior of a three-dimensional Ising spin glass in a transverse magnetic field. *Phys. Rev. Lett.*, 72: 4137–4140, Jun 1994. doi: 10.1103/PhysRevLett.72.4137.

[30] H. Rieger and A. P. Young. Zero-temperature quantum phase transition of a two-dimensional ising spin glass. *Phys. Rev. Lett.*, 72:4141–4144, Jun 1994. doi: 10.1103/PhysRevLett.72.4141.

[31] Rastko Sknepnek, Thomas Vojta, and Matthias Vojta. Exotic versus conventional scaling and universality in a disordered bilayer quantum heisenberg antiferromagnet. *Phys. Rev. Lett.*, 93:097201, Aug 2004. doi: 10.1103/PhysRevLett.93.097201.

[32] Thomas Vojta and Rastko Sknepnek. Quantum phase transitions of the diluted o(3) rotor model. *Phys. Rev. B*, 74:094415, Sep 2006. doi: 10.1103/PhysRevB.74.094415.

[33] H. G. Ballesteros, L. A. Fernández, V. Martín-Mayor, A. Muñoz Sudupe, G. Parisi, and J. J. Ruiz-Lorenzo. Critical exponents of the three-dimensional diluted ising model. *Phys. Rev. B*, 58:2740–2747, Aug 1998. doi: 10.1103/PhysRevB.58.2740.

[34] Qiong Zhu, Xin Wan, Rajesh Narayanan, José A. Hoyos, and Thomas Vojta. Emerging criticality in the disordered three-color ashkin-teller model. *Phys. Rev. B*, 91:224201, Jun 2015. doi: 10.1103/PhysRevB.91.224201.

[35] J. T. Chayes, L. Chayes, Daniel S. Fisher, and T. Spencer. Finite-size scaling and correlation lengths for disordered systems. *Phys. Rev. Lett.*, 57:2999–3002, Dec 1986. doi: 10.1103/PhysRevLett.57.2999.

[36] Per Hansen and Dianne O'leary. The use of the l-curve in the regularization of discrete ill-posed problems. *SIAM J. Sci. Comput.*, 14:1487–1503, 11 1993. doi: 10.1137/0914086.

[37] Dominic Bergeron and A.-M. S. Tremblay. Algorithms for optimized maximum entropy and diagnostic tools for analytic continuation. *Phys. Rev. E*, 94:023303, Aug 2016. doi: 10.1103/PhysRevE.94.023303.

[38] A. MacKinnon and B. Kramer. The scaling theory of electrons in disordered solids: Additional numerical results. *Z. Phys. B*, 53:1, 1983. doi: 10.1007/BF01578242.

[39] A. MacKinnon. The calculation of transport properties and density of states of disordered solids. *Z. Phys. B*, 59:385, 1985. doi: 10.1007/BF01328846.

[40] Bayesian inference and the analytic continuation of imaginary-time quantum monte carlo data. *Physics Reports*, 269(3):133 – 195, 1996. ISSN 0370-1573. doi: https://doi.org/10.1016/0370-1573(95)00074-7.

[41] Daniel Podolsky and Subir Sachdev. Spectral functions of the higgs mode near two-dimensional quantum critical points. *Phys. Rev. B*, 86:054508, Aug 2012. doi: 10.1103/PhysRevB.86.054508.

[42] Massimo Campostrini, Martin Hasenbusch, Andrea Pelissetto, and Ettore Vicari. Theoretical estimates of the critical exponents of the superfluid transition in *he*4 by lattice methods. *Phys. Rev. B*, 74(14):144506, Oct 2006. doi: 10.1103/PhysRevB.74.144506.

[43] Snir Gazit, Daniel Podolsky, and Assa Auerbach. Fate of the higgs mode near quantum criticality. *Phys. Rev. Lett.*, 110:140401, Apr 2013. doi: 10.1103/PhysRevLett.110.140401.

[44] Kun Chen, Longxiang Liu, Youjin Deng, Lode Pollet, and Nikolay Prokof'ev. Universal properties of the higgs resonance in (2 + 1)-dimensional u(1) critical systems. *Phys. Rev. Lett.*, 110:170403, Apr 2013. doi: 10.1103/PhysRevLett.110.170403.

[45] Ehud Altman and Assa Auerbach. Oscillating superfluidity of bosons in optical lattices. *Phys. Rev. Lett.*, 89:250404, Dec 2002. doi: 10.1103/PhysRevLett.89.250404.

[46] D. Pekker, B. Wunsch, T. Kitagawa, E. Manousakis, A. S. Sørensen, and E. Demler. Signatures of the superfluid to mott insulator transition in equilibrium and in dynamical ramps. *Phys. Rev. B*, 86:144527, Oct 2012. doi: 10.1103/PhysRevB.86.144527.

[47] Matthias Vojta. Excitation spectra of disordered dimer magnets near quantum criticality. *Phys. Rev. Lett.*, 111:097202, Aug 2013. doi: 10.1103/PhysRevLett.111.097202.

[48] Juan Pablo Álvarez Zúñiga and Nicolas Laflorencie. Bose-glass transition and spin-wave localization for 2d bosons in a random potential. *Phys. Rev. Lett.*, 111:160403, Oct 2013. doi: 10.1103/PhysRevLett.111.160403.

[49] Mason Swanson, Yen Lee Loh, Mohit Randeria, and Nandini Trivedi. Dynamical conductivity across the disorder-tuned superconductor-insulator transition. *Phys. Rev. X*, 4:021007, Apr 2014. doi: 10.1103/PhysRevX.4.021007.

[50] Daniel Sherman, Uwe S. Pracht, Boris Gorshunov, Shachaf Poran, John Jesudasan, Madhavi Chand, Pratap Raychaudhuri, Mason Swanson, Nandini Trivedi, Assa Auerbach, Marc Scheffler, Aviad Frydman, and Martin Dressel. The higgs mode in disordered superconductors close to a quantum phase transition. *Nature Physics*, 11:188, 2015. doi: 10.1038/nphys3227.

IV. LOCALIZATION OF THE HIGGS MODE AT THE SUPERFLUID-MOTT GLASS TRANSITION

Jack Crewse, Thomas Vojta
Department of Physics, Missouri University of Science and Technology
Rolla, MO 65409, USA

ABSTRACT

The amplitude (Higgs) mode near the two-dimensional superfluid-Mott glass quantum phase transition is studied. We map the Bose-Hubbard Hamiltonian of disordered interacting bosons onto an equivalent classical XY model in (2+1) dimensions and compute the scalar susceptibility of the order parameter amplitude via Monte Carlo simulation. Analytic continuation of the scalar susceptibilities from imaginary to real frequency to obtain the spectral densities is performed by a modified maximum entropy technique. Our results show that the introduction of disorder into the system leads to unconventional dynamical behavior of the Higgs mode that violates naive scaling, despite the underlying thermodynamics of the transition being of conventional power-law type. The computed spectral densities exhibit a broad, non-critical response for all energies, and a momentum-independent dispersion for long-wavelengths, indicating strong evidence for the localization of the Higgs mode for all dilutions.

1. INTRODUCTION

Zero-temperature phase transitions between quantum ground states of interacting many-body systems have become a central focus of modern condensed matter physics. The interest in these quantum phase transitions (QPTs) is justified by the rich physics that they exhibit, from unconventional thermodynamics and transport properties, to novel phases of matter. [1, 2, 3, 4] The effects of the inevitable disorder in condensed matter systems

(impurities, defects, etc.) on these QPTs have also been intensely studied in the past two decades. Disorder leads to additional interesting physics, including infinite-randomness critical points [5], Griffiths singularities[6, 7, 8], and smeared phase transitions[9, 10] (for reviews see e.g. References [11, 12, 13]).

While much is understood about the thermodynamics of disordered QPTs, much less is known about the properties and dynamics of excitations near these critical points. Of particular interest are collective excitations in systems with spontaneously broken continous symmetry. A fundamental consequence of the breaking of the continuous symmetry of an N-component order parameter is the emergence of two distinct types of collective modes; the $(N-1)$ massless Goldstone modes – fluctuations of the order parameter phase – and a massive amplitude (Higgs) mode – fluctuations of the order parameter amplitude.[14, 15] Prominent examples of condensed matter systems that exhibit this continuous symmetry breaking include Heisenberg and XY spin systems, superfluids, superconductors, and optical lattice bosons. Higgs excitations have also been observed experimentally in a number of these systems including: the superconductor $NbSe_2$ [16], the antiferromagnetic $TiCuCl_3$ [17], and some incommensurate charge density wave compounds [18, 19].

In Lorentz-invariant systems without disorder the Higgs mode is a sharp excitation in the ordered (broken symmetry) phase sufficiently close to the QPT, with a peak in the spectral density centered at the Higgs energy ω_H. This energy softens as the critical point is approached. At zero wave vector, it obeys a power-law relationship controlled by the correlation length critical exponent $\omega_H \sim |r|^{\nu}$, where r is the reduced distance from criticality. Higgs excitations in these clean systems have been widely studied.[20, 21] While the existence of a sharp Higgs peak in two-dimensions was initially in doubt, it was later proven by both analytic and numerical techniques. However, the fate of Higgs modes in the presence of disorder is much less understood.

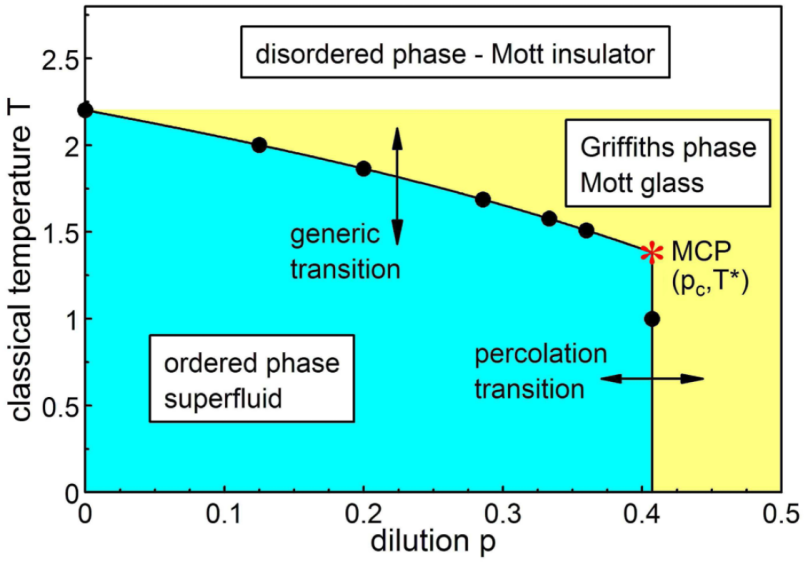

Figure 1. Phase diagram of the classical (2+1)-dimensional XY model (3) determined from Monte Carlo simulation.[22] The emergence of the Mott glass phase is seen for arbitrarily small dilutions. Large dots mark the numerically calculated transitions, lines are spline fits that only serve as a visual guide. Here, we consider the Higgs mode for $p = 1/8, 1/5, 2/7, 1/3$ across these numerically determined generic transition points.

In this article we therefore consider the effects of disorder on the Higgs mode excitation near the prototypical superfluid-Mott glass transition of disordered bosons. We model this transition using a particle-hole symmetric diluted quantum rotor model. This model is mapped onto an equivalent (2+1) dimensional classical XY model, which is then simulated via large-scale Monte Carlo methods. The imaginary (Matsubara) frequency scalar susceptibility of the order parameter is calculated. The associated spectral densities are found via analytic continuation of the Matsubara frequency data to the real-frequency axis via maximum entropy methods.

Our results show that despite the critical behavior of the superfluid-Mott glass transition being of conventional power-law type, the Higgs mode shows unconventional dynamics that violates naive scaling. Specifically, the Higgs mode becomes strongly

Table 1. Critical exponents for the (2+1)d XY model. Clean exponents are from Reference [24]. Disordered exponents are from Reference [22].

	z	β/ν	γ/ν	ν	η
Clean	1	0.5189(2)	1.961(4)	0.6717(1)	0.0381(2)
Diluted	1.52(3)	0.48(2)	2.52(4)	1.16(5)	−0.52(4)

localized below the critical point for all dilutions, resulting in a broad non-critical response in the spectral densities arbitrarily close to the critical point. A short account of part of this work has already been published in Reference [23].

The remainder of the article is organized as follows. In Section 2 we introduce the model Hamiltonian, the mapping to an equivalent classical model, and briefly discuss the thermodynamics of the corresponding superfluid-Mott glass transition. Section 3 discusses the Monte Carlo simulations. Analytic continuation of the Matsubara frequency Monte Carlo data is detailed in Section 5 and the results discussed in Section 6. We conclude and discuss experimental ramifications in Section 7.

2. SUPERFLUID-MOTT GLASS TRANSITION

We start from the Bose-Hubbard Hamiltonian describing bosons hopping between nearest-neighbor sites of a two-dimensional ($d = 2$) square-lattice of linear size L

$$H_{\mathrm{BH}} = \frac{1}{2}\sum_i U_i(\hat{n}_i - \bar{n}_i)^2 - \sum_{\langle ij\rangle} J_{ij}(a_i^\dagger a_j + h.c.) \tag{1}$$

where $a_i^\dagger$ and a_i are bosonic creation and annihilation operators at a lattice site i with $[a_i, a_j^\dagger] = \delta_{ij}$ and $\hat{n}_i = a_i^\dagger a_i$ as the number operator. Site-dependent interaction energy U_i, hopping amplitudes J_{ij}, and average filling $\bar{n}_i$ allow for a rich phase diagram. The phases and phase boundaries of this model have been well established via analytic methods.[25] In the clean case of spatially uniform on-site interactions $U_i = U$, hopping amplitude $J_{ij} = J$, and average filling $\bar{n}_i = \bar{n}$ (excepting half-integer $\bar{n}$), the system exhibits a direct

quantum phase transition between a superfluid ($J \gg U$) and a Mott insulating ($U \gg J$) ground state. Allowing spatially varied distributions (disorder) of U_i, J_{ij} and $\bar{n}_i$ introduces a third, intermediate phase that separates the bulk superfluid and Mott insulating phases. The character of this intermediate phase is dependent on the qualitative nature of the distributions of U_i, J_{ij}, and $\bar{n}_i$. For generic disorder (realized, e.g., by random on-site potentials $\bar{n}_i$) the intermediate phase is the Bose glass, a compressible gapless insulator. If the disorder is such that the system is particle-hole symmetric (uniform integer $\bar{n}_i = \bar{n}$ and random U_i, J_{ij}), this intermediate phase instead becomes the *incompressible* gapless Mott glass.

We introduce disorder into the system with site-dilution by considering $U_i = U\epsilon_i$ and $J_{ij} = J\epsilon_i\epsilon_j$ where U and J are constants. The site-dilution is controlled then by the quenched random variables ϵ_i that take on the values 0 (creates a vacancy) with probability p and 1 (creates an occupied lattice site) with probability $1 - p$. If we consider the limit of large integer filling $\bar{n}_i = \bar{n}$, the Hamiltonian (1) becomes equivalent to the Josephson junction (or quantum rotor) Hamiltonian

$$H_{\mathrm{JJ}} = \frac{U}{2} \sum_i \epsilon_i \hat{n}_i^2 + J \sum_{\langle ij \rangle} \epsilon_i \epsilon_j \cos(\hat{\phi}_i - \hat{\phi}_j) \tag{2}$$

where $\hat{n}_i$ now represents the fluctuations on top of the (uniform) filled background and $\hat{\phi}_i$ is the phase operator of a boson at site i. This model exhibits particle-hole symmetry for our site-dilution disorder and undergoes a QPT between the superfluid and Mott glass phases at a critical ratio U/J.

To facilitate the study of the dynamics near the QPT via Monte Carlo simulation, we map the 2D quantum rotor Hamiltonian H_{JJ} onto an equivalent classical model H_C that is in the same universality class.[26] This mapping yields a Hamiltonian with total dimensionality $D = d + 1 = 3$,

$$H_C = -J_s \sum_{\langle ij \rangle, \tau} \epsilon_i \epsilon_j \mathbf{S}_{i,\tau} \cdot \mathbf{S}_{j,\tau} - J_\tau \sum_{i,\tau} \epsilon_i \mathbf{S}_{i,\tau} \cdot \mathbf{S}_{i,\tau+1} \tag{3}$$

with $\mathbf{S}_{i,\tau}$ as an $O(2)$ unit vector at space coordinate i and imaginary-time coordinate τ. The coupling constants are defined such that $\beta_C J_s \sim 1/U$ and $\beta_C J_\tau \sim J$ where $\beta_C = 1/T$ is the inverse temperature of the classical model. This mapping allows us to interpret the quantum model in two dimensions as a classical model at the inverse temperature $\beta_C = 1/T$ in three-dimensions. The temperature of the classical model is not the physical temperature of the quantum system (which is at absolute zero), but represents the ratio of the quantum coupling constants U & J of the quantum system. Therefore, we can study the universal properties of the zero-temperature superfluid-Mott glass transition tuned by the ratio of couplings U/J, by tuning the classical temperature T through the transition in the classical Hamiltonian H_C. For the remainder of this article, we will discuss the transition in H_C in terms of the reduced distance from criticality $r = (T - T_c)/T_c$, for which the transition corresponds to $r \to 0$.

The thermodynamic critical behavior of H_C falls into the 3D XY universality class for the undiluted case ($p = 0$). The critical behavior in the presence of disorder was studied in Reference [22]. It is of conventional finite-disorder type with a dynamical scaling characterized by a power law relation $\xi_\tau \sim \xi_s^z$ between the correlation lengths in space and imaginary-time. This is in contrast to many other disordered quantum phase transitions that feature "infinite-randomness" critical points featuring activated dynamical scaling characterized by an exponentially growing relationship between the space and imaginary-time correlation lengths.

The phase diagram of H_C resulting from the simulations in Reference [22] is presented in Figure 1. The critical exponents for both the clean and diluted case can be found in Table 1. The numerically calculated critical exponents are used as inputs throughout the remainder of the article and careful consideration of their calculation, as well as the details of the phase diagram calculations can be found in our previous work.[22]

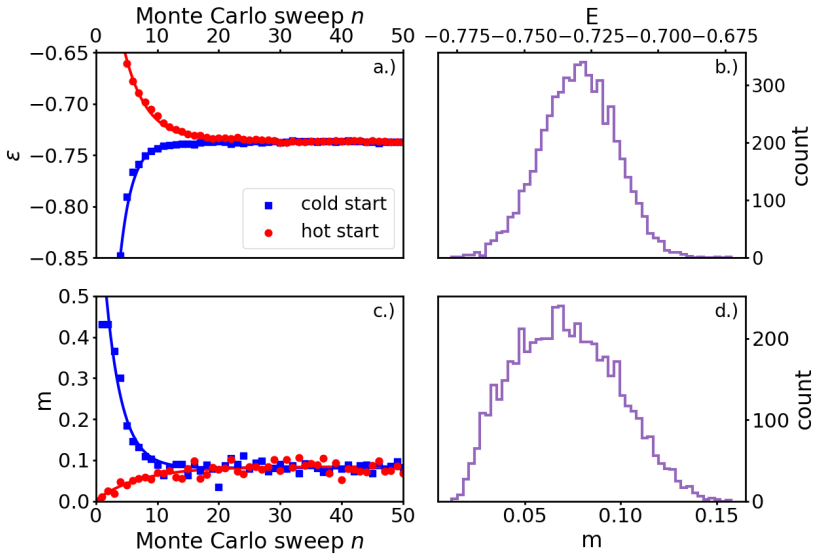

Figure 2. Comparison of 'hot' (randomly aligned spins) and 'cold' (aligned spins) start equilibration times for a.) energy per particle $\varepsilon = E/V$ (where V is the number of spins), and c.) order parameter m for a highly-dilute system ($p = 1/3$) at criticality $T = T_c = 1.5735$. Calculated from a single disorder realization of size $L = 100$ and $L_\tau = 452$. Fits of the energy and order parameter data (solid lines) to an exponential form yields equilibration times $\tau_{eq} \sim 3 - 7$. Histograms of the energy per particle and order parameter for 6000 disorder realizations of the same system are shown in b.) and d.), respectively. Each disorder realization was averaged over 1000 Monte Carlo sweeps to obtain accurate estimates.

3. MONTE CARLO SIMULATION

We study the Higgs mode by means of Monte Carlo simulation of the classical XY model Hamiltonian H_C. We consider a range of dilutions $p = 0, 1/8, 1/5, 2/7, 1/3$ below the lattice percolation threshold $p_c \approx 0.407253$. Dilutions higher than p_c cause the lattice to form disconnected clusters and do not allow for any long range order formation. Both Metropolis[27] single-spin and Wolff[28] cluster algorithms are used throughout the simulation and one Monte Carlo sweep is defined by a Wolff cluster sweep plus a Metropolis sweep over the entire lattice. A single Wolff sweep flips a number of clusters such that the total number of flipped spins is equal to the number of spins in the lattice. While the Wolff algorithm alone is sufficient in clean systems, highly dilute systems can exhibit small dangling clusters that the Metropolis algorithm can more effectively bring to equilibrium.

We estimate equilibration times by directly analyzing the evolution of the energy per particle E/V and order parameter $m = \frac{1}{V}\sum_i \mathbf{S}_i$ as a function of Monte Carlo sweep n (where V the number of occupied lattice sites). Figures 2a and 2c shows this evolution for a case where equilibration is expected to take the longest – a large, highly-dilute system right at criticality. The energy and order parameter reach equilibrium values for both a 'hot start' (all spins randomly oriented) and a 'cold start' (all spins aligned) after only $n \approx 30$ Monte Carlo sweeps. Fitting the energy data to $E_n = E_{av} + a\exp(-n/\tau_{eq})$ (and analogously for order parameter) results in equilibration times not exceeding $\tau_{eq} = 8$. We choose a number of equilibration sweeps many times larger than any measured equilibration times $N_{eq} = 100$ to ensure measurements are taken on properly equilibrated systems for even the most extreme disorder realizations.

Distributions of key thermodynamic observables has also been considered to ascertain the significance of rare events. Histograms of the energy per particle and order parameter are presented in Figure 2b and 2d. While the distributions are moderately broad, they feature no long tails. This is in agreement with what is expected for a finite-disorder fixed point[29, 30], for which the conventional power-law type critical behavior is the superfluid-Mott glass transition implies.[22]

Due to the large computational effort required to simulate disordered systems, we carefully consider the balance of measurement steps N_M and disorder realizations (samples) N_S.[31] The final variance σ^2 of a given observable after both the thermodynamic (Monte Carlo) and disorder averaging can be estimated as

$$\sigma^2 \approx (\sigma_S^2 + \sigma_M^2/N_M)/N_S \tag{4}$$

where σ_S^2 is the disorder-induced variance and σ_M^2 is the variance of single measurement for a given disorder realization. Computational effort is roughly proportional to $(N_M + N_{eq})N_S$, thus we can achieve best performance with a reasonably small σ^2 by considering a large

number of disorder realizations with a relatively small number of measurement steps. In our simulations we choose $N_M = 500$ with a number of disorder realizations $N_S = 5000 - 10000$ (dependent on system sizes).

The small number of measurement steps comes at the cost of introducing biases to traditional estimators of the required correlation functions. Without the need for disorder averaging the bias decays much faster ($\sim N_M^{-1}$) than the statistical error ($\sim N_M^{-1/2}$) and can be neglected for long Monte Carlo runs. Averaging short runs over a large number of disorder realizations suppresses the decay of the statistical error by another factor of $N_S^{-1/2}$, thus the bias may become commensurate to the statistical error and must be considered. To eliminate these biases we utilize improved estimators as discussed e.g. in Reference [32].

As the introduction of quenched disorder breaks the isotropy between the space and imaginary-time dimensions in the Hamiltonian (3), the standard finite-size scaling techniques to calculate critical exponents breaks down in the disordered case. There are two characteristic length scales we must consider in the simulations: the spatial correlation length ξ_s and the correlation length in imaginary-time ξ_τ. Correspondingly, the system sizes in the spatial dimensions L and the imaginary-time dimension L_τ are independent parameters. Anisotropic two-parameter finite-size scaling needs to be used to find the "optimal" aspect ratios L_τ/L^z (equivalently determining the dynamical exponent z), by considering system sizes that maximize the Binder cumulant at the quantum critical point (QCP). We utilize the results for the "optimal shapes" obtained in our previous simulations of the thermodynamic critical behavior.[22] Further technical details can be found in Reference [22], as well as other works on the critical behavior of Ising spin glasses. [33]

To suppress any finite-size effects, we consider only the largest system sizes accessible within our computational limits. We consider spatial sizes up to $L = 100$ and imaginary-time sizes up to $L_\tau = 452$ for diluted systems. These system sizes exceed the correlation lengths and times of the excitations we examine. For example, the smallest Higgs energy calculated for the clean case is $\omega_H \approx 0.21$ giving a characteristic time of

$2\pi/\omega_H \approx 30$, much smaller than any of the imaginary-time system sizes used. Finite-size effects in the disordered case are of even lesser concern as our results suggest that the Higgs mode localizes, and the energy of the Higgs spectral peak remains microscopic (see Figure 5).

4. SCALAR SUSCEPTIBILITY AND SPECTRAL DENSITIES

The amplitude mode is a collective excitation of the order parameter *magnitude*. The local degrees of freedom of the system defined by (3) are of fixed magnitude $|\mathbf{S}_{i,\tau}| = 1$, so we must define a local order parameter that can fluctuate. We define our order parameter by considering a course-graining of the local degrees of freedom. This is calculated as the vector sum of the $\mathbf{S}_{i,\tau}$ at the site i with its nearest (spatial) neighbors.[9] It's magnitude reads

$$\rho(\mathbf{x}_i, \tau) = \frac{1}{5}\left|\epsilon_i \mathbf{S}_{i,\tau} + \sum_j^{n.n.} \epsilon_j \mathbf{S}_{j,\tau}\right|. \tag{5}$$

Information about the Higgs mode is contained in the imaginary-time scalar susceptibility of the local order parameter magnitude $\rho(\mathbf{x}, \tau)$

$$\chi_{\rho\rho}(\mathbf{x}, \tau) = \langle \rho(\mathbf{x}, \tau)\rho(0, 0)\rangle - \langle \rho(\mathbf{x}, \tau)\rangle\langle \rho(0, 0)\rangle \tag{6}$$

and it's Fourier transform $\tilde{\chi}_{\rho\rho}(\mathbf{q}, i\omega_m) = \int d\mathbf{x} d\tau e^{-i\mathbf{q}\cdot\mathbf{x} - i\omega_m \tau} \chi_{\rho\rho}(\mathbf{x}, \tau)$ in terms of Matsubara frequencies $\omega_m = 2\pi m/\beta$ and wave vector $\mathbf{q}$. The real-frequency dynamic susceptibility is obtained via analytic continuation

$$\chi_{\rho\rho}(\mathbf{q}, \omega) = \tilde{\chi}_{\rho\rho}(\mathbf{q}, i\omega_m \to \omega + i0^+). \tag{7}$$

[9] We have also considered an alternative definition of the order parameter which includes the next-nearest-neighbors. Qualitative behavior of the Higgs mode is unaffected in both the clean and disordered systems.

The spectral density, which is related to many experimental probes, is then proportional to the imaginary part of the dynamic susceptibility

$$\chi''_{\rho\rho}(\mathbf{q},\omega) = \mathrm{Im}\,\chi_{\rho\rho}(\mathbf{q},\omega). \tag{8}$$

A scaling form for the real-frequency susceptibility at the *clean* superfluid-Mott insulator transition has been derived by Podolsky and Sachdev.[34] This can be generalized to include the quenched disorder and an appropriate dynamical exponent for the *diluted* transition we are interested in. We start from a d-dimensional, quantum field theory for an N-component order parameter ψ defined by the action

$$S = \int d^d x d\tau [(\partial_{\mathbf{x}}\psi)^2 + (\partial_\tau \psi)^2 + (r + \delta r(\mathbf{x}))\psi^2 + u\psi^4] \tag{9}$$

where r is the reduced distance from criticality, $\delta r(\mathbf{x})$ represents a quenched random-mass disorder and u is the quartic interaction strength. For the parameters of our system, $d = 2$ and $N = 2$, the action (9) is a coarse-grained, long-wavelength approximation of the quantum rotor model (2) and exhibits a QPT in the same universality class.

The free energy is given as

$$f = -\frac{1}{\beta V}\ln Z = -\frac{1}{\beta V}\ln \int D[\psi] e^{-S}. \tag{10}$$

We then notice that with two derivatives of this free energy with respect to the distance from criticality, we arrive at the expression

$$\begin{aligned}\frac{d^2 f}{dr^2} =& \frac{1}{\beta V}\int d^d x d\tau \int d^d x' d\tau' \\ &\times[\langle\psi^2(\mathbf{x},\tau)\psi^2(\mathbf{x}',\tau')\rangle - \langle\psi^2(\mathbf{x},\tau)\rangle\langle\psi^2(\mathbf{x}',\tau')\rangle]\end{aligned}$$

which is the exact expression for the $\mathbf{q} = 0$, $\omega_m = 0$ Fourier components of the scalar susceptibility of the order parameter $\chi_{\rho\rho}$. More precisely, this yields the susceptibility of the square of the order parameter amplitude, however as the order parameter magnitude is non-zero at criticality, the scaling behavior of both correlation functions is the same. The singular part of the free energy fulfills the homogeneity relationship

$$f(r) = b^{-(d+z)} f(rb^{1/\nu}) \tag{11}$$

with b as an arbitrary scale factor. From the argument above, taking two derivatives of the free energy (11) with respect to r gives the scaling behavior of the scalar susceptibility, thus implying the scaling form

$$\chi_{\rho\rho}(r, \mathbf{q}, \omega) = b^{-(d+z)+2/\nu} \chi_{\rho\rho}(rb^{1/\nu}, \mathbf{q}b, \omega b^z) \tag{12}$$

from which we identify the scale dimension of $\chi_{\rho\rho}$ as $-(d+z) + 2/\nu$. Setting $b = r^{-\nu}$ we arrive at the scaling form

$$\chi_{\rho\rho}(r, \mathbf{q}, \omega) = r^{(d+z)\nu-2} X(\mathbf{q}r^{-\nu}, \omega r^{-z\nu}) \tag{13}$$

or equivalently, with $r \sim \omega^{1/z\nu}$

$$\chi_{\rho\rho}(r, \mathbf{q}, \omega) = \omega^{[(d+z)\nu-2]/(\nu z)} Y(\mathbf{q}r^{-\nu}, \omega r^{-z\nu}) \tag{14}$$

where X and Y are scaling functions, and z is the dynamical critical exponent. If we set the dynamical exponent to the clean value $z = 1$ in two-dimensions $d = 2$ in equation (13), we arrive at the scaling form derived by Podolsky & Sachdev for the clean superfluid-Mott insulator transition

$$\chi_{\rho\rho}(\mathbf{q}, \omega) = r^{3\nu-2} X(\mathbf{q}r^{-\nu}, \omega r^{-\nu}). \tag{15}$$

Considering the critical exponents calculated for the two-dimensional superfluid-Mott glass transition, the scaling form (14) makes some interesting predictions about the fate of the Higgs mode in the diluted case. For our case, using the critical exponents calculated for the diluted transition, $z = 1.52$ and $\nu = 1.16$ (see Table 1), we see that we have

$$[(d+z)\nu - 2]/(\nu z) \approx 1.18 > 0. \tag{16}$$

This positive scaling dimension suggests that the amplitude of the singular part of the scalar susceptibility becomes strongly suppressed as the critical point is approached. Thus, the introduction of disorder may destroy a sharp, well-defined Higgs mode excitation near the QCP.

This argument can be extended to any quantum system with random mass disorder. The condition for a strongly suppressed Higgs peak near the QCP $[(d+z)\nu - 2]/(\nu z) > 1$ is equivalent to the condition $d\nu > 2$. It is well known that general disordered systems must satisfy the inequality $d\nu \geq 2$.[35] Thus it is guaranteed that we have a scaling dimension $[(d+z)\nu - 2]/(\nu z) > 1$ for the scalar susceptibility, strongly suppressing the singular part of $\chi_{\rho\rho}$ in the excitation spectra as the QCP is approached.

5. MAXIMUM ENTROPY METHODS

The Monte Carlo simulations output the scalar susceptibility $\tilde{\chi}_{\rho\rho}(\mathbf{q}, i\omega_m)$ as a function of Matsubara frequency $\omega_m = 2\pi m/\beta$. The spectral densities $\chi''_{\rho\rho}(\mathbf{q}, \omega)$ we are interested in are related to the scalar susceptibilities by the Kramers-Kronig relationship

$$\tilde{\chi}_{\rho\rho}(\mathbf{q}, i\omega_m) = \frac{1}{\pi}\int_0^\infty d\omega \chi''_{\rho\rho}(\mathbf{q}, \omega)\frac{2\omega}{\omega_m^2 + \omega^2}. \tag{17}$$

In principle, one could invert this relationship to extract the spectral densities from the computed scalar susceptibility directly. Unfortunately, this inversion is ill-conditioned and the inevitable noise of Monte Carlo data only exaggerates the problem (small errors in the input data can create large features in the spectral density).

To overcome this issue, we use a modified maximum entropy (MaxEnt) method.[36, 37] The method utilizes Bayesian inference to transform the integral inversion problem (17) into finding the most probable spectral density given the input quantum Monte Carlo (QMC) data. This reduces the problem to minimizing a cost function

$$Q = \Delta - \alpha S. \tag{18}$$

The first term in Q,

$$\Delta = (\tilde{\chi}_{\rho\rho} - K\chi''_{\rho\rho})^T \Sigma^{-1} (\tilde{\chi}_{\rho\rho} - K\chi''_{\rho\rho}) \tag{19}$$

serves as a measure of how well the fitted spectral density $\chi''_{\rho\rho}$ reproduces the input data $\tilde{\chi}_{\rho\rho}$. Here, K is a discretized version of the integration kernel $K(\omega, \omega_m) = 2\omega/(\omega_m^2 + \omega^2)$ and $\Sigma_{mn} = \langle \tilde{\chi}_{\rho\rho}(i\omega_m)\tilde{\chi}_{\rho\rho}(i\omega_n)\rangle - \langle \tilde{\chi}_{\rho\rho}(i\omega_m)\rangle\langle \tilde{\chi}_{\rho\rho}(i\omega_n)\rangle$ is the covariance matrix of the scalar susceptibility data. The second term is an entropy of the spectral density

$$S = -\sum_{\omega} \chi''_{\rho\rho}(\omega) \ln \chi''_{\rho\rho}(\omega) \tag{20}$$

that serves to regularize the inversion process, preventing over-fitting of Monte Carlo noise. This regularization is achieved because large entropy values favor a smooth spectral density, thus punishing over-fitting of the unphysical noise in the minimization of Q.

This leaves an additional free parameter α that controls the relative weight between the goodness-of-fit term Δ and the entropy term in Q. There are a number of choices in the literature concerning the determination of the value of α for a given fit. In our calculations we choose the value of α by a version of the L-curve method (see Figures 3a-b) which

maximizes the curvature $\kappa = d^2\Delta/d(\ln\alpha)^2$.[38, 39] This maximum marks a crossover from the fitting of information to the fitting of noise. Additional methods of determining the optimal fit parameter choose α such that Δ is roughly equal to the number of independent Matsubara frequencies ω_m being fit. In our simulations, we use this condition as a check for the suitability of the optimal alpha found by maximizing the curvature.

5.1. DISCRETE TIME-STEP MODIFICATIONS OF THE MAXENT METHOD

The integral relationship (17) we seek to invert in the maximum entropy method assumes continuous time or, equivalently, an infinite set of Matsubara frequencies. However, our quantum Monte Carlo method works in discrete imaginary-time. Some previous implementations of this method have used spline interpolation of the discrete time Monte Carlo data to best approximate a continuous input $\tilde{\chi}_{\rho\rho}$.[38] While this choice allows simple numerical integration when calculating (19), the interpolation method may introduce additional uncertainties that are not accounted for. In our calculations we take a different approach, instead modifying the integral kernel in (17) to account for both the discrete nature of the data as well as the periodic boundary conditions imposed on the system in the simulations. [37]

The QMC data from simulation are time discrete with imaginary-time values $\tau_k = k\Delta\tau$ with $k \in \{0, 1, ..., N-1\}$ where $N = \beta/\Delta\tau$. For a given general imaginary-time Green's function $G(\tau_k)$ the discrete Fourier transform in terms of Matsubara frequencies $\omega_m = 2\pi m/\beta = 2\pi m/\Delta\tau N$ is given by

$$G(i\omega_m) = \sum_{k=0}^{N-1} e^{i2\pi\omega_m\tau_k} G(\tau_k)\Delta\tau = \Delta\tau \sum_{k=0}^{N-1} e^{i2\pi mk/N} G(\tau_k) \tag{21}$$

The spectral (Lehmann) representation of an arbitrary imaginary-time Green's function involving operators A and B is given by

$$G(\tau_k) = -\langle A(\tau_k)B(0)\rangle = \frac{1}{Z}\sum_{l,m} A_{lm}B_{ml}e^{\tau_k(E_l-E_m)}e^{-\beta E_l} \tag{22}$$

where $Z = \mathrm{Tr}(e^{-\beta H})$ is the partition function of the system and E_n the energy of eigenstate $|n\rangle$. If we insert this into (21), and carry out the sum over k, we arrive at

$$G(i\omega_m) = \frac{\Delta\tau}{Z}\sum_{l,m} A_{lm}B_{ml}\left[\frac{e^{-\beta E_l} - e^{-\beta E_m}}{e^{\Delta\tau(i\omega_m+E_l-E_m)-1}}\right] \tag{23}$$

which allows the identification of the spectral density

$$\chi''_{\rho\rho}(\omega) = \frac{1}{Z}\sum_{l,m} A_{lm}B_{ml}[e^{-\beta E_l} - e^{-\beta E_m}]\delta(\omega - E_m - E_l). \tag{24}$$

Equation (24) is the same result as one would find in the continuous time case. This justifies expressing the discrete Matsubara frequency Green's function in terms of the continuous time spectral density such that we have

$$G(i\omega_m) = \int_{-\infty}^{\infty} d\omega\chi''_{\rho\rho}(\omega)\frac{\Delta\tau}{e^{\Delta\tau(i\omega_m-\omega)-1}}. \tag{25}$$

We now take advantage of expected properties of the spectral density $\chi''_{\rho\rho}(\omega)$. For bosonic operators we have $\chi''_{\rho\rho}(-\omega) = -\chi''_{\rho\rho}(\omega)$. This allows us to split the integration for (25) into

$$G(i\omega_m) = \int_0^{\infty} d\omega\chi''_{\rho\rho}(\omega)\left[\frac{\Delta\tau}{e^{\Delta\tau(i\omega_m-\omega)-1}} - \frac{\Delta\tau}{e^{\Delta\tau(i\omega_m+\omega)-1}}\right]. \tag{26}$$

which simplifies to the form used in the MaxEnt procedure

$$G(i\omega_m) = \int_0^{\infty} d\omega\chi''_{\rho\rho}(\omega)\left[\frac{\Delta\tau\sinh(\Delta\tau\omega)}{\cos(\Delta\tau\omega_m) - \cosh(\Delta\tau\omega)}\right] \tag{27}$$

We can verify that this simplifies to the appropriate continuous time case for $\Delta\tau \rightarrow 0$, by expanding the trigonometric functions for $\Delta\tau \ll 0$

$$G(i\omega_m) \xrightarrow{\Delta\tau\rightarrow 0} -\int_0^\infty d\omega \chi''_{\rho\rho}(\omega) \frac{2\omega}{\omega_m^2 + \omega^2}. \tag{28}$$

The convergence to the continuous time case also holds along each step of the derivation.

Applying these modifications to (17) one arrives at the relationship that is used in our MaxEnt procedure

$$\tilde{\chi}_{\rho\rho}(\mathbf{q}, i\omega_m) = \frac{1}{\pi} \int_0^\infty d\omega \chi''_{\rho\rho}(\mathbf{q}, \omega) \frac{\Delta\tau \sinh(\Delta\tau\omega)}{\cos(\Delta\tau\omega_m) - \cosh(\Delta\tau\omega)} \tag{29}$$

It is straight forward to confirm that if one takes $\Delta\tau \rightarrow 0$, we arrive back at the continuous time form (17).

5.2. MAXIMUM ENTROPY ERROR

The maximum entropy technique is notoriously sensitive to both the noise of the QMC data and the choice of weight parameter α. To understand the extent to which the output spectral densities are sensitive to these two sources of error, we have utilized two methods to make estimates of the total error introduced in this numeric analytic continuation.

First, we utilize an ensemble method to estimate the sensitivity of the method to the input QMC error bars σ_i. In addition to the analytic continuation of the output QMC data, we generate a set of synthetic data by adding random variables drawn from a Gaussian distribution with width equal to the error bar σ_i of the calculated data point. A separate Maxent procedure is performed for each of these synthetic data sets. A statistical error is then calculated from an ensemble average and variance of the resulting set of spectral densities. This gives an estimate of the statistical error introduced in the maximum entropy process from the QMC data. These error bars will be presented in each figure in Section 6,

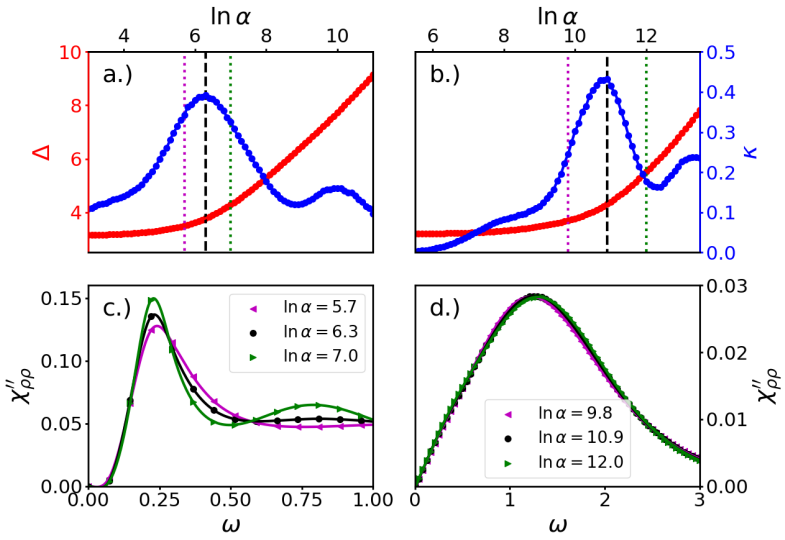

Figure 3. Maximum entropy method and it's sensitivity to variation with respect to the fit parameter α. a.) the error sum Δ and it's curvature $d^2\Delta/d(\ln\alpha)^2$ vs. $\ln\alpha$ for a clean system of size $L = L_\tau = 128$ a distance $r = -0.01$ from criticality. Dashed lines represent our chosen optimal fit parameter $\ln\alpha = 6.3$, dotted lines represent the range of variation we consider in error estimations. b.) Similar data for a diluted ($p = 1/3$) system of size $L = 100$, $L_\tau = 452$ with analogous parameters. c.) Spectral densities for the clean system at the values of $\ln\alpha$ indicated in a.). d.) Spectral densities for diluted ($p = 1/3$) system for values of $\ln\alpha$ indicated in b.).

however the magnitude of the error is such that the error bars are smaller than the symbol sizes. Second, we consider how variation of the weight parameter α about the neighborhood of the optimal value α^* affects the resulting spectral density. Taking values $\pm 5\%$ of $\ln\alpha^*$, we find that the spectral density peak positions are only weakly varied in the frequency axis, with a variation of only a few percent of their peak energies at α^* for small wave vector q. For larger q, the spectral densities become much more broad and have significantly smaller amplitude. As the peak positions of a broad maximum is less well-defined, this leads to a larger variation in the apparent peak positions for short wavelengths. This can be seen as the error bars presented with the dispersion data in Figure 8. The peak amplitudes are

significantly more sensitive to the exact value of α^* in the clean case with variations of the peak amplitudes $\approx 10\%$ (Figure 3c). In the diluted case the broader peaks and significantly smaller amplitudes suppress the peak amplitude variations (Figure 3d).

Lastly, we consider the effects introduced by changing the number of fitted Matsubara frequency data points. This becomes important in the case of large q, as the peak frequencies begin to increase and have their features broadened. For small q, the main features in the spectral density are at low frequency and, thus only a few percent variation is observed in the spectral densities when the number of ω_m included is changed, with most of the difference seen in the tails leaving the peaks relatively unaffected. For large q, an increasing number of fitted Matsubara frequencies is required to capture the main features of the broader, high-frequency features of the spectral densities. We therefore utilize all available Matsubara frequencies for fitting when considering the dispersion for the full range of q.

6. RESULTS: HIGGS MODE LOCALIZATION

For the clean ($p = 0$) system, the amplitude mode is seen as a well-defined, soft-gapped excitation with a sharp peak in the spectral density $\chi''_{\rho\rho}$ centered at the Higgs energy ω_H. The calculated zero-wavenumber spectral densities are shown in Figure 4 for a range of distances from criticality $r = (T - T_c)/T_c$. The expected scaling behavior (15) is seen to be satisfied by the collapse of the spectral densities with respect to both Higgs energy ω_H and amplitude for $r \geq -0.030$. The remaining variation between the curves in this r-range is within the errors introduced by the maximum entropy method. Beyond $r < -0.030$, both Higgs energy and amplitudes begin to violate scaling. This can be attributed to being outside of the critical window where scaling is not expected to be satisfied. These results are in agreement with previous studies of the clean case Higgs mode.[37]

A much different behavior is seen in the spectral densities as soon as disorder is introduced to the system. Our calculated zero-wavenumber spectral densities can be seen in Figure 5. The main panel compares $\chi''_{\rho\rho}$ for several dilutions at a fixed distance from

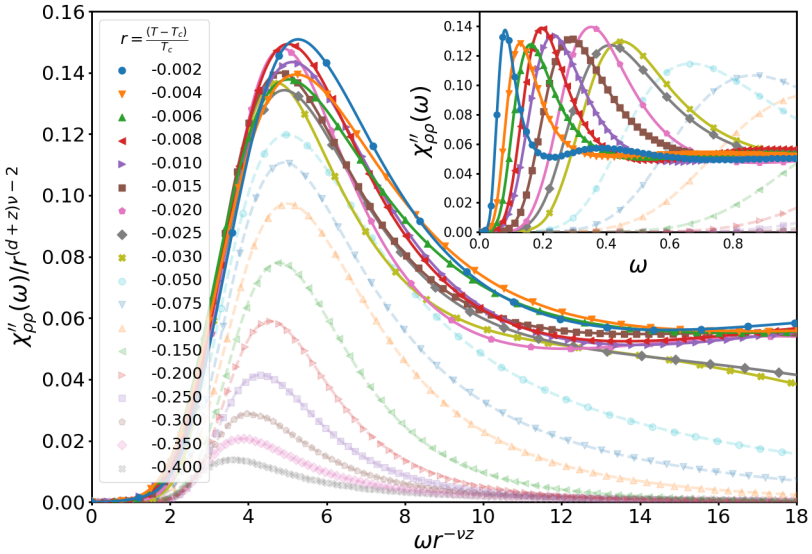

Figure 4. Spectral densities in the clean ($p = 0$) case for $\mathbf{q} = 0$ at different distances from criticality $r < 0$. Calculated from a system of size $L = L_\tau = 128$ and averaged over 10,000 samples. Main panel: Spectral densities scaled according to the expected scaling form (15). The clean spectral densities scale as expected to within the error bars of the maximum entropy techniques. Inset: Raw data of spectral densities showing the softening of ω_H as the QCP is approached. Spectral densities outside the scaling window ($r < -0.30$) are indicated by faint/dotted line plots.

criticality $r = -0.01$. A broad, non-critical response in the spectral densities is seen for all dilutions below the percolation threshold, with no sharp Higgs peak present. Even for the smallest dilution considered ($p = 1/8$), the Higgs peak is strongly suppressed, with the main contribution to the spectral weight being at high-frequencies. As dilution is increased the high-frequency contribution quickly dominates the spectral weight as can be seen in the main panel of Figure 5. For larger dilutions $\chi''_{\rho\rho}$ becomes almost dilution independent. Even more interesting is the dependence of $\chi''_{\rho\rho}$ on the distance from criticality. In contrast to the clean case, only weak variation of the spectral weight is observed as distance from criticality is adjusted for the smallest dilutions. For higher dilutions, this variation within the critical scaling region is effectively non-existent as can be seen for $p = 1/3$ in the inset

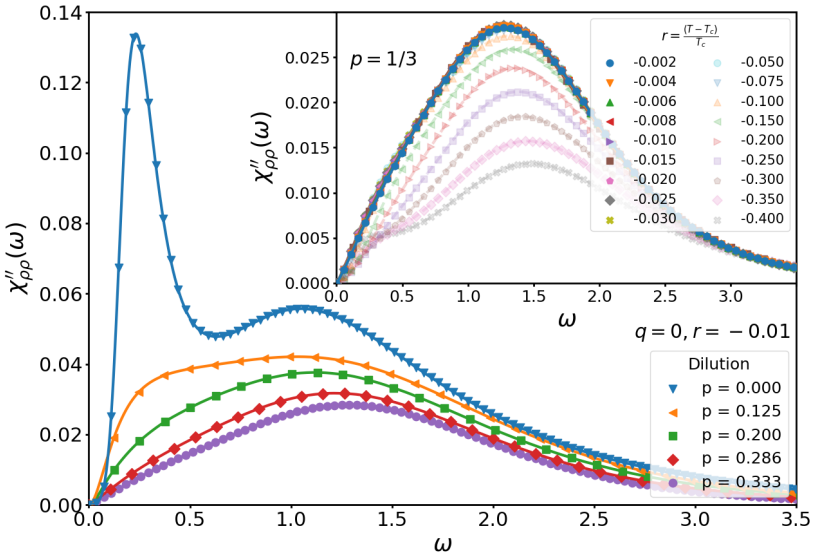

Figure 5. Main panel: Zero-wavenumber $\mathbf{q} = 0$ spectral densities at a fixed distance from criticality $r = -0.01$ for each of the dilutions considered. For each dilution we simulate a system size $L = 100$ (with $L_\tau = 175, 241, 358, 452$ corresponding to each dilutions "optimal" system size fixed by the dynamical exponent z) averaged over $10,000$ disorder samples. The prominent Higgs peak seen in the clean ($p = 0$) case is not observed even in the lowest dilutions considered ($p = 1/8$). Inset: Spectral densities of a highly-dilute system ($p = 1/3$) as a function of r. Within the scaling region $|r| < 0.03$, the spectral densities show no dependence on distance from criticality.

of Figure 5. This response of the diluted system clearly violates the naive scaling form (15) further indicating that the spectral densities must be dominated by some non-critical contribution that does not feature a sharp Higgs peak.

This striking difference between the clean and diluted spectral densities is already evident in the imaginary-time scalar correlation functions themselves where the potential instabilities of the MaxEnt procedure are of no concern. Figure 6 shows the correlation functions $\chi_{\rho\rho}(\tau)$ with respect to imaginary-time for both the clean and highly-dilute case. In the clean case, the approximately exponential decay of the correlations for large τ implies a well-defined, single-frequency peak in the associated spectral densities.[10] The softening of ω_H as the critical point is approached is also easily observed, with increasing decay times

[10]The long-time decay is not purely exponential as the clean spectral density is known to feature a soft gap at $\omega = 0$ rather than a hard gap.

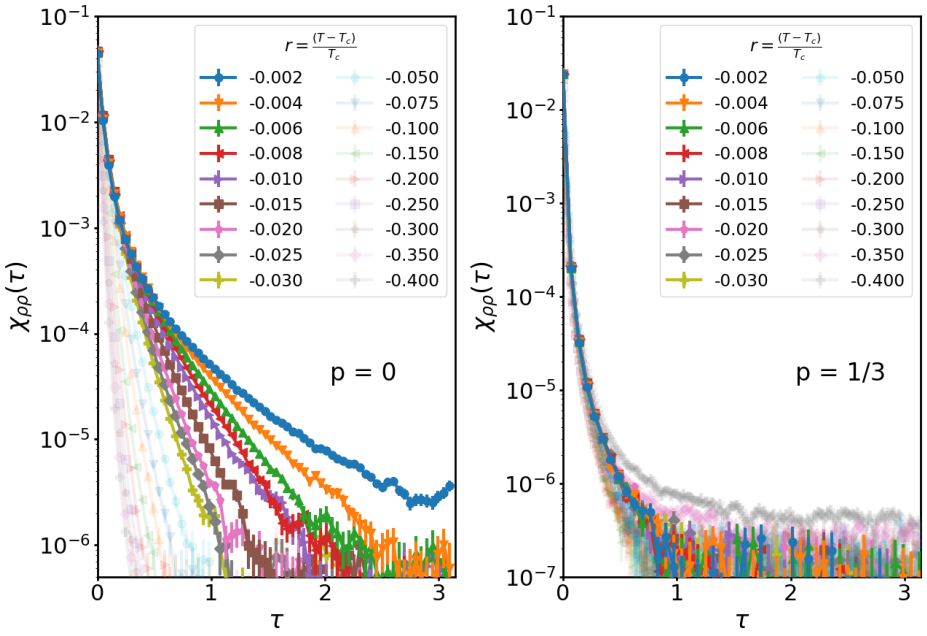

Figure 6. Comparison of scalar correlation functions in imaginary-time for a clean system (left) and a highly-dilute system (right). Approximately exponential decay of $\chi_{\rho\rho}(\tau)$ for long times implies a well-defined single frequency peak in the associated spectral density. Parameters are as in Figure 5.

closer to criticality. In contrast, the diluted case shows a much faster, non-exponential decay of the correlation function, implying a broad frequency response in the spectral densities. Additionally, the absence of any dependence on distance from criticality is observed, with correlation functions within the region $|r| \leq 0.03$ effectively identical within error bars. These two features of the diluted correlations functions are in agreement with the response seen in the spectral densities, verifying that the unconventional nature of the Higgs mode in the diluted system is evident even before the uncertainties of the MaxEnt process.

To further understand the nature of this non-critical response we also study the dispersion $\omega_H(\mathbf{q})$ of the peak positions as a function of the wave vector $\mathbf{q}$. Figure 7 shows spectral densities for $p = 0$ and $p = 1/3$ at a fixed distance from criticality $r = -0.01$ for several values of the wave number q. The clean case shows expected behavior for a $z = 1$ quantum critical point. Namely, a quadratic long-wavelength dispersion $\omega_H(\mathbf{q}) = \omega_H(0) + a\mathbf{q}^2$ that crosses over to a linear form $\omega_H(\mathbf{q}) \sim |\mathbf{q}|$ as the critical point $r \to 0$ is

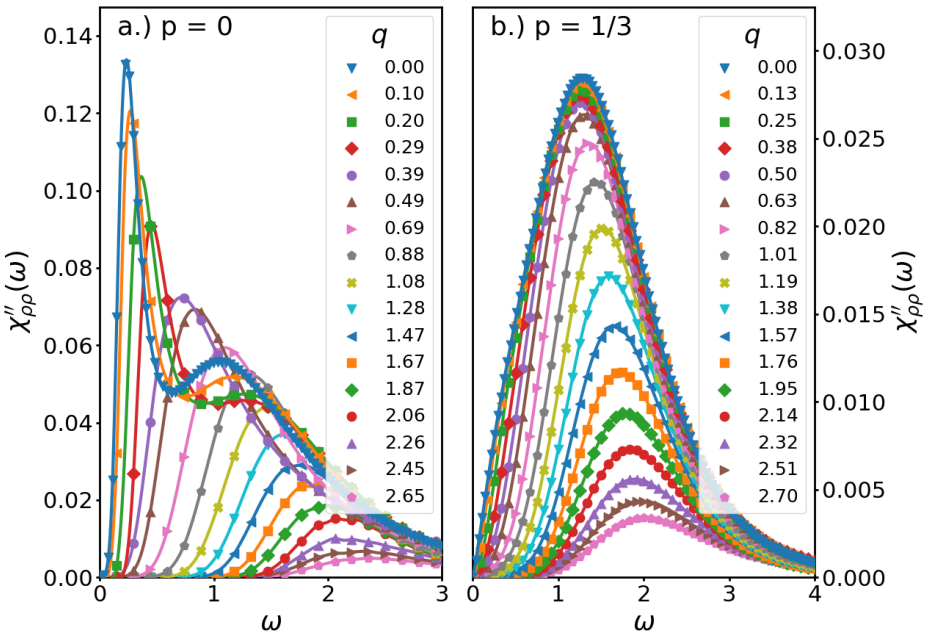

Figure 7. Spectral densities for several values of the wave number q for a.) $p = 0$ and b.) $p = 1/3$ at a fixed distance from criticality $r = -0.01$. Parameters analogous to those in Figures 4 and 5. A strong q-dependence can be seen in the clean case, whereas the diluted case features only weak q-dependence at the shortest wavelengths. These spectral densities are used as inputs for calculating the peak position dispersion $\omega_H(\mathbf{q})$.

approached. The short-wavelength behavior is much more difficult to discern in our Monte Carlo data as peaks in the spectral densities have their amplitudes decreased and peaks broadened. Higgs mode dispersions of the clean system calculated within the critical scaling region can be seen in Figure 8, with error bars indicating estimated MaxEnt uncertainties.

The diluted case exhibits different dispersion behavior with much weaker $\mathbf{q}$-dependence for short-wavelengths and showing nearly $\mathbf{q}$-independent behavior for low-energy, long-wavelength modes as illustrated in Figure 8b for $p = 1/3$. The flattening of the dispersion below a critical $\mathbf{q}^*$ suggests the existence of a localization length $\lambda \sim 1/|\mathbf{q}^*|$ beyond which no Higgs excitations can extend. This behavior is contrasted with the clean case in Figure 8. Within the critical scaling region, the dispersions are essentially independent of r, further supporting the non-critical character of the Higgs excitations.

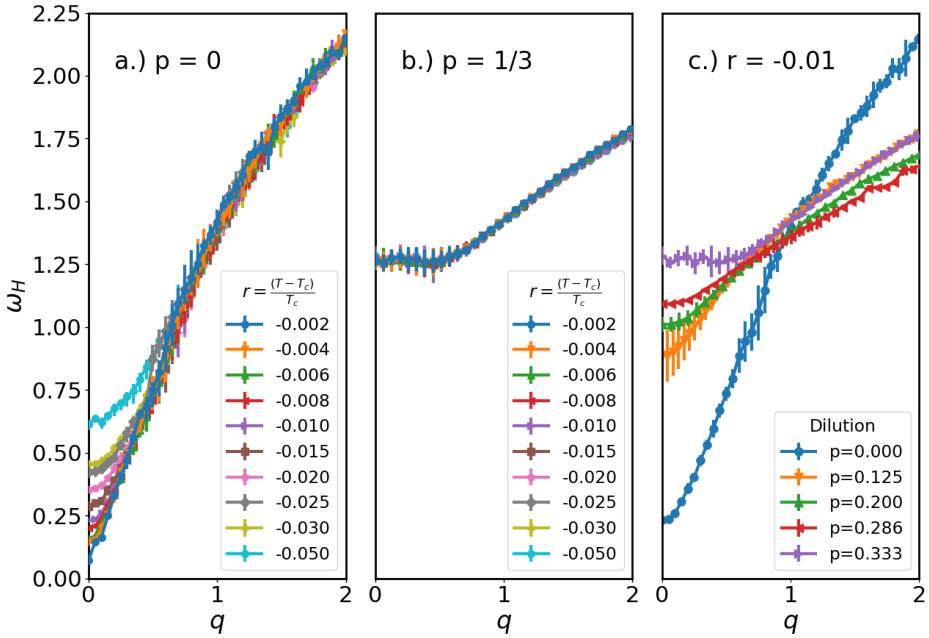

Figure 8. a.) Clean case ($p = 0$) dispersion of the Higgs energy ω_H at various distances from criticality. Calculated from a system of size $L = L_\tau = 128$. b.) Diluted case ($p = 1/3$) dispersion calculated from a system of size $L = 100$, $L_\tau = 452$. c.) Dispersion at a fixed distance from criticality ($r = -0.01$) for each of the dilutions considered. Error bars stem from variation of the fit parameter α as described in Section 5.2. Parameters are as in Figure 5.

This localization behavior also shows dependence on the dilution strength p. Figure 8c shows dispersion relations for each of the dilutions considered, at a fixed distance from criticality $r = -0.01$. The effects of dilution are clearly drastic, as even the smallest dilution causes significant flattening of the dispersions for long wavelengths. The short-wavelength behavior is also interesting, as some cross-over effects may be significant. For the lowest dilutions, the flattening of the dispersions is still substantial for all wavelengths, but the long-wavelength response is still "nearly-quadratic" for $p = 1/8$ with localization lengths only well-defined for $p = 1/5$ and beyond. As dilution is increased, the localization length decreases monotonically as the dilution further inhibits long-range correlations.

7. CONCLUSION

We have conducted a study of the Higgs (amplitude) mode near the superfluid-Mott glass quantum phase transition in two-dimensions. To this end, we have considered a Bose-Hubbard model of disordered, interacting bosons in the limit of large integer filling. The resulting quantum rotor model is then mapped onto an equivalent $(2+1)$-dimensional classical XY model and simulated via standard Metropolis and Wolff Monte Carlo algorithms. Scalar correlation functions of the order parameter are calculated as a function of Matsubara frequency and the associated spectral densities are obtained via maximum entropy methods.

In the clean case ($p = 0$), the spectral densities exhibit a sharp Higgs excitation. This excitation in the clean case satisfies scaling predictions near criticality and exhibits behavior in agreement with previous studies. Once disorder is introduced to the system, the spectral densities exhibit a broad, non-critical response that violates naive scaling arguments. This non-critical response is seen for all dilutions for which long range order is possible (i.e. below the lattice percolation threshold) and persists arbitrarily close to the critical point $r \to 0$, suggesting that the introduction of disorder to the system localizes the Higgs excitation.

The possibility of disorder-induced localization of the Higgs mode is further supported by contrasting the dispersion of the maximum of the scalar susceptibility (the Higgs peak) as a function of wave vector for the clean and diluted cases. Expected behavior is observed in the clean case, with a quadratic dispersion for long wavelengths crossing over into a linear dispersion upon approaching the critical point. In contrast, dispersion in the diluted case shows a much weaker q-dependence and a nearly q-independent response for long wavelengths, implying a localization length below which no eigenmodes can extend. This localization broadens the spectral densities and prevents a critical response. This localization length is also observed to decrease monotonically with dilution strength, suggesting the Higgs mode becomes more strongly localized as the site-dilution further inhibits long-range correlations of the order parameter fluctuations.

While the Monte Carlo results constitute strong evidence for the localization of the Higgs mode, further disentanglement of the source of the spectral response has been performed in a related work.[23, 40] The work consists of the simulation of an inhomogeneous mean-field theory of the system (1) that includes Gaussian fluctuations. The resulting spectral densities are analogous to the Monte Carlo results, showing a broad, non-critical response in the ordered phase arbitrarily close to the critical point. The mean-field theory permits the explicit analysis of the excitation eigenmodes which were found to be localized. Given that a mean-field theory has infinitely long-living excitations, this indicates localization as the source of the spectral density broadening.

The effects of disorder on the Higgs mode has also been studied from a number of other theoretical and experimental perspectives. Swanson and collaborators[41] have considered the fate of the Higgs mode across the disorder-induced superconductor-insulator transition by calculating complex conductivity $\mathrm{Re}\sigma(\omega)$. In the clean case, the Higgs mode is predicted to give rise to an absorption threshold in the conductivity. This absorption threshold is not observed in the diluted case. Rather, excess spectral weight is observed for the sub-gap frequencies. The complex conductivity has also been studied experimentally in the disordered superconducting thin-films NbN and InO. This paper reports the observation of a critical Higgs mode after accounting for excess spectral weight in the complex conductivity arising from the superfluid condensate and quasiparticle dynamics. The experimental data were approximately reproduced in a Monte Carlo simulation of a Josephson junction Hamiltonian similar to (2). At first glance, the observation of the critical Higgs mode seems to contradict our results. However, the apparent observation of this Higgs mode is likely due to relatively weak disorder, with a maximum bond dilution of $p \approx 0.125$ considered in the simulations accompanying the experiment. For weak disorder, the system is expected to display a slow crossover from the clean to disorder behavior. Further study of this crossover region would be worthwhile, but requires considerably more computational effort.

These results have the broader implication that disordered QPTs in general can exhibit unconventional collective excitations even in the case of conventional thermodynamic critical behavior. This motivates the further study of characteristics of this Higgs mode as well as the corresponding Goldstone modes. Additionally, it will certainly be interesting to investigate how spatial dimensionality and symmetries may affect these modes in disordered systems. Is it possible to classify disordered dynamics in a similar manner as the critical behavior? [29]

This work was supported in part by the NSF under grant No. DMR-1828489.

REFERENCES

[1] Sachdev, S., *Quantum Phase Transitions*, Cambridge University Press, 2011.

[2] Sondhi, S., Girvin, S., Carini, J., and Shahar, D., 'Continuous quantum phase transitions,' Rev. Mod. Phys., 1997, **69**, p. 315.

[3] Vojta, T., 'Quantum phase transitions in electronic systems,' Ann. Phys. (Leipzig), 2000, **9**(403).

[4] Vojta, M., 'Quantum phase transitions,' Rep. Prog. Phys., 2003, (66), pp. 2069–2110.

[5] Fisher, D. S., 'Random transverse field ising spin chains,' Phys. Rev. Lett., 1992, **69**(3), pp. 534–537.

[6] Griffths, R., 'Nonanalytic behviour above the critical point in a random ising ferromagnet,' Phys. Rev. Lett., 1969, **23**(17), pp. 17–19.

[7] Thill, M. and Huse, D. A., 'Equilibrium behaviour of quantum ising spin glass,' Physica A: Stat. Mech. and it's Applications, 1995, **214**(3), pp. 321–355.

[8] Rieger, H. and Young, A. P., 'Griffiths singularities in the disordered phase of a quantum ising spin glass,' Phys. Rev. B, 1996, **54**(5), pp. 3328–3335.

[9] Hoyos, J. A. and Vojta, T., 'Theory of smeared quantum phase transitions,' Phys. Rev. Lett., 2008, **100**(24), p. 240601.

[10] Vojta, T., 'Disorder-induced rounding of certain quantum phase transitions,' Phys. Rev. Lett., 2003, **90**(10), p. 107202.

[11] Vojta, T., 'Rare region effects at classical, quantum and nonequilibrium phase transitions,' J. Phys. A: Math. Gen., 2006, **39**(22), p. R143.

[12] Vojta, T., 'Quantum griffiths effects and smeared phase transitions in metals: Theory and experiment,' J Low Temp. Phys., 2010, **161**(1), pp. 299–323.

[13] Vojta, T., 'Disorder in quantum many-body systems,' Annu. Rev. Condens. Matter Phys., 2019, **10**(1), pp. 233–252.

[14] Pekker, D. and Varma, C., 'Amplitude/higgs modes in condensed matter physics,' Annu. Rev. Cond. Matt. Phys., 2015, **6**, pp. 269–97.

[15] Burgess, C., 'Goldstone and pseudo-goldstone bosons in nuclear, particle and condensed-matter physics,' Phys. Rep., 2000, **330**(4), pp. 193–261.

[16] Sooryakumar, R. and Klein, M. V., 'Raman scattering by superduncting-gap excitations and their coupling to charge-density waves,' Phys. Rev. Lett., August 1980, **45**(8), pp. 660–662.

[17] Rüegg, C., Normand, B., Matsumoto, M., Furrer, A., McMorrow, D. F., Krämer, K. W., Güdel, H. U., Gvasaliya, S. N., Mutka, H., and Boehm, M., 'Quantum magnets under pressure: Controlling elementary excitations in $TlCuCl_3$,' Phys. Rev. Lett., 2008, **100**, p. 205701.

[18] Ren, Y., Xu, Z., and Lüpke, G., 'Ultrafast collective dynamics in the charge-density-wave conductor $K_{0.3}MoO_3$,' J. Chem. Phys., March 2004, **120**(10), pp. 4755–4758.

[19] Pouget, J. P., Hennion, B., Escribe-Filippini, C., and Sato, M., 'Neutro-scattering investigations of the Kohn anomaly and of the phase and amplitude charge-density-wave excitations of the blue bronze $K_{0.3}MoO_3$,' Phys. Rev. B, April 1991, **43**(10), p. 8421.

[20] Gazit, S., Podolsky, D., and Auerbach, A., 'Fate of the higgs mode near quantum criticality,' Phys. Rev. Lett., 2013, **110**(14), p. 140401.

[21] Podolsky, D., Auerbach, A., and Arovas, D. P., 'Visibility of the amplitude (higgs) mode in condensed matter,' Phys. Rev. B., 2011, **84**(17), p. 174522.

[22] Vojta, T., Crewse, J., Puschmann, M., Arovas, D., and Kiselev, Y., 'Quantum critical behavior of the superfluid-mott glass transition,' Phys. Rev. B, 2016, **94**, p. 134501.

[23] Puschmann, M., Crewse, J., Hoyos, J. A., and Vojta, T., 'Collective modes at a disordered quantum phase transition,' Phys. Rev. Lett., 2020, **125**(2), p. 027002.

[24] Campostrini, M., Hasenbusch, M., Pelissetto, A., and Vicari, E., 'Theoretical estimates of the critical exponents of the superfluid transition in ^{4}He by lattice methods,' Phys. Rev. B, 2006, **74**(14), p. 144506.

[25] Weichman, P. B. and Mukhopadhyay, R., 'Particle-hole symmetry and the dirty boson problem,' Phys. Rev. B, 2008, **77**, p. 214516.

[26] Wallin, M., Sørensen, E. S., Girvin, S. M., and Young, A. P., 'Superconductor-insulator transition in two-dimensional dirty boson systems,' Phys. Rev. B, 1994, **49**(17), pp. 12115–12139.

[27] Metropolis, N., Rosenbluth, A., Rosenbluth, M., Teller, E., and Teller, A., 'Equation of state calculations by fast computer machines,' J. Chem. Phys., 1953, **21**(6), pp. 1087–1092.

[28] Wolff, U., 'Collective monte carlo updating for spin systems,' Phys. Rev. Lett., 1989, **62**(4), pp. 361–364.

[29] Vojta, T. and Hoyos, J. A., 'Criticality and quenched disorder: Harris criterion versus rare regions,' Phys. Rev. Lett., 2014, **112**, p. 075702.

[30] Vojta, T. and Schmalian, J., 'Percolation quantum phase transitions in diluted magnets,' Phys. Rev. Lett., 2005, **95**(23), p. 237206.

[31] Vojta, T. and Sknepnek, R., 'Quantum phase transitions of the diluted o(3) model,' Phys. Rev. B, 2006, **74**(9), p. 094415.

[32] Zhu, Q., Wan, X., Narayanan, R., Hoyos, J. A., and Vojta, T., 'Emerging criticality in the disordered three-color ashkin-teller model,' Phys. Rev. B, 2015, **91**(22), p. 224201.

[33] Guo, M., Bhatt, R. N., and Huse, D. A., 'Quantum critical behaviors of a three-dimensional ising spin glass in a transverse magnetic field,' Phys. Rev. Lett., 1994, **72**(26), pp. 4137–4140.

[34] Podolsky, D. and Sachdev, S., 'Spectral functions of the higgs mode near two-dimensional quantum critical points,' Phys. Rev. B, 2012, **86**, p. 054508.

[35] Chayes, J. T., Chayes, L., Fisher, D. S., and Spencer, T., 'Finite-size scaling and correlation lengths for disorder systems,' Phys. Rev. Lett., December 1986, **57**(24), pp. 2999–3002.

[36] Jarrel, M. and Gubernatis, J., 'Bayesian inference and the analytic continuation of imaginary-time quantum monte carlo data,' Physics Reports, 1996, **269**, p. 133.

[37] Gazit, S., Podolsky, D., Auerbach, A., and Arovas, D. P., 'Dynamics and conductivity near quantum criticality,' Phys. Rev. B, 2013, **88**, p. 235108.

[38] Bergeron, D. and Tremblay, A. M. S., 'Algorithms for optimized maximum entropy and diagnostic tools for analytic continuation,' Phys. Rev. E, 2016, **94**, p. 023303.

[39] Hansen, P. and O'Leary, D., 'The use of the l-curve method in the regularization of discrete ill-posed problems,' SIAM J. Sci. Comp., 1993, **14**, p. 1487.

[40] Puschmann, M., Getelina, J. C., Hoyos, J. A., and Vojta, T., 'Inhomogeneous mean-field approach to collective excitations in disordered interacting bosons,' 2021.

[41] Swanson, M., Loh, Y. L., Randeria, M., and Trivedi, N., 'Dynamical conductivity across the disorder-tuned superconductor-insulator transition,' Phys. Rev. X, 2014, **4**(2), p. 021007.

SECTION

2. CONCLUSIONS

In this dissertation we have investigated the effects of disorder on the critical behavior and dynamics of the superfluid-Mott insulator quantum phase transition. The critical exponents that govern the critical behavior of these phase transitions violate the Harris criterion for stability of a transition against disorder in the system. It follows that new critical behavior is expected to emerge once disorder is introduced, if a phase transition still exists at all. Analogously, the dynamical behavior of the collective excitations of the system is expected to be governed by the critical exponents. Therefore, one may naively expect the dynamics to evolve in a similar manner to the critical behavior once disorder is introduced.

In our calculations, we find that once disorder is introduced the critical behavior of the system is indeed changed. We have calculated new, dilution-independent critical exponents that now describe the transition and place the system in a new universality class. However, despite the new values of the critical exponents the critical behavior of the transition still falls into the category of "conventional" power-law critical behavior (as opposed to more exotic "infinite-randomness" critical points). We find these results in both cases of two and three spatial dimensions. These results are in line with a previously derived classification scheme of disordered quantum phase transitions based on the dimensionality of rare regions in the system.

Once the critical behavior was calculated, we shifted our focus to that of the dynamical behavior of the collective excitations near the phase boundary. Namely, the Higgs and Goldstone modes of the superfluid order parameter. Since these dynamics are governed by

power-law relationships of the critical exponents in the clean case, one may expect that the energies and dispersion of the collective excitations in the disordered case would reflect the shift in the critical exponents. However, this is not what is observed in our calculations.

We find that, in two spatial dimensions, the zero-momentum Higgs mode becomes strongly localized upon the introduction of disorder. The calculated spectral densities show no significant Higgs resonance, exhibiting only a broad, non-critical response for all energies and a momentum-independent dispersion for long wavelengths. This implies that the disorder in the system prevents long-range order parameter correlations from forming, destroying any long-lived Higgs mode excitation. This is contrary to current scaling arguments that suggest the Higgs mode is merely suppressed in the diluted case, implying that unconventional dynamical behavior arises upon the introduction of disorder.

In conclusion, this dissertation has studied the effects of disorder on the superfluid-Mott insulator quantum phase transition. We have calculated the critical behavior of the system in both two and three spatial dimensions and found that despite the change of universality class in these systems, they still exhibit conventional power-law critical behavior. With these results, we resolved a dispute among the literature for the two-dimensional case and reported the first calculations of the critical behavior in the three-dimensional case. Interestingly, despite the critical behavior of the diluted systems being of conventional power-law type, the underlying dynamical behavior of the order parameter shows unconventional localization behavior in the disordered case. This unconventional dynamical response defies theoretical expectations and opens the door to many interesting questions on the nature of the dynamical behavior of systems near a disordered quantum phase transitions.

REFERENCES

[1] Goldenfeld, N. (1992). *Lectures on Phase Transitions and the Renormalization Group*. Westview Press.

[2] Ma, S.-K. (2000), *Modern Theory of Critical Phenomenon*. Westview Press.

[3] Sornette, D. (2006). *Critical Phenomena in Natural Sciences: Chaos, Fractals, Selforganization and Disorder: Concepts and Tools*. Springer.

[4] Landau, L. (1937). On The Theory of Phase Transitions. *Zh. Eksp. Teor. Fiz., 7*, 19-32.

[5] Chaikin, P.M. & Lubensky, T. (1995). *Principles of Condensed Matter Physics*. Cambridge University Press.

[6] Chayes, J.T., Chayes, L., Fisher, D.S., Spencer, T. (1986). Finite-Size Scaling and Correlation Lengths of Disordered Systems. *Physical Review Letters*(57), 2999.

[7] Campostrini, M., Hasenbusch, M., Pelissetto, A., Rossi, P., & Vicari, E. (2001). Critical behavior of the three-dimensional XY universality class. *Physical Review B, 63*(21), 214503. https://doi.org/10.1103/PhysRevB.63.214503

[8] Landau, L. & Ginzburg, V. (1950). On The Theory of Superconductivity. *Zh. Eksp. Teor. Fiz, 20*, 1064-1082.

[9] Widom, B. (1965). Equation of State in the Neighborhood of the Critical Point, *Journal of Chemical Physics, 43* (11), 3898-3905. https://doi.org/10.1063/1.1696618

[10] Wilson, K.G. (1983). The Renormalization Group and Critical Phenomena. *Reviews of Modern Physics, 55* (3), 583-600. https://doi.org/10.1103/RevModPhys.55.583

[11] Harris, A.B. (1974). Effect of Random Defects on the Critical Behavior of Ising Models. *Journal of Physics C: Solid State Physics, 7* (9), 1671-1692. https://doi.org/10.1088/0022-3719/7/9/009

[12] Sachdev, S. (2011). *Quantum Phase Transitions*. Cambridge University Press. https://doi.org/10.1017/CBO9780511973765

[13] Binder, K. (1981). Finite size scaling analysis of ising model block distribution functions. *Z. Physik B - Condensed Matter 43*, 119-14. https://doi.org/10/1007/BF01293604

[14] Varma, P. (2002). Higgs Boson in Superconductors. *Journal of Low Temperature Physics, 126*, 901-909.

[15] Burgess, C.P. (2000). Goldstone and pseudo-Goldstone bosons in nuclear, particle and condensed-matter physics. *Physics Reports, 330* (4), 193-261. https://doi.org/10.1016/S0370-1573(99)00111-8

[16] Kubo, R. (1957). Statistical-Mechanical Theory of Irreversible Processes. I. General Theory and Simple Application to Magnetic and Conduction Problems. *Journal of the Physics Society of Japan, 12*, 570-586. https://doi.org/10.1143/jpsj.12.570

VITA

Jack Russell Crewse III was born in Kansas City, Missouri. He attended the University of Central Missouri as a music theory student from 2009 to 2011. While there he developed deep interests in nature, mathematics, and the sciences. He enrolled as a physics major at the Missouri University of Science and Technology in 2011. He joined the research group of Dr. Yew San Hor in 2013 as an undergraduate research assistant. Upon completion of his B.S. in Physics in 2015, he joined the research group of Dr. Thomas Vojta as a graduate student at Missouri University of Science and Technology. During his time working with Thomas Vojta, he published five journal articles in respectable journals such as Physical Review B and Physical Review Letters. In the winter of 2019-2020, he joined the research group of Dr. Ferdinand Evers at the University of Regensburg in Regensburg, Germany. While there he contributed to a vibrant collaboration between theorists and experimentalists that led to publications in Nature and Physical Review B. Jack's research efforts and results have been recognized in three separate first-place awards in the annual department-wide graduate research competition at Missouri University of Science and Technology. In July 2024 he received his Ph.D in Physics from Missouri University of Science and Technology.